

5-1-2011

**Vapor-grown carbon nanofiber/vinyl ester nanocomposites:
designed experimental study of mechanical properties and
molecular dynamics simulations**

Sasan Nouranian

Follow this and additional works at: <https://scholarsjunction.msstate.edu/td>

Recommended Citation

Nouranian, Sasan, "Vapor-grown carbon nanofiber/vinyl ester nanocomposites: designed experimental study of mechanical properties and molecular dynamics simulations" (2011). *Theses and Dissertations*. 4945.

<https://scholarsjunction.msstate.edu/td/4945>

This Dissertation - Open Access is brought to you for free and open access by the Theses and Dissertations at Scholars Junction. It has been accepted for inclusion in Theses and Dissertations by an authorized administrator of Scholars Junction. For more information, please contact scholcomm@msstate.libanswers.com.

VAPOR-GROWN CARBON NANOFIBER/VINYL ESTER NANOCOMPOSITES:
DESIGNED EXPERIMENTAL STUDY OF MECHANICAL PROPERTIES
AND MOLECULAR DYNAMICS SIMULATIONS

By

Sasan Nouranian

A Dissertation
Submitted to the Faculty of
Mississippi State University
in Partial Fulfillment of the Requirements
for the Degree of Doctor of Philosophy
in Chemical Engineering
in the Swalm School of Chemical Engineering

Mississippi State, Mississippi

April 2011

VAPOR-GROWN CARBON NANOFIBER/VINYL ESTER NANOCOMPOSITES:
DESIGNED EXPERIMENTAL STUDY OF MECHANICAL PROPERTIES
AND MOLECULAR DYNAMICS SIMULATIONS

By

Sasan Nouranian

Approved:

Hossein Toghiani
Associate Professor of Chemical
Engineering
Dave C. Swalm School of Chemical
Engineering
(Major Professor and Co-Director of
Dissertation)

Rebecca K. Toghiani
Associate Professor of Chemical
Engineering
Dave C. Swalm School of Chemical
Engineering
(Committee Member)

Thomas E. Lacy
Associate Professor of Aerospace
Engineering
(Co-Director of Dissertation)

Charles U. Pittman, Jr.
Professor of Chemistry
(Committee Member)

Janice K. DuBien
Associate Professor of Statistics
(Committee Member)

Rafael Hernandez
Associate Professor of Chemical
Engineering
Graduate Coordinator of the Dave C.
Swalm School of Chemical Engineering

Sarah A. Rajala
Dean of the Bagley College of
Engineering

Name: Sasan Nouranian

Date of Degree: April 29, 2011

Institution: Mississippi State University

Major Field: Chemical Engineering

Major Professor: Dr. Hossein Toghiani

Title of Study: VAPOR-GROWN CARBON NANOFIBER/VINYL ESTER
NANOCOMPOSITES: DESIGNED EXPERIMENTAL STUDY OF
MECHANICAL PROPERTIES AND MOLECULAR DYNAMICS
SIMULATIONS

Pages in Study: 199

Candidate for Degree of Doctor of Philosophy

The use of nanoreinforcements in automotive structural composites has provided promising improvements in their mechanical properties. For the first time, a robust statistical design of experiments approach was undertaken to demonstrate how key formulation and processing factors (nanofiber type, use of dispersing agent, mixing method, nanofiber weight fraction, and temperature) affected the dynamic mechanical properties of vapor-grown carbon nanofiber (VGCNF)/vinyl ester (VE) nanocomposites. Statistical response surface models were developed to predict nanocomposite storage and loss moduli as functions of significant factors. Only ~0.50 parts of nanofiber per hundred parts resin produced a roughly 20% increase in the storage modulus versus that of the neat VE at room temperature. Optimized nanocomposite properties were predicted as a function of design factors employing this methodology. For example, the use of high-shear mixing (one of the mixing methods in the design) with the oxidized VGCNFs in the absence of dispersing agent or arbitrarily with pristine VGCNFs in the presence of

dispersing agent was found to maximize the predicted storage modulus over the entire temperature range (30-120 °C). To study the key concept of interphase in thermoset nanocomposites, molecular dynamics simulations were performed to investigate liquid VE resin monomer interactions with the surface of a pristine VGCNF. A liquid resin having a mole ratio of styrene to bisphenol A-diglycidyl dimethacrylate monomers consistent with a 33 wt% styrene VE resin was placed in contact with both sides of pristine graphene sheets, overlapped like shingles, to represent the outer surface of a pristine VGCNF. The relative monomer concentrations were calculated in a direction progressively away from the surface of the graphene sheets. At equilibrium, the styrene/VE monomer ratio was higher in a 5 Å thick region adjacent to the nanofiber surface than in the remaining liquid volume. The elevated styrene concentration near the nanofiber surface suggests that a styrene-rich interphase region, with a lower crosslink density than the bulk matrix, could be formed upon curing. Furthermore, styrene accumulation in the immediate vicinity of the nanofiber surface might, after curing, improve the nanofiber-matrix interfacial adhesion compared to the case where the monomers were uniformly distributed throughout the matrix.

DEDICATION

I wish to dedicate this work to my beloved wife, Sanaz, and my beautiful daughter, Amanda. Without the encouragement and support of my wife through difficult times, none of this would have been possible. I'm forever grateful to her.

ACKNOWLEDGEMENTS

The materialization of this work would not have been possible without continuous help and support of numerous people during my past four years of studies. I wish to express my sincere gratitude to Dr. Hossein Toghiani and Dr. Thomas Lacy for their invaluable insight, experience, support, encouragement, and patience. They have been an inspiration for me during difficult times.

I also wish to thank my graduate committee members, Dr. Charles Pittman, Dr. Rebecca Toghiani, and Dr. Janice DuBien for their wholehearted support and encouragement during the different stages of my research. Their instrumental insight and many hours of discussions had a big impact on my research and the direction it took. I also wish to thank Dr. Steven Gwaltney, associate professor of chemistry in the Chemistry Department of Mississippi State University, and Changwoon Jang, my fellow Ph.D. student in the Aerospace Engineering Department, for their invaluable assistance with the molecular dynamics simulations.

Finally, I wish to acknowledge the U.S. Department of Energy, which provided the funding for this research under contract DE-FC26-06NT42755, and the Center for Advanced Vehicular Systems (CAVS) at Mississippi State University for their support.

TABLE OF CONTENTS

DEDICATION	ii
ACKNOWLEDGMENTS	iii
LIST OF TABLES	vii
LIST OF FIGURES	ix
CHAPTER	
1. INTRODUCTION	1
1.1. Motivation and Objectives	2
1.2. Overview	5
2. LITERATURE REVIEW AND THEORY	6
2.1. Vapor-Grown Carbon Nanofibers	6
2.1.1. Fabrication	7
2.1.2. Chemical Functionalization and Surface Treatment	12
2.1.3. Morphology	16
2.1.4. Mechanical Properties	18
2.2. Vinyl Ester Resin	21
2.2.1. Chemistry and Synthesis	21
2.2.2. Curing	23
2.2.3. Physical and Mechanical Properties	25
2.3. VGCNF/Polymer Nanocomposites	26
2.3.1. Fabrication	27
2.3.1.1. Nanofiber Dispersion and Interfacial Adhesion	27
2.3.1.2. Nanofiber Alignment	33
2.3.2. VGCNF/Thermoplastic Matrix Nanocomposites	35
2.3.3. VGCNF/Thermoset Matrix Nanocomposites	40
2.4. Dynamic Mechanical Analysis	42
2.5. Design of Experiments	44
2.5.1. General Full Factorial Design	46
2.5.2. Terminology	46

2.5.3. Design of Experiments in Polymer Nanocomposites	47
2.6. Molecular Dynamics Simulations of Polymer Nanocomposites.....	48
2.6.1. Nanocomposite Interface Simulations	49
2.6.2. MD Simulations of VGCNF/VE Nanocomposites.....	56
3. DYNAMIC MECHANICAL ANALYSIS OF VAPOR-GROWN CARBON NANOFIBER/VINYL ESTER NANOCOMPOSITES USING DESIGN OF EXPERIMENTS PART 1: ANALYSIS AT ROOM TEMPERATURE.....	58
3.1. Materials and Methods	59
3.1.1. Statistical Design of Experiments.....	59
3.1.2. Materials	60
3.1.3. Specimen Preparation	62
3.1.4. Dynamic Mechanical Analysis	64
3.2. Results and Discussion.....	64
3.2.1. Statistical Analysis of the Storage Modulus Data.....	68
3.2.2. Statistical Analysis of the Loss Modulus Data	75
3.2.3. Nanocomposite Optimization	81
3.3. Conclusions	81
4. DYNAMIC MECHANICAL ANALYSIS OF VAPOR-GROWN CARBON NANOFIBER/VINYL ESTER NANOCOMPOSITES USING DESIGN OF EXPERIMENTS PART 2: ANALYSIS WITH TEMPERATURE AS A FACTOR.....	83
4.1. Statistical Experimental design.....	84
4.2. Results and Discussion.....	85
4.2.1. Statistical Analysis of the Storage Modulus Data.....	94
4.2.2. Statistical Analysis of the Loss Modulus Data	111
4.2.3. Nanocomposite Optimization	124
4.3. Conclusions	125
5. MOLECULAR DYNAMICS SIMULATIONS OF VINYL ESTER RESIN MONOMER INTERACTIONS WITH A PRISTINE VAPOR-GROWN CARBON NANOFIBER AND THEIR IMPLICATIONS FOR COMPOSITE INTERPHASE FORMATION.....	126
5.1. Molecular Models.....	127
5.1.1. Models of Vinyl Ester Monomers.....	127
5.1.2. Model of the Carbon Nanofiber Surface.....	129
5.2. MD Simulation Details.....	131
5.2.1. The MD Simulation Cell.....	131
5.2.2. Dynamics Simulations	133

5.3. Results and Discussion	138
5.4. Conclusions	151
6. CONCLUSIONS AND RECOMMENDATIONS FOR FUTURE WORK.....	153
REFERENCES	159
APPENDIX	
A. MATERIAL DATA SHEETS	179
B. SAS PROGRAM CODES	189
C. SUPPLEMENTAL CONCENTRATION PROFILES	195

LIST OF TABLES

2.1	Typical properties of carbon filamentous materials (Koyama, 1972; Tibbetts & Beetz, 1987; Applied Sciences, 2011; O'Connell, 2006; Kang et al., 2006).....	20
3.1	Design factors and their levels.....	60
3.2	Nanocomposite formulations used in this study.....	62
3.3	Randomized design treatment combinations and measured average responses	66
3.4	Analysis of variance (ANOVA) for the storage modulus data.....	69
3.5	Regression analysis for the storage modulus data.....	70
3.6	Analysis of variance (ANOVA) for the loss modulus data.....	76
3.7	Multiple comparison results using least significant differences (LSD) for the interaction between the use of dispersing agent and mixing method (B×C).....	77
3.8	Regression analysis for the loss modulus data.....	78
4.1	Factors used for the study and their levels.....	85
4.2	Randomized treatment combinations and their average responses.....	87
4.3	Analysis of variance (ANOVA) for the storage modulus data.....	95
4.4	Multiple comparison results for the mean storage modulus data using least significant differences (LSD) for the interaction between the VGCNF type, use of dispersing agent, and mixing method (A×B×C).....	98
4.5	Regression analyses for the storage modulus data.....	100
4.6	Analysis of variance (ANOVA) for the loss modulus data.....	112

4.7	Multiple comparison results for the mean loss modulus data using least significant differences (LSD) for the interaction between the VGCNF type, use of dispersing agent, and mixing method (A×B×C).....	114
4.8	Regression analysis for the loss modulus data.....	116
5.1	Total number and weight fractions of vinyl ester resin monomers	133
5.2	Summary of the molecular dynamics simulation parameters	137

LIST OF FIGURES

1.1	a) Global investment in nanotechnology. b) Proposed U.S. government investment in nanotechnology for fiscal year 2009. c) Projected growth in the manufactured goods incorporating nanotechnology (Ott, 2009)	3
2.1	Batch process for growing VGCFs under atmospheric pressure (Tibbetts & Rodda, 1988; Morgan, 2005)	8
2.2	Schematic of the floating-catalyst process for growing VGCFs. a) Catalyst particles are introduced with benzene feedstock. b) Ultrafine catalyst particles such as ferrocene flowing with hydrocarbons (Endo & Shikata, 1985; Morgan, 2005).....	9
2.3	a) Schematics of VGCF nucleation and growth over a metal (M) support from the pyrolysis of acetylene (C_2H_2) (C denotes carbon and H denotes hydrogen). The growth is terminated when the catalyst is poisoned (Baker et al., 1972; Morgan, 2005). b) VGCF filament growth and fiber thickening when the growth has terminated (Tibbetts, 1989; Morgan, 2005).....	10
2.4	A schematic view of nitric acid oxidation of VGCFs at 115 °C where functional groups are attached to the end of the nanocones (Lakshminarayanan et al., 2004).....	14
2.5	a) Different VGCF morphologies resulted from the chemical vapor deposition process (Lafdi et al., 2007). b) View of a single bamboo-like VGCF in VGCF/VE nanocomposite	17
2.6	Transmission electron micrograph of a) a single-layer, and b) a double-layer VGCF cross section (Uchida et al., 2006).....	18
2.7	Reaction between a diglycidyl ether of bisphenol A and methacrylic acid to form a VE oligomer (Bruins, 1976)	22
2.8	Curing of VE oligomers with styrene (Li, 1998).....	24
2.9	a) An earlier debulking process employed by Applied Sciences Inc.	

	yielding large VGCNF agglomerated structures difficult to disperse in various polymer matrices, b) XT® debulking process yielding loose VGCNF agglomerates easier to disperse (Pyrograf Products, 2011).....	28
2.10	A schematic of different nanofiber alignment patterns in a polymer matrix, where a) is the randomly oriented pattern; b) is the pattern created by magnetic processing; c) and d) are patterns created by the DC electric field; e) represents patterns generated by the AC electric field; and f) shows patterns created by a magnetic field with a magnetic modulator (Gupta et al., 2010).....	34
2.11	Electrospinning process for the fabrication of polymer or nanocomposite fibers (Huang et al., 2003)	35
2.12	Applied oscillatory (dynamic) force (F_d) and the material response (oscillatory strain) in the dynamic mechanical analysis. F_s is the static (clamping) force and δ is the phase lag between stress and strain (Menard, 1999).....	42
2.13	The relationship between storage modulus (E'), loss modulus (E''), and phase angle (δ). E^* is the complex modulus and $\tan \delta$ is damping (Menard, 1999)	43
2.14	General description of the different transitions in polymers and the associated molecular motions responsible for them (Menard, 1999)	44
3.1	a) Silverson high-shear mixer model L4RT-A. b) A description of Solid dispersion mechanism in three stages (courtesy of Silverson Machines, Ltd.)	63
3.2	Predicted storage modulus versus actual mean data for different VGCNF types as a function of VGCNF weight fraction	72
3.3	Scanning electron micrographs of the fracture surfaces of two VGCNF/VE nanocomposites: a) 1.0 phr pristine nanofibers without dispersing agent mixed with ultrasonication, where two large-size VGCNF agglomerates (50-75 μm) can be seen. b) 1.0 phr pristine nanofibers with dispersing agent mixed with ultrasonication, where a smaller agglomerate is observed (25 μm)	74
3.4	Predicted loss modulus versus actual mean data for different mixing methods as a function of VGCNF weight fraction	80
4.1	The predicted response surface and contour plots for the storage modulus as a function of VGCNF weight fraction and temperature for the case	

	where either high-shear mixing (HS) or coupled high-shear mixing/ ultrasonication (HS/US) is used.....	102
4.2	The predicted response surface and contour plots for the storage modulus as a function of VGCNF weight fraction and temperature for the case where oxidized VGCNF (OX), dispersing agent (DA), and ultrasonication (US) are used.....	102
4.3	The predicted response surface and contour plots for the storage modulus as a function of VGCNF weight fraction and temperature for the case where ultrasonication (US) is used with any of combinations other than that of oxidized VGCNF and dispersing agent	104
4.4	Predicted storage modulus as a function of temperature for different VGCNF weight fractions for three cases: a) high-shear mixing (HS) or high-shear mixing/ultrasonication (HS/US), b) oxidized VGCNF/dispersing agent/ ultrasonication combination (OX/DA/US), and c) ultrasonication with other combinations except in b) (US (Other)).	103
4.5	Predicted storage modulus as a function of VGCNF weight fraction for different temperatures for three cases: a) high-shear mixing (HS) or high-shear mixing/ultrasonication (HS/US), b) oxidized VGCNF/dispersing agent/ultrasonication combination (OX/DA/US), and c) ultrasonication with other combinations except in b) (US (Other))....	106
4.6	Comparisons between predicted storage modulus for high-shear mixing (HS) or high-shear mixing/ultrasonication (HS/US), oxidized VGCNF/dispersing agent/ultrasonication combination (OX/DA/US), and ultrasonication with other combinations (US (Other)) for VGCNF weight fractions (D) of a) 0.25 phr, b) 0.50 phr, c) 0.75 phr, and d) 1.00 phr	107
4.7	Comparisons between predicted storage modulus for high-shear mixing (HS) or high-shear mixing/ultrasonication (HS/US), oxidized VGCNF/dispersing agent/ultrasonication combination (OX/DA/US), and ultrasonication with other combinations (US (Other)) for temperatures (T) of a) 30 °C, b) 60 °C, c) 90 °C, and d) 120 °C.....	109
4.8	The predicted response surface and contour plots for the loss modulus as a function of VGCNF weight fraction and temperature for the case where either high-shear mixing (HS) or coupled high-shear mixing/ultrasonication (HS/US) is used	117
4.9	The predicted response surface and contour plots for the loss modulus as a function of VGCNF weight fraction and temperature for the	

	case where ultrasonication (US) is used	118
4.10	Predicted Predicted loss modulus as a function of temperature for different VGCNF weight fractions for two cases: a) high-shear mixing (HS) or high-shear mixing/ultrasonication (HS/US) and b) ultrasonication (US).....	120
4.11	Predicted loss modulus as a function of VGCNF weight fraction for different temperatures for two cases: a) high-shear mixing (HS) or high-shear mixing/ultrasonication (HS/US) and b) ultrasonication (US).....	121
4.12	Comparisons between predicted loss modulus for high-shear mixing (HS) or high-shear mixing/ultrasonication (HS/US) and ultrasonication (US) for VGCNF weight fractions (D) of a) 0.25 phr, b) 0.50 phr, c) 0.75 phr, and d) 1.00 phr	122
4.13	Comparisons between predicted loss modulus for high-shear mixing (HS) or high-shear mixing/ultrasonication (HS/US) and ultrasonication (US) for temperatures (T) of a) 30 °C, b) 60 °C, c) 90 °C, and d) 120 °C	123
5.1	Bisphenol A-based dimethacrylate monomers of the vinyl ester resin: a) General formula ($n = 1.62$ for Derakane 441-400). b) Chemical formula and model created for $n = 1$. c) Chemical formula and model created for $n = 2$	128
5.2	Chemical structure and the model created for styrene	129
5.3	a) View of a single carbon nanofiber. b) Cross section of the stacked nanocone structure of VGCNF with shingled graphene sheets (adapted from (Uchida et al., 2006)). c) A schematic of overlapping graphene sheets along the outer edge of VGCNF stacked nanocones (courtesy of Changwoon Jang)	130
5.4	View of stacked (periodic) graphene sheets resembling the surface of carbon nanofiber	132
5.5	The periodic simulation cell packed with resin monomers	133
5.6	Snapshots of the initial frame after geometry optimization (left) and final frame after dynamics simulation (right) for a total simulation time of ~13 ns (following cooling procedure C1)	137
5.7	Styrene concentration profiles, time-averaged over each successive 1 ns (a) and 2 ns (b) time intervals at 1000 K.....	141

5.8	Styrene concentration profiles, time-averaged over each successive 1 ns time interval at 300 K (total simulation time of 5 ns) for simulations following cooling procedures C1 (a) and C2 (b).....	143
5.9	Concentration profiles of styrene, VE1, and VE2 averaged over the two simulations, which employed cooling procedures C1 and C2, respectively, and over 5 ns at 300 K for each simulation	144
5.10	Concentration profiles of styrene, VE1, and VE2 (a) and monomer relative concentration ratios (b), where simulations were averaged after following cooling procedures C1 and C2 over the total simulation times of 5 ns at 300 K for each procedure (results are averaged over both sides of the graphene sheets).....	146
5.11	The distribution and arrangement of styrene molecules (a), VE1 molecules (b), and VE2 molecules (c) around the graphene sheets.....	150
A.1	Concentration profiles of VE1, time-averaged over each successive 1 ns (a) and 2 ns (b) time intervals at 1000 K	196
A.2	Concentration profiles of VE2, time-averaged over each successive 1 ns (a) and 2 ns (b) time intervals at 1000 K	197
A.3	Concentration profiles of VE1 time-averaged over each successive 1 ns time interval at 300 K (total simulation time of 5 ns) for simulations following cooling procedure C1 (a) and C2 (b).....	198
A.4	Concentration profiles of VE2 time-averaged over each successive 1 ns time interval at 300 K (total simulation time of 5 ns) for simulations following cooling procedure C1 (a) and C2 (b).....	199

CHAPTER 1

INTRODUCTION

Since ancient times, humans have been using “composite” materials in one form or another. “Composite” in engineering terms refers to two or more materials of identifiably different nature that are combined to yield a material with performance characteristics that are superior to those of the individual materials (Berthelot, 1999). As an example, wood, a “natural” composite comprised of cellulose and lignin (Kulshreshtha, 2002), has been available to man as a construction material for centuries. Different classes of composite materials, such as polymer and ceramic composites, are increasingly being used to replace more traditional metallic materials (Mazumdar, 2002). For polymer composites, this is mainly due to their exceptional property-to-weight ratios and flexibility of design and fabrication. The aerospace and automotive industries are relying on composite materials since issues such as component weight and handling of complex mechanical loads are key design considerations. Continuous long glass or carbon fibers have been most used as the desired reinforcement for the composite materials. This has mainly been due to their excellent mechanical properties (depending on the choice of matrix) and added architectural flexibility. With the advent of nanomaterials, especially carbon nanofibers (CNFs) and carbon nanotubes (CNTs) (Iijima, 1991) in the 1980s and 1990s, attention was shifted towards a new class of

composite materials, “nanocomposites”. The term “nano” refers to the size scale of the reinforcement, which is in the nanometer range.

A generally agreed-upon definition for a nanocomposite is a composite material where at least one dimension of the reinforcement is less than 100 nm (Schadler et al., 2007). One unique feature of nano-sized reinforcements or “nanoreinforcements” is their extremely high surface area-to-volume ratio, which provides a significantly increased interfacial area for matrix/nanoreinforcement interactions and hence, better load transfer capability (Endo et al., 2001). Another consequence of the small size of these nanoreinforcements is their decreased likelihood of structural defects, which results in higher functional (thermal and electrical) and mechanical properties compared to their micro-scale counterparts (Wagner & Vaia, 2004; Podsiadlo et al., 2007). The majority of research in this field has been conducted on polymer nanocomposites because of their diverse applications, low costs, and excellent physical and mechanical properties (Fischer, 2003; Hussain et al., 2006).

1.1. Motivation and Objectives

The U.S. Department of Energy’s Industrial Technologies Program (ITP) has announced a nanomanufacturing initiative with a focus on energy efficiency (Ott, 2009). The goal is “to obtain comprehensive understanding of new technologies, global markets, trends, and commercialization challenges for nanomaterials and nano-enabled products that have impact on energy efficiency” (Ott, 2009). Figure 1.1 shows the distribution of global and U.S. government investment in nanotechnology and projected growth in manufactured nanotechnology-based goods (Ott, 2009). In ITP’s initiative,

nanocomposites are included as part of a high priority list of applications for energy efficiency. These materials are candidates for use in structural applications with a high demand for energy savings through weight reduction. The ITP reports a market size of \$151.9 million for nanocomposites in 2007 and an expected \$520 million market in 2012 with energy savings of up to 360 trillion BTU per year through the utilization of light-weight aerospace, marine, and other structural materials (Ott, 2009).

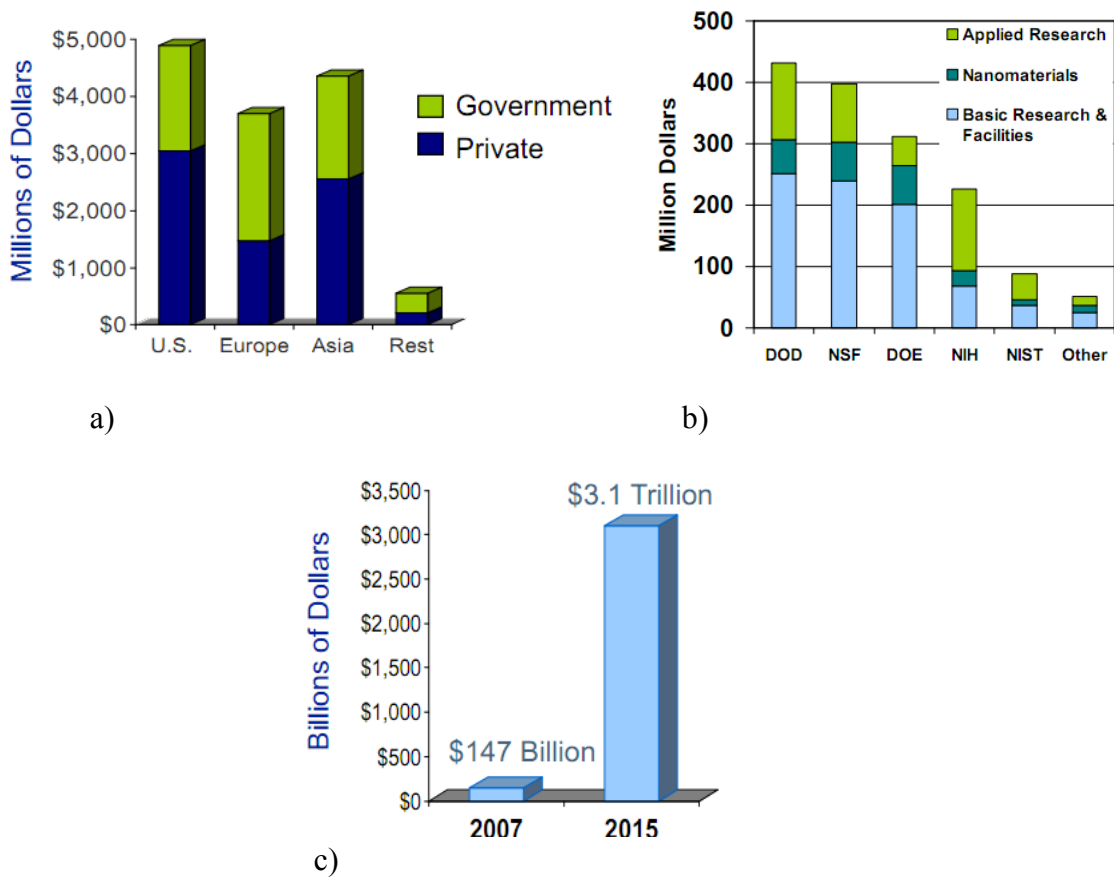


Figure 1.1 a) Global investment in nanotechnology. b) Proposed U.S. government investment in nanotechnology for fiscal year 2009. c) Projected growth in the manufactured goods incorporating nanotechnology (Ott, 2009).

The automotive sector, which has recently been striving to meet federal demands for more fuel-efficient vehicles, would benefit from the use of nanocomposites. The volatile Middle East oil supply situation has acted as a catalyst in this respect. Research is now focused on the use of novel light-weight materials to replace current automotive parts made mainly from steel. Nano-enhanced laminated composites are candidate materials for this purpose (Garcés et al., 2000). Here, “nano-enhanced” refers to a thermoset matrix reinforced with CNTs, CNFs, carbon nanoplatelets, nanoclays, mineral nanoparticles, etc. These materials are collectively termed thermoset nanocomposites. The commercialization of polymer nanocomposites for automotive applications has been slow to date due to fabrication issues such as nanoreinforcement dispersion (Edser, 2002).

This work is part of a larger research effort funded by the U.S. Department of Energy to develop and model light-weight, low cost nano-enhanced structural automotive composites. Currently, a robust framework for the design, fabrication, mechanical characterization, optimization, and predictive modeling of thermoset nanocomposites as precursors to nano-enhanced automotive composites does not exist. This dissertation addresses these crucial issues for vapor-grown carbon nanofiber (VGCNF)/vinyl ester (VE) nanocomposites. Furthermore, a treatise on the subject of “interphase” in VGCNF/VE nanocomposites is introduced for the first time, using molecular dynamics (MD) simulations as part of a “multi-scale” modeling methodology to predict nanocomposite mechanical properties.

1.2. Overview

This dissertation is divided into six chapters. A literature review of VGCNFs and VEs, nanocomposite fabrication issues, fabrication and mechanical characterization of VGCNF/thermoplastic and thermoset nanocomposites, design of experiments, dynamic mechanical analysis, and MD simulations of polymer nanocomposite interfaces are given in Chapter 2. Chapter 3 deals with the designed experimental study of the viscoelastic properties of VGCNF/VE nanocomposites at room temperature. The effect of temperature is introduced in the experimental design in Chapter 4. The concept of interphase formation in VGCNF/VE nanocomposites is explored using MD simulations in Chapter 5. Finally, conclusions and recommendations for future work are presented in Chapter 6.

CHAPTER 2

LITERATURE REVIEW AND THEORY

2.1. Vapor-Grown Carbon Nanofibers

Carbon is the building block for a myriad of organic and inorganic materials around us. It is a versatile atom capable of joining to other atoms in sp , sp^2 , and sp^3 hybridized structures giving rise to a variety of stable molecules (Hennrich et al., 2006). In its elemental form, it exists as a number of allotropes (polymorphs) including diamond, graphite, and fullerenes with significantly different properties ranging from very soft to extremely hard (Morgan, 2005). Carbon can be made to form a tubular microstructure called a filament or fiber. The unique properties of carbon fibers have expanded the science and technology of composite materials in recent decades. Vapor-grown carbon fibers (VGCFs) and their smaller size variant, vapor-grown carbon nanofibers (VGCNFs), are among the carbon fibers that have attracted a great deal of attention for their potential thermal, electrical, electromagnetic interference shielding, and mechanical property enhancements (Tibbetts et al., 2007). They are being utilized more and more in different composite materials (Hammel et al., 2004) due to their exceptional properties and low costs. A general overview of the fabrication, surface treatment, morphology, and mechanical properties of VGCFs/VGCNFs are given next.

2.1.1. Fabrication

The earliest attempt to fabricate VGCNFs, initially referred to as carbon filaments or filamentous carbon, is attributed to Hughes and Chambers (1889). They utilized a methane/hydrogen gaseous mixture and grew carbon filaments through gas pyrolysis and subsequent carbon deposition and filament growth. The true appreciation of these fibers, however, came much later when their structure could be analyzed by electron microscopy (Morgan, 2005). In the early 1970s, Koyama and Endo (1973) succeeded in manufacturing VGCFs with diameters of 1 μm and lengths of greater than 1 mm (Biró et al., 2001). Later, in the early 1980s, Tibbetts (1985) and Benissad (1988) continued to perfect the VGCF fabrication process. The first commercialization of VGCFs was attempted by Nikosso Co. in 1991 under the trade name Grasker® (Morgan, 2005). This same year, Iijima published his famous paper announcing the discovery of CNTs (Iijima, 1991). VGCNFs are produced through essentially the same manufacturing process as VGCFs. However, the diameters are typically less than 200 nm. Catalytic chemical vapor deposition (CCVD) or simply chemical vapor deposition (CVD) with variants such as thermal and plasma-assisted CVD are the dominant commercial techniques for the fabrication of VGCFs and VGCNFs. Here, gas-phase molecules are decomposed at high temperature, and carbon deposition in the presence of a transition metal catalyst with subsequent growth of the fibers around the catalyst particles is realized. In general, this process involves separate stages such as gas decomposition, carbon deposition, fiber growth, fiber thickening, graphitization, and purification, ultimately resulting in hollow fibers. The nanofiber diameter depends on the catalyst particle size (Oberlin et al., 1976). The CVD process for the fabrication of VGCFs generally falls into two categories:

1) fixed-catalyst (batch) processes, and 2) floating-catalyst (continuous) processes (Burchell, 1999).

In a fixed-catalyst process developed by Tibbetts (1985), a mixture of 15 vol% methane (CH_4) in hydrogen and helium was passed over a series of nested semi-cylindrical mullite (crystalline aluminum silicate) substrates coated with fine iron catalyst particles maintained at 1000 °C. A schematic of this process is shown in Figure 2.1 (Tibbetts & Rodda, 1988; Morgan, 2005). Fibers were grown to lengths of several centimeters with diameters of 7-10 μm on the mullite substrate in the furnace (Figure 2.1) using a gas residence time of 20 seconds. In general, fiber growth lengths can be controlled by the gas residence time in the reactor.

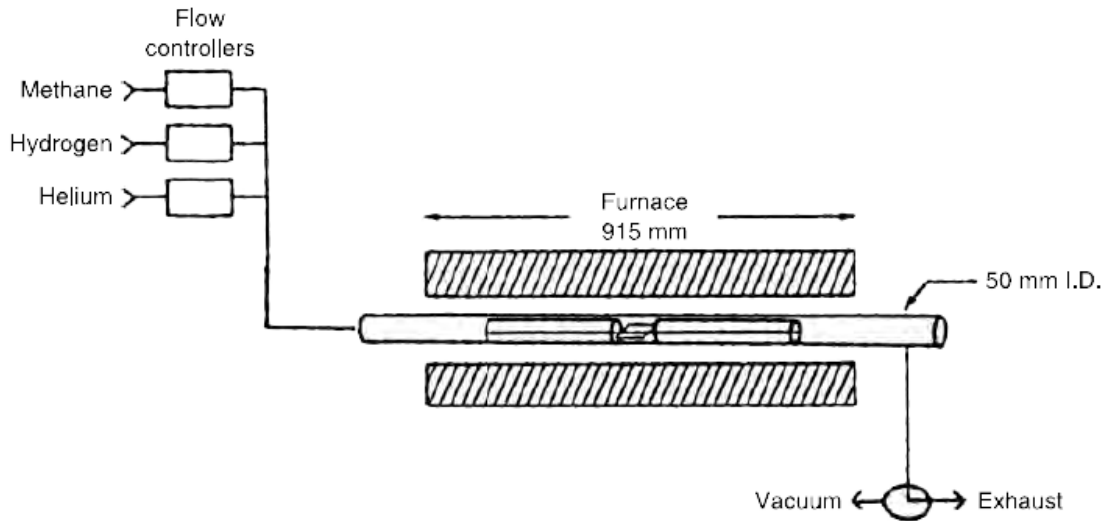


Figure 2.1 Batch process for growing VGCFs under atmospheric pressure (Tibbetts & Rodda, 1988; Morgan, 2005).

The continuous or floating-catalyst process was patented by Koyama and Endo (1983) and was later modified by Hatano et al. (1985). They utilized organometallic

compounds dissolved in a volatile solvent (benzene) as feedstock that would yield a mixture of ultrafine catalyst particles (5-25 nm in diameter) in hydrocarbon gas as the temperature rose to 1100 °C. This process typically yields VGCFs with submicron diameters and lengths of a few to 100 microns (Burchell, 1999). A schematic of the floating-catalyst process is shown in Figure 2.2 (Endo & Shikata, 1985; Morgan, 2005).

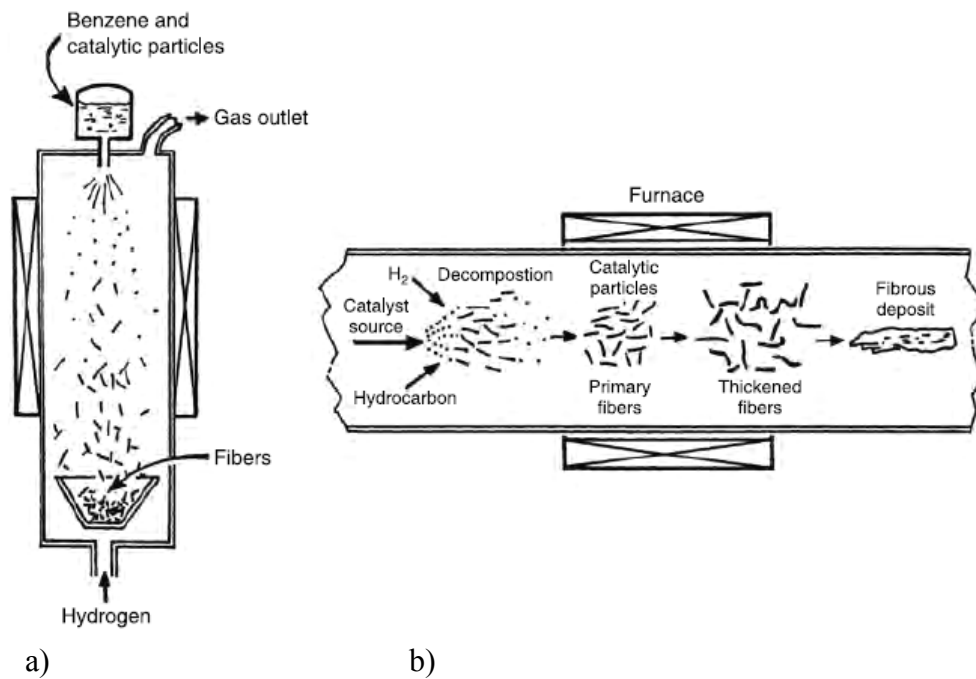


Figure 2.2 Schematic of the floating-catalyst process for growing VGCFs. a) Catalyst particles are introduced with benzene feedstock. b) Ultrafine catalyst particles such as ferrocene flowing with hydrocarbons (Endo & Shikata, 1985; Morgan, 2005).

In the furnace (Figure 2.2), the fiber growth initiates on the surface of the floating catalyst particles and continues until catalyst poisoning (deactivation) occurs due to impurities in the system. Based on the fiber growth mechanism described by Baker et al.

(1972), only that part of the catalyst particle exposed to the gas mixture contributes to the fiber growth and the growth stops as soon as the exposed part is covered, i.e., the catalyst is poisoned. The catalyst particle remains buried in the growth tip of the fiber at a final concentration of about a few parts per million (Burchell, 1999). At this stage, fiber thickening takes place. Figure 2.3 shows schematics of VGCF nucleation, growth, and thickening (Baker et al., 1972; Tibbetts, 1989; Morgan, 2005). In these schematics, the hollow core structure of the fiber and the trapped catalyst particle are visible.

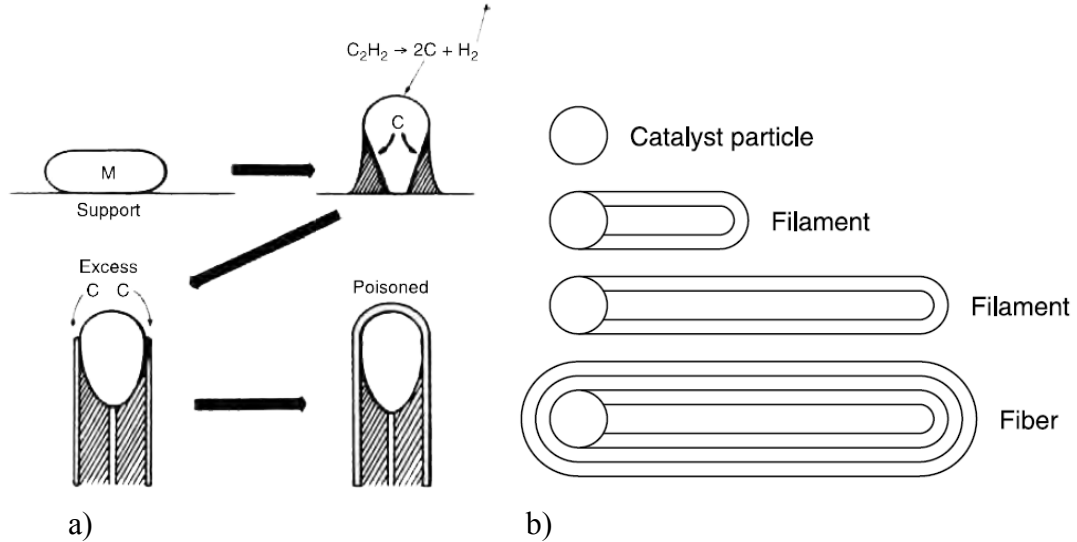


Figure 2.3 a) Schematics of VGCF nucleation and growth over a metal (M) support from the pyrolysis of acetylene (C_2H_2) (C denotes carbon and H denotes hydrogen). The growth is terminated when the catalyst is poisoned (Baker et al., 1972; Morgan, 2005). b) VGCF filament growth and fiber thickening when the growth has terminated (Tibbetts, 1989; Morgan, 2005).

The most commonly used catalyst is iron, often treated with sulfur or hydrogen sulfide, to lower its melting point and facilitate its penetration into the pores of carbon, resulting in more growth sites (Morgan 2005). Fe/Ni, Ni, Co, Mn, Cu, V, Cr, Mo and Pd

have also been used as catalysts (De Jong & Geus, 2000; Morgan, 2005). Acetylene, ethylene, methane, natural gas, and benzene are the most commonly used carbonaceous gases. Often, carbon monoxide is introduced into the gas flow to increase the carbon yield through reduction of iron oxides that may form in the system. Dresselhaus et al. (1988), Rodriguez (1993), De Jong and Geus (2000), and Tibbetts et al. (2007) have reviewed the CVD process for the manufacturing of VGCFs.

Applied Sciences, Inc. (ASI), a leading manufacturer of VGCNFs in the U.S.A., is the supplier of the nanofibers used in this study (Applied Sciences, 2011). Their technology was licensed from General Motors and their VGCFs and VGCNFs were introduced under the trade name, Pyrograf®. Pyrograf®-I are VGCFs manufactured by the fixed-catalyst process, while Pyrograf®-II and their latest graphitic, very fine, and tubular Pyrograf®-III, are VGCNFs manufactured by the continuous floating-catalyst process (Tibbetts et al., 1994; Biró et al., 2001). This class of VGCNF is comprised of two types: i) PR-19, and ii) PR-24; and three grades: 1) pyrolytically stripped (designated as PS in the grade specification), where the polyaromatic hydrocarbons are removed from the surface of the fiber through a purification process, 2) low heat-treated (LHT), where a heat treatment at 1500 °C provides more graphitic structures of the deposited carbon on the surface of the Pyrograf® fibers resulting in VGCNFs with excellent electrical conductivities, and 3) high heat-treated (HHT), where the nanofiber is heat treated at 3000 °C further graphitizing and enhancing the crystallinity of the CVD carbon on the nanofiber surface. The resulting VGCNFs are highly graphitic with low iron catalyst content (Pyrograf Products, 2011). PR-19 has an average diameter of 150 nm, while PR-24 has a smaller average diameter of 100 nm. The level of nanofiber entanglement, which

is a consequence of the vapor phase manufacturing process, is generally reduced through a “debulking” process. The nanofibers that have undergone this debulking process are designated as XT (Pyrograf Products, 2011).

2.1.2. Chemical Functionalization and Surface Treatment

A strong interfacial interaction must exist between the nanofiber and polymer matrix to exploit the reinforcing characteristics of VGCNFs in structural nanocomposite applications (Tibbetts et al., 2007; Lafdi et al., 2008; Zhu & Kissell, 2008). Pristine VGCNFs have highly agglomerated structures with poor interfacial adhesion that often lead to a limited load transfer between the matrix and the nanofiber. Hence, attempts have been made to “functionalize” or “treat” the nanofiber surfaces to enhance the interfacial adhesion and aid in the de-agglomeration and dispersion of nanofibers in the matrix. Many currently employed methods have been applied to CNTs, but they can be applied as readily to VGCNFs. The only difference is in the VGCNF surface structure that limits the available functionalization sites to the end portions of the stacked nanocones, as opposed to the whole surface area available for functionalization in CNTs. Currently, two methods are used for functionalizing nanofibers: 1) non-covalent functionalization, and 2) covalent functionalization. The former relies on hydrophilic/hydrophobic interaction forces between a “wrapping” polymer or surfactant and the nanofiber surface (Zhu & Kissell, 2008), while the latter employs strong covalent bonds between the nanofibers and the matrix to promote better interfacial adhesion. The surfactant molecules in non-covalent functionalization can be anionic, neutral, or cationic in nature. Examples of surfactants include sodium dodecyl sulfate (anionic), Pluronic® (a biocompatible

polyethylene oxide (PEO)-polypropylene oxide (PPO) copolymer) (neutral), and cetyl trimethylammonium bromide (cationic) (Zhu & Kissell, 2008). The drawback of non-covalent functionalization is a limited load transfer from the matrix to the nanofiber due to the absence of strong covalent bonds.

Covalent functionalization is accomplished with methods such as oxidation (Rasheed et al., 2006), chemical modification of oxidized nanofibers, free radical addition and nanofiber surface grafting, electron beam irradiation (Evora et al., 2010), plasma treatment, etc. (Zhu & Kissell, 2008). The choice of the functional group introduced to the VGCNF surface is critical since it influences the nanofiber/matrix interactions and, hence, the nanocomposite's mechanical properties. Furthermore, the functional group should not affect the curing chemistry of the resin in thermoset nanocomposites. Oxidation is the most commonly used method to functionalize the nanofiber surface, where strong acids like HNO_3 , $\text{H}_2\text{SO}_4/\text{HNO}_3$, or $\text{H}_2\text{SO}_4/\text{H}_2\text{O}_2$ are reacted with nanofibers to generate carboxylic (-COOH) and other oxo-functionalities on the nanofiber surface. Lakshminarayanan et al. (2004) reacted VGCNFs with a concentrated (~70 wt%) aqueous nitric acid solution at 115 °C for various amounts of time. The surface functionalities of VGCNFs were determined through sodium hydroxide (NaOH) titration and conducted surface area measurements and X-ray photoelectron spectroscopy (XPS) analysis. An increase in the surface oxygen content was observed from 6.3% to 18.5% after only 10 minutes of reaction. A schematic of the VGCNF surface oxidation is shown in Figure 2.4 (Lakshminarayanan et al., 2004). Another oxidation method is dry oxidation or etching in air at high temperatures (Zhu & Kissell, 2008; Tibbetts et al., 2007).

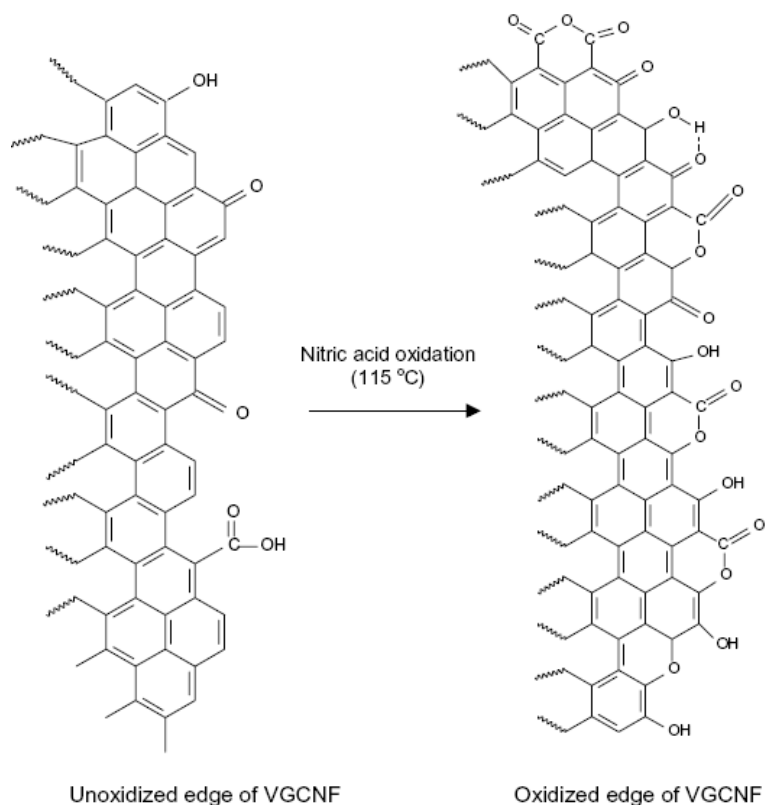


Figure 2.4 A schematic view of nitric acid oxidation of VGCNFs at 115 °C where functional groups are attached to the end of the nanocones (Lakshminarayanan et al., 2004).

Fluorination of CNTs and VGCNFs provides active surfaces suitable for alkyl, amine, carboxylic, and other substitution reactions (Zhu & Kissell, 2008). For example, reflux of fluorinated single-walled carbon nanotubes (SWCNTs) in the presence of excess hexamethylenediamine resulted in amino-substitution of fluorine, thereby facilitating the reaction of nanotubes with resins such as epoxy (Stevens et al., 2003). This was achieved by interfacial covalent bond formation. As another method for amine functionalization of nanofiber surface, Karippal et al. (2010) acid-treated VGCNFs using a $\text{H}_2\text{SO}_4/\text{HNO}_3$ mixture, acylated the surface with thionyl chloride, and finally amino-

functionalized the modified VGCNFs with triethylenetetramine (TETA). A variety of improvements were observed in the electrical, thermal, and mechanical properties of the nanocomposites prepared from the functionalized VGCNFs and epoxy. Other VGCNF side wall reactions are also possible (Chaos-Morán et al., 2009). Li et al. (2005) have an excellent report on the surface functionalization of graphitic CNFs (GCNFs). The nanofiber surfaces were oxidized through chemical reaction with nitric acid to yield carboxylic acid groups. These groups were further reacted with “linker” molecules derived from diamines and triamines. Strong interfacial covalent bonds may then be developed between the functionalized GCNFs and the resin during curing.

Use of free radical initiators (hardeners) can effectively lead to the grafting of different alkyl, methyl chloride, methyl cyanide, and other groups on the surfaces of VGCNFs (Zhu & Kissell, 2008). Morales-Teysier et al. (2006) investigated the effect of peroxide functionalization of VGCNFs on the mechanical properties of polystyrene (PS)/nanofiber nanocomposites. A 25-30% increase in the storage and tensile moduli of the nanocomposites (containing 0.5 wt% VGCNFs) were reported through the use of 0.075 wt% of peroxide. Shi et al. (2003) used plasma polymerization treatment to coat an ultra thin PS layer (~3 nm) on the surfaces of VGCNFs. An increase in the tensile strength of VGCNF/PS nanocomposites was observed due to improved compatibility between VGCNFs and PS. Hence, a better dispersion of coated VGCNFs in the PS matrix was achieved. In a similar study, He et al. (2006) investigated the effect of plasma surface treatment of VGCNFs on the mechanical properties of VGCNF/polycarbonate (PC) nanocomposites. An increase in the tensile strengths of the nanocomposites prepared using modified VGCNFs were observed compared to unmodified VGCNFs.

Another approach used to treat the VGCNF surfaces is metallization. In this technique, the nanofiber surface is coated with metal atoms (Cu, Ag, Ni, etc.) (Zhu & Kissell, 2008). This leads to an increased number of sites for strong nanofiber/matrix interactions, while the nanofiber/nanofiber interactions are minimized, leading to better nanofiber dispersion characteristics. For example, epoxy resin forms complexes with copper (Cu) and, hence, metallization of the nanofiber surfaces with Cu leads to a better interfacial adhesion in VGCNF/epoxy nanocomposites.

Attempts have also been made to oxidize VGCNF surfaces in the reactor during the CVD growth process (Tibbetts et al., 2007). Glasgow and Lake (2003) used oxidizing gases like carbon dioxide (CO₂) in the reactor to increase both surface area and surface energy of VGCNFs.

2.1.3. Morphology

The unique features of the fiber growth process in CVD result in different nanofiber morphologies, which may later be modified by various post-production treatments, such as pyrolytic stripping, heat treatment, and oxidation. Depending on the reaction temperature, the nanofibers can be relatively straight, twisted, or helical (Morgan, 2005; Lafdi et al., 2007). They often have worm-like or sometimes bamboo-like shapes with amorphous carbon (carbon black) on the surface (Cui et al., 2004; Lafdi et al., 2007; Lawrence et al., 2007) (Figure 2.5).

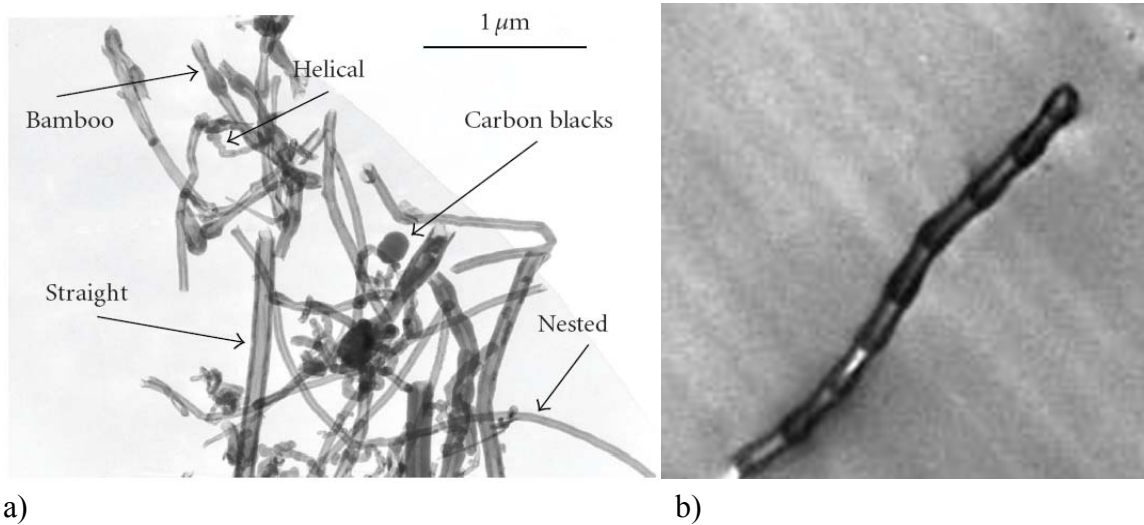


Figure 2.5 a) Different VGCNF morphologies resulted from the chemical vapor deposition process (Lafdi et al., 2007). b) View of a single bamboo-like VGCNF in VGCNF/VE nanocomposite.

Uchida et al. (2006) reported two main morphologies for VGCNFs (based on PR-24-HHT grade): 1) a single-layer morphology comprised of truncated stacked-cone (Dixie cup) microstructure, where graphene sheets comprising the cones have an angle of about 15° - 17° to the fiber axis, and 2) a double-layer morphology comprised of an inner stacked-cone microstructure and outer graphene sheet layers oriented along the nanofiber axis with angles of less than 10° . Transmission electron micrographs of the two VGCNF morphologies are shown in Figure 2.6 (Uchida et al., 2006).

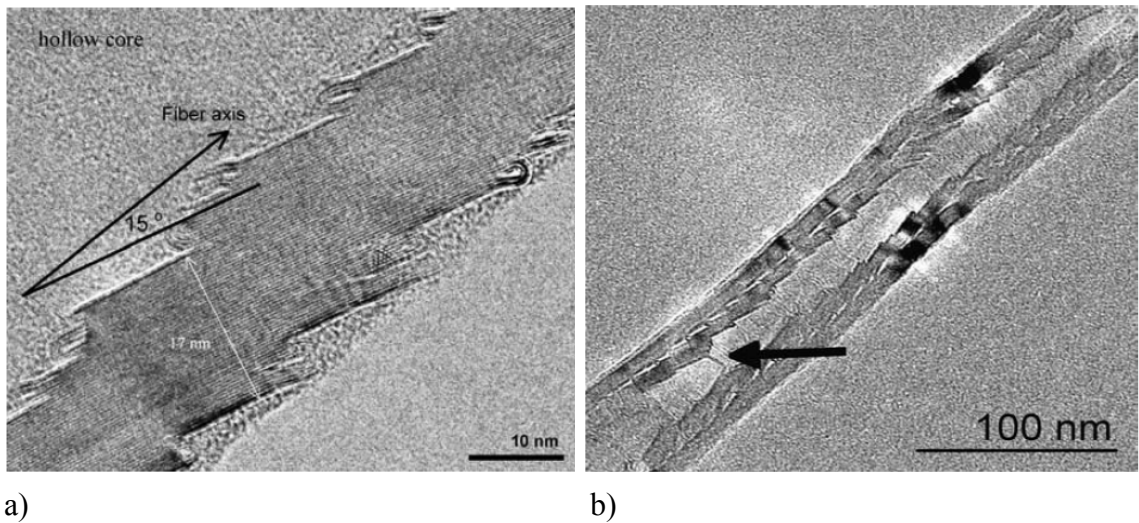


Figure 2.6 Transmission electron micrograph of a) a single-layer, and b) a double-layer VGCNF cross section (Uchida et al., 2006).

The stacked-cone microstructure is created during the nanofiber growth stage and depends largely on the size and shape of the catalyst particle (Endo et al., 2002). When fiber thickening takes place, an outer layer of “turbostratic” graphite is created, which is typically covered with amorphous carbon. The pyrolytic stripping process removes the amorphous carbon and tar, and the turbostratic carbon layer remains, yielding a relatively rough surface. Through heat treatment, the turbostratic layer is drastically reduced and graphitized, leading to a smoother nanofiber microstructure with higher mechanical properties (Endo et al., 2003; Özkan et al., 2010; Lau et al., 2010).

2.1.4. Mechanical Properties

The distinguishing characteristic of VGCNFs compared to traditional micro-sized carbon fibers is their smaller size, with diameters typically in the 70-200 nm range (Pyrograf Products, 2011). Therefore, they possess fewer structural defects (Wagner &

Vaia, 2004; Podsiadlo et al., 2007) and provide for large interfacial area for nanoreinforcement/matrix contact (Schadler et al., 2007). However, their mechanical characterization is not always straightforward. Currently, few characterization techniques are available for nanofibers, nanotubes, nanorods, and other filamentous nanomaterials (Tan & Lim, 2006). These include nano-tensile, nano-bend, and nano-indentation tests using atomic force microscopy (AFM). Despite these limitations, there are literature data for the mechanical properties of VGCNFs. Tibbetts et al. (1987) used a micro-tensilemeter to measure the tensile strengths and moduli of VGCFs with a diameter of 7.5 μm . Values of 2.92 GPa and 237 GPa were reported for the average VGCF tensile strength and modulus, respectively. Furthermore, improvements in the mechanical properties were observed as the VGCF diameter decreased. These improvements were attributed to a more complete graphitic ordering at lower diameters. Patton et al. (1999) made estimates of the flexural moduli and strengths (lower limits) of Pyrograf®-III nanofibers using VGCNF/epoxy nanocomposites. Values of 150-166 and 4-5.1 GPa were reported for the flexural moduli and strengths, respectively.

The mechanical properties of VGCNFs depend on the microstructure resulting from the growth process (see section 2.1.1) and post-fabrication treatments that alter the amorphous carbon content on the nanofiber surface, the turbostratic layer thickness, and the iron content. Wei and Srivastava (2004) defined four different structural parameters for a single nanocone: inner diameter, outer diameter, length, and tilting angle. Continuum elasticity theory was used to derive an expression for the Young's moduli of single, multi-shell, and stacked-cup VGCNFs, which were validated using MD simulations. Based on their calculations, nanofiber attributes of shorter cone length and

smaller tilting angle result in a higher Young's modulus. During tensile loading, a strain stiffening behavior (up to 28% increase in the Young's modulus) is typically observed as a result of a better graphitic layer orientation in the load direction (Morgan, 2005). The typical mechanical properties of VGCNFs are compared to CNTs and traditional micron-sized carbon fibers in Table 2.1.

Table 2.1 Typical properties of carbon filamentous materials (Koyama, 1972; Tibbetts & Beetz, 1987; Applied Sciences, 2011; O'Connell, 2006; Kang et al., 2006).

Property	SWCNT¹	DWCNT²	MWCNT³	VGCNF	VGCF	PAN⁴ Carbon Fiber
Typical Diameter (μm)	~0.001	~0.005	~0.02	0.06-0.2	0.005-0.05	0.005-0.01
Typical Length (μm)	~0.2	~0.5	1-50	50-100	50-100	1,000-5,000
Density (g/cm ³)	1.3-1.5	~1.5	1.8-2.0	1.9-2.1	~1.8	1.7-2.2
Tensile Modulus (GPa)	~640	-	~1060	50-775	160-760	150-950
Tensile Strength (GPa)	-	23-63	-	3-20	1-3	4-7
Elongation at Break (%)	~5.8	~28	-	-	-	0.5-2.5

¹ Single-walled carbon nanotube

² Double-walled carbon nanotube

³ Multi-walled carbon nanotube

⁴ Polyacrylonitrile

2.2. Vinyl Ester Resin

The composite industry consumes three commodity thermosetting resins in significant amounts: unsaturated polyester, VE, and epoxy. VE resin was introduced in the mid 1960s (Bruins, 1976). Various VE resin grades are widely used in the automotive industry. The automotive applications include body panels, firewalls, fuel cell plates, headlamp components, and radiator supports among others (Harper, 2002). These applications take advantage of VE resin's superior physical and mechanical properties including dimensional stability, strength, toughness, high service temperatures, and chemical and corrosion resistance (Goodman, 1998; Harper, 2002). McConnell has an excellent article on VE resins, their chemistry, growing composite markets, applications, and related research with focus on the fundamental and applied research on VE matrix-based nanocomposites at Mississippi State University (McConnell, 2010). This work is part of the research efforts mentioned in McConnell's article. A review of VE's chemistry and synthesis, curing, and properties is given next.

2.2.1. Chemistry and Synthesis

VE resins are synthesized through the addition reaction between various epoxy resins or diepoxides, such as diglycidyl ether of bisphenol A, and unsaturated monocarboxylic acids, most commonly methacrylic or acrylic acid (Goodman, 1998; Li, 1998). The ring opening reaction of the epoxy group with the carboxylic acid takes place at moderately high temperatures (120-150 °C) in the presence of a catalyst. Suitable catalysts include tertiary amines, phosphines, and onium salts (Goodman, 1998). Figure

2.7 shows a schematic of the reaction between a diglycidyl ether of bisphenol A and methacrylic acid to form a VE oligomer (Bruins, 1976).

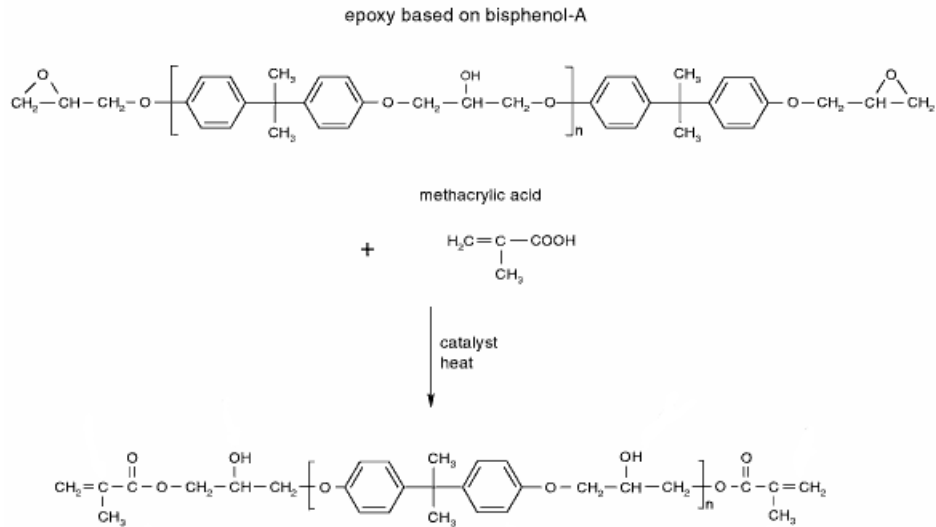


Figure 2.7 Reaction between a diglycidyl ether of bisphenol A and methacrylic acid to form a VE oligomer (Bruins, 1976).

The VE oligomer has very reactive unsaturated (double) bonds at each end of the molecule, which can undergo a homopolymerization reaction with other VE oligomers or participate in copolymerization reactions with other unsaturated co-monomers like styrene, para-methyl styrene, vinyl toluene, or methyl methacrylate (Li, 1998). If bi- or trifunctional epoxy resins are used to synthesize VE oligomers, multiple unsaturated bonds will exist at either end of the VE oligomer. The polymerization reaction (curing) gives rise to a three dimensional (3D) crosslinked system.

Styrene is the most commonly used co-monomer in industrial-grade VE resin systems (Goodman, 1998). It is added to the VE resin, typically in amounts of 30-50 wt%, to reduce the room temperature viscosity of the resin to 200-2000 cP (Li, 1998).

The VE molecular weight can be tailored by the choice of the epoxy backbone (Goodman, 1998). For most composite applications, two moles of diglycidyl ether of bisphenol A are reacted with one mole of bisphenol A to extend the epoxy backbone chain for tailored mechanical properties (Goodman, 1998).

2.2.2. Curing

To achieve a solid material, liquid VE resin must undergo curing. VE resins are most commonly cured through peroxide-initiated free radical polymerization (Shonaike & Advani, 2003), although curing by electron beam, ultraviolet, and ionizing beam irradiation are also employed (Lopata et al., 1999; Endruweit et al., 2006). The initiators are typically organic peroxides, such as methyl ethyl ketone peroxide (MEKP) and benzoyl peroxide (BPO), or hydroperoxides, such as cumene hydroperoxide (CHP) (Ashland, 2005). These compounds decompose either by application of heat or through a room temperature reduction-oxidation reaction with a metal promoter like cobalt naphthenate (CoNap) or cobalt octoate (CoOct) (Shonaike & Advani, 2003). CoNap is available as a 6%, 12%, or 21% solution of active cobalt in a solvent, but the 6% solution is typically used with epoxy VE resins (Ashland, 2005). The use of accelerators like *N,N*-dimethylaniline (DMA), *N,N*-diethylaniline (DEA), and *N,N*-dimethylacetoacetamide (DMAA) in small quantities can accelerate the curing reaction, while the use of retarders like 2,4-pentanedione (acetylacetone) can delay the “gelling” of the VE resin (Ashland, 2005). Once free radicals are formed, they attack the unsaturated sites on the terminal methacrylate groups of the epoxy backbone as well as the unsaturated styrene molecules, and the polymerization reaction begins. Three reactions can occur, each possessing

different kinetic rate constants: 1) methacrylate-methacrylate homopolymerization, 2) methacrylate-styrene copolymerization, and 3) styrene-styrene homopolymerization (Shonaike & Advani, 2003). Figure 2.8 shows a schematic of VE curing (Li, 1998). As the reaction proceeds, a gel (semi-crosslinked system) is formed and further crosslinking becomes diffusion-controlled (Li, 1998). “Gelation” is the point where a polymer of infinite molecular weight is formed. Later in the curing process, the “vitrification” point is reached, where the glass transition temperature (T_g) of the thermoset system is equal to the cure temperature (Li, 1998). The kinetics of VE curing depend strongly on the formulation and processing conditions (Abadie et al., 2002). An excellent review on the kinetics of thermoset resin curing is given by Yousefi et al. (1997).

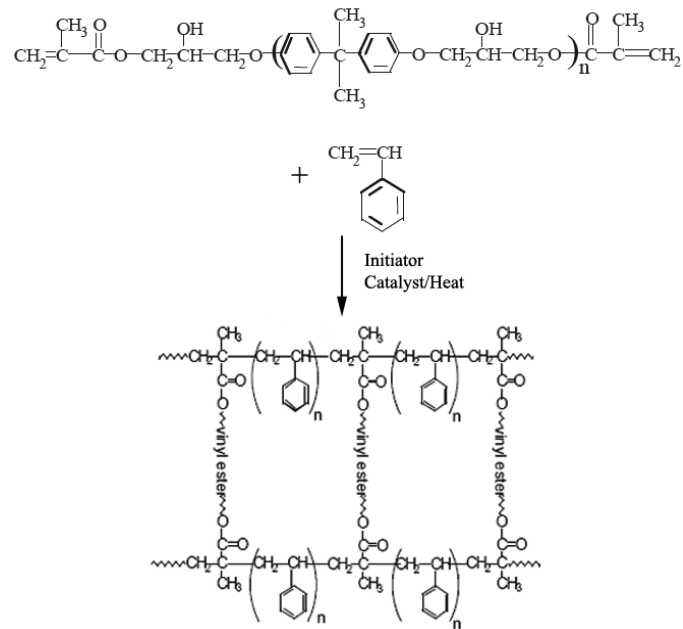


Figure 2.8 Curing of VE oligomers with styrene (Li, 1998).

The formulation of VE resins often contains other components. For example, the mixing process and the use of MEKP with 6% CoNap solution typically results in foaming of the resin; hence, surfactants and antifoam agents are added to eliminate the air bubbles (Ashland, 2005). Thixotropic additives (flow control agents) are sometimes used to control the flow of the resin. Ultraviolet absorbers can shield against degrading by ultraviolet radiation (Goodman, 1998).

2.2.3. Physical and Mechanical Properties

VE resin has the processability of polyester resin, yet at the same time possesses mechanical properties comparable to epoxy (Ratna, 2009). Some of the chemical groups present on the backbone of the VE oligomer impart certain physical and mechanical properties to the final cured resin (Goodman, 1998; Shonaike & Advani, 2003). Aromatic rings contribute to the toughness, mechanical properties, and heat resistance of the cured resin. VE resin has ester linkages in the terminal positions of the VE oligomer and phenyl ether linkages in the epoxy backbone. The presence of the relatively bulky methyl group in the proximity of the ester linkages sterically hinders the hydrolysis of the chain through chemical attack and thus, VE resin has excellent chemical and corrosion resistance (Goodman, 1998). The structure of the VE resin can further be modified through reactions with the pendant hydroxyl groups in the epoxy backbone (Shonaike & Advani, 2003). Furthermore, these hydroxyl groups can hydrogen-bond with the surfaces of reinforcements in composites. One of the unique features of VE resins is the presence of double bonds in the terminal positions of the VE oligomers, which make it possible to better control the crosslink density (Li, 1998). In contrast, unsaturated polyesters have

double bonds distributed along the entire polymer backbone, giving rise to a more random crosslinking pattern. Therefore, the mechanical properties of VE systems are superior to unsaturated polyesters, but inferior to epoxies.

Addition of styrene to VE resin can affect the ultimate mechanical properties of the resulting crosslinked system. Varma et al. (1985) systematically varied the styrene concentration in VE resin from 20 to 60 wt%. A marginal change in the curing characteristics of the resin, a decrease in the tensile modulus, an increase in the elongation, and a decrease in the T_g of the neat resin cast and glass fiber-reinforced laminates were observed with increasing styrene content in the resin.

2.3. VGCNF/Polymer Nanocomposites

The use of VGCNFs can lead to a variety of improvements in thermal conductivity (Elgafy & Lafdi, 2005; Kumar et al., 2007; Agarwal et al., 2008; Moore et al., 2009), dielectric properties (Yang et al., 2007b), electrical conductivity (Wang & Alexander, 2004; Xu et al., 2005; Kumar et al., 2007; Jimenez & Jana, 2007; Wu et al., 2007; Sui et al., 2008; Allaoui et al., 2008; Al-Saleh & Sundararaj, 2009; Bal, 2010; Morales et al., 2010), electromagnetic interference (EMI) shielding (Yang et al., 2007; Nanni et al., 2009; Al-Saleh & Sundararaj, 2010), fire (flame) retardancy (Zhao & Gou, 2009; Morgan & Liu, 2010), and mechanical properties of the host thermoplastic and thermoset polymer matrices. Since the focus of this work is on the mechanical property enhancement of the matrix, a detailed review of this subject will be given next.

2.3.1. Fabrication

To date, the expected mechanical property enhancements of VGCNF-based nanocomposites have typically not been realized because of the agglomerated nature of VGCNFs, the randomness of their 3D orientation (Tibbetts et al., 2007), their curvature, their poor interfacial adhesion to the matrix, and their structural defects. These are all consequences of the inherent characteristics of nanofibers produced and dispersed using currently available manufacturing methods.

2.3.1.1. Nanofiber Dispersion and Interfacial Adhesion

The level of mechanical property improvement possible through the incorporation of VGCNFs in various matrices depends on the level of available interfacial contact (load transfer area) and the strength of interfacial adhesion between the nanofibers and the matrix. Though these nanofibers possess high surface area-to-volume ratios (Endo et al., 2001), this unique attribute of the nanofibers will not be fully utilized unless the matrix can completely wet the entire VGCNF surface area (McHugh & Tibbetts, 1998). Nanofiber agglomeration is a serious obstacle for achieving complete wetting-out of the nanofiber surface and prevents a high degree of nanofiber-matrix interfacial contact.

Two main mechanisms contribute at the nano- and micro-scale resulting in agglomeration of VGCNFs: 1) mechanical interlocking of high aspect ratio nanofibers, which is a direct result of the growth mechanism (Baker et al., 1972) during nanofiber fabrication, and 2) strong van der Waals interactions between the individual nanofiber surfaces. The interlocking (entanglement) of nanofibers occurs at a higher length scale than the van der Waals interactions. The nanofibers typically undergo a debulking

process after fabrication for a more uniform bulk density to allow a more homogeneous compounding with different matrices (Pyrograf Products, 2011; Tibbetts et al., 2007). However, this process results in bundles of agglomerated VGCNFs and possible fiber shortening (decreased aspect ratio) (Pyrograf Products, 2011). Figure 2.9 shows scanning electron micrographs of VGCNF agglomerated structures (clusters), which have undergone two different debulking methods by Applied Sciences Inc. The loose structure (XT®) may possess better dispersion characteristics (Pyrograf Products, 2011).

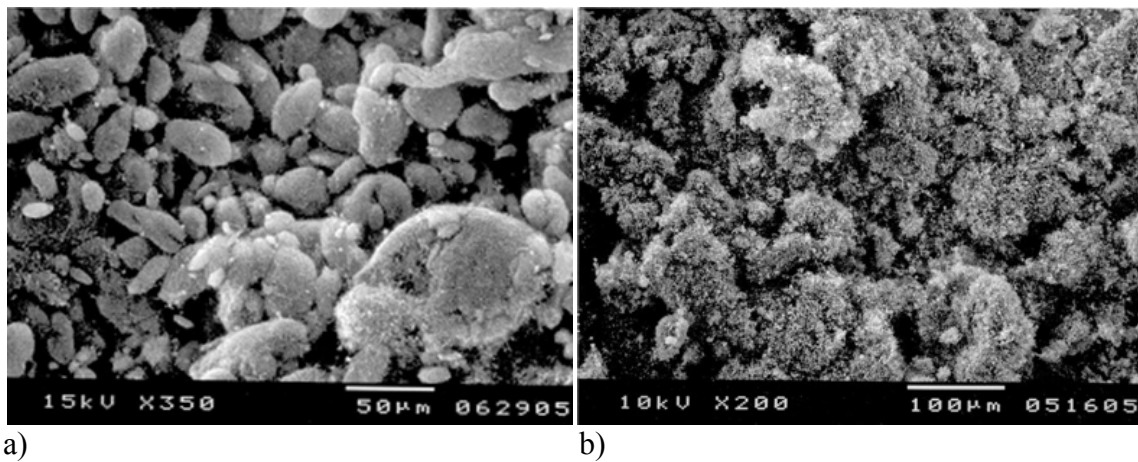


Figure 2.9 a) An earlier debulking process employed by Applied Sciences Inc. yielding large VGCNF agglomerated structures difficult to disperse in various polymer matrices, b) XT® debulking process yielding loose VGCNF agglomerates easier to disperse (Pyrograf Products, 2011).

Measures have been applied to facilitate VGCNF agglomerate break-up and dispersion in matrices. These measures use physical, mechanical, or chemical means to disentangle the nanofibers locked in the agglomerates, overcoming their attractive forces, and preventing their re-agglomeration once dispersed in the medium of interest. Often, a combination of all these measures is necessary to achieve acceptable levels of nanofiber

dispersion. The mechanical route to nanofiber dispersion involves applying energy to the nanofiber agglomerates through vibration or shearing action. Ultrasound sonication (i.e., ultrasonication) is one such technique that is widely used for the dispersion of nanoreinforcements in a variety of matrices. This technique applies ultrasonic energy at a typical frequency of 20 kHz to a suspension of nanofibers, which leads to the disintegration of nanofiber agglomerates through “cavitation” (creation and collapse of air bubbles) or resonance excitation of the agglomerated structures (Gibson et al., 2007). It is available in two varieties: tip sonication and bath sonication. In the tip sonication, an ultrasonic tip (wand or horn) is submerged in the nanoreinforcement/matrix blend, while in bath sonication, the blend is immersed in an ultrasound bath. The amplitude, power, irradiation mode (continuous or pulsed), and duration of sonication are parameters that affect the level and efficiency of dispersion. Studies show that longer durations of sonication may lead to nanoreinforcement shortening (Gibson et al., 2007) and reduced mechanical properties of the final nanocomposite (Kabir et al., 2007). The use of ultrasonication often requires a primary step of dispersing the nanofibers in a solvent, such as acetone or alcohol, and a secondary step of adding the solution to the matrix and removing the solvent. Therefore, the nanocomposite fabrication process may become tedious with various complications related to solvent removal. It is also difficult to apply on a large industrial scale.

Shear can be applied to the nanofiber/matrix blend through different means. In thermoplastic matrix nanocomposites, a single (Hasan et al., 2007) or twin-screw extruder (Carneiro et al., 1998; Sandler et al., 2002; Zeng et al., 2004; Choi et al., 2006; Ren et al., 2008; Vidhate et al., 2009) is often used. The nanofibers are added directly or

in the form of a “masterbatch” to the extruder. The level of dispersion achieved this way is highly dependent on the geometry of the screw(s) (and possible mixing elements), extrusion time (screw rotation speed), and temperature. All these parameters define the amount of shear that is applied to the nanofiber agglomerates. In resin systems, high-shear mechanical mixers are typically used. Among these are the ball mill (Tibbetts & McHugh, 1999; Tibbetts et al., 2002), the two roll mill (Patton et al., 1999; Xu et al., 2000; Patton et al., 2002), the three roll mill (calendar) (Yasmin et al., 2003; Park et al., 2008; Ji & Li, 2008; Thostenson et al., 2009), the thermokinetic mixer (Faraz et al., 2010), the chaotic mixer (Jimenez & Jana, 2007), the internal mixer (Lozano & Barrera, 2001; Ma et al., 2003; Xu et al., 2004), and the screen/blade high-shear mixer (Nouranian et al., 2009). The viscosity should be relatively low to allow proper mixing by these methods.

One chemical route to nanofiber dispersion involves the use of surfactants and dispersing agents to lower the nanofiber surface tension and prevent nanofiber re-agglomeration. This is achieved by keeping the nanofiber surfaces at a distance away from each other, where van der Waals forces will not reaggregate them. Surfactants are widely used in clay nanocomposites to improve the intercalation of clay tactoids (Jang et al., 2005; Bellucci et al., 2008). They are also used in other nanocomposites as dispersion aids (Liao et al., 2004; Xia & Song, 2005; Zhang et al., 2007; Cho et al., 2008; Zhang et al., 2009; Ciecierska et al., 2010).

Surface functionalization of VGCNFs is another chemical modification aimed at decreasing the surface energy of nanofibers and, hence, reducing the nanofiber-to-nanofiber attractive forces. Many functional groups on the nanofiber surface not only

reduce the strong van der Waals forces between nanofibers, but also improve the nanofiber-to-matrix interactions (interfacial adhesion) in many systems. This leads to better nanofiber dispersion, improved load transfer characteristics, and ultimately enhanced nanocomposite mechanical properties (Finegan et al., 2003). The choice of the functional groups is crucial in order to maximize the compatibility between the nanofibers and the matrix. A detailed review of various functionalization techniques is given in section 2.1.2.

The micro- and nano-scale interactions between nanofibers and matrix molecules at the interface often result in an “interphase” region (Jancar, 2009) surrounding each nanofiber, where matrix properties are different from those of the bulk matrix and mostly change in a gradient fashion (Vaia & Giannelis, 2001; Jancar, 2008). The nature of interactions (attractive or repulsive) depends primarily on the chemistry of the matrix and nanoreinforcement and the arrangement of molecules in the proximity of the interface at the nano-scale. In thermoplastics, attractive interactions are often observed. The segmental immobilization of polymer chains and other changes in polymer dynamics at the nanofiber-polymer interface is therefore the main phenomenon resulting in the formation of the interphase with its gradient properties (Jancar, 2008; Qiao & Brinson, 2009). The retarded motion of polymer chains leads to morphological changes manifesting as different levels of crystallinity, lamellae size and orientation, chain entanglement density, charge distribution, and free volume adjacent to the surface. This induces different polymer physical and mechanical properties compared to the bulk polymer (Schadler et al., 2007). In thermosets, the interactions between chemical constituents of the resin and the nanofiber surface right before crosslinking might lead to

different interfacial molar ratios of the constituents compared to the bulk. The resulting crosslinked network may therefore have a different crosslink structure and density in the interphase region. Hence, a gradient may develop in mechanical properties (Schadler et al., 2007). The interphase thickness and its mechanical properties depend on the size of the inclusions and need to be included in a realistic mechanical modeling of nanocomposites (Montazeri & Naghdabadi, 2010).

Currently, few methods are available to assess the level of nanoreinforcement dispersion in a particular system. The majority of these methods are qualitative and do not provide means of comparing dispersion among different systems. Transmission electron microscopy (TEM) and scanning electron microscopy (SEM) (Kornmann et al., 2001; Morgan & Gilman, 2003; Yoonessi et al., 2005; Luo & Koo, 2008; Ciecierska et al., 2010; Khare & Burris, 2010), small-angle X-ray scattering (SAXS) and wide-angle X-ray scattering (WAXS) (Fratzl, 2003; Vermogen et al., 2005), small-angle neutron scattering (SANS) (Schmidt et al., 2002; Fratzl, 2003; Shibayama et al., 2005; Yoonessi et al., 2005), X-ray diffraction (XRD) (Kornmann et al., 2001), and nuclear magnetic resonance (NMR) (VanderHart et al., 2001; Bourbigot et al., 2008) are common techniques widely used for qualitative and quantitative dispersion studies. Some researchers have also attempted to use stereology as a means to quantify the dispersion of inclusions in a 3D media (Luo & Koo, 2007 and 2008).

2.3.1.2. Nanofiber Alignment

Once dispersed, the nanofibers will have a 3D random orientation in the matrix. The effective use of the anisotropic characteristics of VGCNFs can be realized if the individual nanofibers are aligned in a preferred orientation. Through alignment, more nanofibers are capable of bearing a greater amount of applied load and the nanocomposite's mechanical properties are further improved. The flow of a polymer melt containing randomly oriented CNT or CNF nanoreinforcements in single- or twin-screw extruder and injection molding machines leads to partial alignment of the fibers as the melt is sheared. Further alignment can result if the extrudate is forced through a die. The extrusion process can be repeated to apply desired cycles of shearing action and, hence, achieve different levels of nanoreinforcement alignment (Hine et al., 2005). This shear- and flow-induced alignment is further enhanced by drawing the melt after the extrusion step (mechanical stretching) (Jin et al., 1998; Thostenson & Chou, 2002; Sennett et al., 2003; Siochi et al., 2004). Similar shear-induced orientation can be obtained in other processing machines, such as roll mills (Kim et al., 2006). These methods are all applicable to commodity thermoplastics and rubbers, where the inherent shear-dominated characteristics of their processing allow for effective manipulation of CNT/CNF alignment in the desired orientation. When preparing polymer nanocomposite films by film blowing, a preferred CNT/CNF orientation can be achieved through the bubble stretching mechanism (Dalton & Jurewicz, 2007). Because of the electron conductivity of CNTs/CNFs, electric (Chen et al., 2001; Park et al., 2006) and magnetic fields (Kimura et al., 2002; Garmestani et al., 2003; Takahashi et al., 2007) can often be used during the nanocomposite processing to induce alignment in a desired orientation. Figure 2.10

shows a schematic of different nanofiber alignment patterns in electric and magnetic fields described by Takahashi and Yonetake (Gupta et al., 2010).

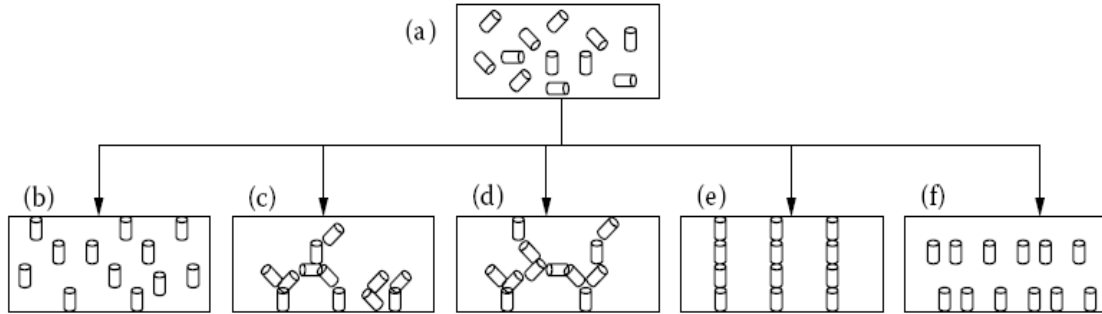


Figure 2.10 A schematic of different nanofiber alignment patterns in a polymer matrix, where a) is the randomly oriented pattern; b) is the pattern created by magnetic processing; c) and d) are patterns created by the DC electric field; e) represents patterns generated by the AC electric field; and f) shows patterns created by a magnetic field with a magnetic modulator (Gupta et al., 2010).

Electrospinning (electrostatic spinning) (Doshi & Reneker, 1995) is a method of polymer fiber fabrication from solutions by the use of electric charges (Figure 2.11) that has recently been used as means for aligning CNTs in polymer nanocomposites (Huang et al., 2003). CNTs are believed to become aligned along the fiber direction during spinning due to a combination of dielectric and high-shear forces. However, this only leads to an in-fiber orientation in an otherwise non-woven fiber nanocomposite. Many attempts have been made to prepare aligned fiber nanocomposites through methods such as high-speed cylindrical fiber collection, the use of auxiliary electrode/electrical field, the use of a thin wheel with sharp edge, and the use of a frame collector (Huang et al., 2003).

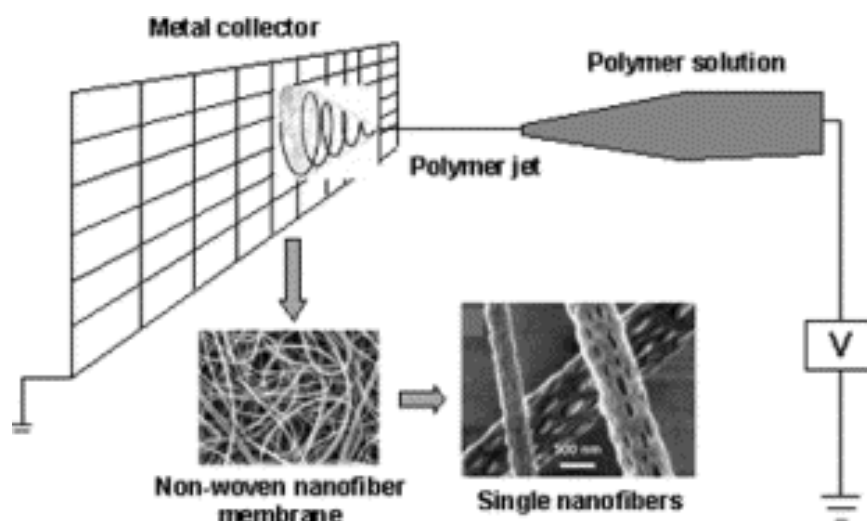


Figure 2.11 Electrospinning process for the fabrication of polymer or nanocomposite fibers (Huang et al., 2003).

2.3.2. VGCNF/Thermoplastic Matrix Nanocomposites

Since VGCFs and VGCNFs became commercially available, numerous attempts have been made to assess the feasibility of exploiting these materials as means to improve the mechanical properties of a variety of thermoplastics with varying results. Carneiro et al. (1998) used a co-rotating intermeshing twin-screw extruder and injection molding to prepare nanocomposites of 5, 10, 20, and 30 wt% of pristine and plasma-treated VGCNFs (Pyrograf®-III) in PC. Tensile and impact tests were conducted on the injection molded specimens of both nanocomposite types. The tensile modulus of the neat PC was increased in a nearly linear fashion by the addition of pristine VGCFs. An increase of 39% in the storage modulus and 17% in the yield stress through the addition of 20 wt% VGCF to the neat PC were reported. The processing and molding procedures were later optimized and a 72% increase in the tensile modulus and 19% increase in the yield stress

were obtained for the same VGCF weight fraction. This clearly showed the processing dependency of polymer/VGCF nanocomposite properties. The impact strength properties degraded through the addition of VGCFs, which were attributed to the poor nanofiber-matrix addition. This issue was alleviated using plasma-treated VGCFs, but only a slight improvement in the impact strength was observed, which was still much lower than the neat PC. It was deduced that the VGCF surface treatment had little influence on the mechanical performance of PC.

Sandler et al. (2002) mixed Pyrograf®-III VGCNFs with semi-crystalline thermoplastic matrix systems, poly(ether ether ketone) (PEEK) and polypropylene (PP) in the amounts of 5, 10, and 15 wt% for PEEK and 7 wt% for PP using conventional polymer processing machines (injection molding and twin-screw extrusion). The tensile properties of the nanocomposites were measured and a 40% increase in the tensile modulus of PEEK was observed as the VGCNF weight fraction increased to 15 wt%. Furthermore, a 110% increase in the modulus of PP was observed as the VGCNF weight fraction increased to 7 wt%. The tensile strength of PEEK increased by 50%, while no significant change was observed for PP. Differential scanning calorimetry (DSC) revealed that the degree of crystallinity and the crystalline structure of the polymer matrices did not change in the presence of VGCNFs.

Choi et al. (2006) used two different techniques to prepare nanocomposites of PC with 1, 10, 15, and 25 wt% VGCF. In one technique, suspensions of dispersed VGCFs in PC/tetrahydrofuran (THF) solutions were prepared. Then the suspensions were cast, dried in the oven, and finally made into compact sheets using a hot press machine. Another technique utilized a twin-screw extruder to apply high shear to the VGCF/PC blend,

followed by compacting the nanocomposite sheets using a hot press, and finally rolling the sheets to achieve the desired thicknesses. A slight initial increase in the tensile strength to 10 wt% VGCF, followed by a decrease in the tensile strength (even to lower values than the neat PC for the solution-cast sheets) at higher nanofiber weight fractions was reported. The rolled sheets gave slightly higher tensile properties. However, the tensile modulus was steadily increased to almost 70% of that of the neat PC at 25 wt% VGCF.

Yang et al. (2007a) mixed high-density polyethylene (HDPE) with 20 wt% Pyrograf®-III VGCNF in a high-shear mixer and prepared VGCNF/HDPE nanocomposites to study the effects of aligning carbon nanofiber in VGCNF nanocomposites. Specimens were hot-pressed and extruded with different draw ratios. A 55% and 82% increase in the storage modulus at 25 °C were determined by dynamic mechanical analysis (DMA) for specimens containing 20 wt% VGCNF drawn with take-up speeds of 10 and 30 rpm, respectively. An increase in the loss modulus was also observed. This behavior was attributed to VGCNF alignment during extrusion at higher draw ratios.

Ren et al. (2008) prepared nanocomposites of 0.5, 1, and 3 wt% VGCNF in a mixture of ultra-high molecular weight polyethylene (UHMWPE) with low-density polyethylene (LDPE) (3:7 ratio by weight) using a twin-screw extruder. A non-linear increase in the tensile strength was observed with the addition of VGCNFs to a maximum of 38% at 3 wt% VGCNF. The modulus increased by 15% at 3 wt% VGCNF. Dynamic mechanical properties of the nanocomposites showed slight variations without significant improvement in the storage modulus compared to the neat UHMWPE/LDPE blend.

In another study, Lee et al. (2010) blended 1-35 wt% of three different VGCNFs (PR-19-PS, PR-24-PS, and laboratory-made) with linear low-density polyethylene (LLDPE) in an intensive mixer and hot-pressed nanocomposite specimens. An increase of 173% in the tensile modulus at 15 wt% PR-grade VGCNFs, insignificant change in the tensile strength, and a drop in the strain-to-failure value from 690% to 120% for the PR-grade VGCNFs were reported.

Chávez-Medellín et al. (2010) prepared nanocomposites of polyamide-12 and nitric acid-oxidized VGCNFs (PR-24-AG) in 0.1, 0.2, 0.5, 1.0, 2.5, and 5 wt% in a laboratory twin-screw extruder. The extrudates were re-pelletized, and the nanocomposite strands were injection-molded. A 40% increase in the room temperature storage modulus at 1 wt% VGCNF was measured by DMA. Furthermore, a decreased elongation at break and a slight improvement in the yield stress were observed.

VGCNFs have modified polymer fiber properties. Sandler et al. (2004) used nanofiber (PR-19 VGCNF) in 5, 10, and 15 wt% in polyamide-12 to melt-spin reinforced nylons in a twin-screw micro-extruder. A linear increase in the initial stiffness and yield strength was observed as a function of nanofiber weight fraction. Furthermore, an 80% increase in the tensile modulus occurred at 15 wt% VGCNF.

PR-21 and PR-24 VGCNF/poly(methyl methacrylate) (PMMA) blends were converted to rods or fibers by Zeng et al. (2004) through melt-mixing in a counter-rotating twin-screw extruder and subsequent extrusion/fiber spinning. The tensile properties of these nanocomposite rods and fibers were measured at two VGCNF weight fractions (5, and 10 wt%) and were compared to those of the neat PMMA. An increase of

50% in the tensile modulus at 5 wt% VGCNF, and a slight improvement at 10 wt% VGCNF were reported. The tensile strength and elongation were slightly reduced.

Vidhate et al. (2009) melt-blended polyvinylidene fluoride (PVDF) with 0, 1, 2, and 4 wt% VGCNF (PR-24-XT-LHT) in a co-rotating twin-screw extruder and pulled the nanocomposite extrudate with a speed of 230 rpm to form fibers with induced nanofiber orientation. An increase of 122% in the yield strength and 88% in the tensile modulus were reported with the addition of 4 wt% VGCNF, while the elongation at break decreased. This decrease was attributed in part to changes in the matrix crystal structure. The storage moduli of the VGCNF/PVDF nanocomposites were higher than that of the neat PVDF.

PP filaments reinforced with VGCNFs were produced by Hasan et al. (2007) through single-screw extrusion. Using only 0.5 wt% VGCNF, an increase of 154% in the tensile modulus and 69.5% in the tensile strength were reported. These observations were attributed to the VGCNF alignment during processing. Thermogravimetric analysis (TGA) of the nanocomposite filaments exhibited an 18.9 °C increase in the decomposition temperature.

George et al. (2008) prepared nanocomposites of PR-24 VGCNF in elastomers-grade ethylene vinyl acetate (EVA) (50% vinyl acetate content). Pristine fibers and fibers surface-treated by electron beam irradiation, gamma irradiation, H₂SO₄/HNO₃ acid treatment, hexamethylene diamine treatment, and vinyl silane treatment were used. Quasi-static tensile testing and DMA were conducted on specimens containing 1, 4, and 8 wt% pristine VGCNFs and 1 wt% surface-functionalized VGCNFs. Increases in the tensile strength of 61% at 1 wt% and 125% at 4 wt% pristine VGCNFs were observed,

while a decline was reported for 8 wt% VGCNFs due to nanofiber agglomeration. The tensile modulus also increased by 350% at 4 wt% and 520% at 8 wt% pristine VGCNF. The surface treatment yielded better nanofiber-to-matrix interfacial adhesion and better dispersion in the elastomer, which was confirmed using swelling studies. This ultimately led to better mechanical properties compared to those of the untreated nanofibers. The best overall mechanical property improvement was observed for 1 wt% surface-modified VGCNF.

2.3.3. VGCNF/Thermoset Matrix Nanocomposites

Choi et al. (2005) prepared nanocomposite sheets of 3, 5, 7, 10, and 20 wt% VGCNF in low and high viscosity epoxy. Dynamic mechanical data showed a T_g increase of 26 °C for the epoxy at 20 wt% VGCNF in the low viscosity resin, while a decrease was observed for the high viscosity resin. This decrease in the T_g was ascribed to the poor interaction between the filler and the epoxy due to the presence of voids and poor VGCNF dispersion in the nanocomposites. The storage modulus increased with increasing VGCNF weight fraction at 80 °C. Stress-strain analysis indicated an increase in the Young's modulus and tensile strength with the addition of VGCNFs to the epoxy. However, the highest increase was observed for the 5 wt% case because of a better dispersion of nanofibers in the matrix at this weight fraction, while for all VGCNF weight fractions, the strain-to-failure was reduced.

Zhou et al. (2007) investigated the effect of Pyrograf®-III VGCNFs on thermal and mechanical properties of SC-15 epoxy. 1, 2, and 3 wt% of VGCNFs were mixed in the epoxy using ultrasonication for half an hour and the system was cured at room

temperature for 24 hours. The nanocomposites were further post-cured at 100 °C for 5 hours. A steady increase in the nanocomposite's storage modulus was observed (up to 65%) as the VGCNF weight fraction increased to 3 wt%. A similar trend was observed for the nanocomposite's tensile modulus, which was strain rate sensitive: 19.4% increase in the modulus at 3 wt% VGCNF. The tensile strength showed a peak 17.4% increase at 2 wt% VGCNF. The fatigue performance of the nanocomposite was also highest at 2 wt% VGCNF. At the same weight fraction, a 32% increase in the fracture toughness was observed.

Faraz et al. (2010) dispersed 1 and 2 wt% VGCNF (PR-19-XT-LHT) in a bismaleimide resin (Homide® 250) using a high thermokinetic mixer. Nanocomposite specimens were compression-molded. Using DMA and tensile tests, an increase of 10 °C in the T_g of the nanocomposites and 53% in the storage modulus of 2 wt% VGCNF specimen were observed. On the other hand, the mechanical performance of the nanocomposites was not improved as evidenced by a 19% decrease in the tensile strength and only 11% increase in the tensile modulus of 2 wt% VGCNF specimen. This behavior was attributed to poor interfacial adhesion between the VGCNFs and the matrix and presence of nanofiber bundles acting as stress concentration points within the specimen.

Plaseied et al. (2008; 2009) measured and modeled the tensile, flexure, and creep behavior of VGCNF/VE nanocomposites. A 6% increase in the flexural modulus and strength of the neat VE was reported through the addition of 1 wt% functionalized VGCNFs.

Attempts have also been made to incorporate VGCNFs in less conventional high-tech thermosetting resins like polyimides (Ogasawara et al., 2004).

2.4. Dynamic Mechanical Analysis

DMA is a common technique to characterize the viscoelastic properties of polymeric materials (Menard, 1999). In this technique, an oscillatory force is applied to the test specimen in a variety of modes, such as flexure, tension, and compression. The force causes a sinusoidal stress in the specimen, which in turn gives rise to a sinusoidal strain (Figure 2.12). Through the measurement of the amplitude and the deformation at the peak of the sine wave and the phase lag between the stress and strain sine waves, properties such as modulus (will be defined later) and viscosity can be measured (Menard, 1999).

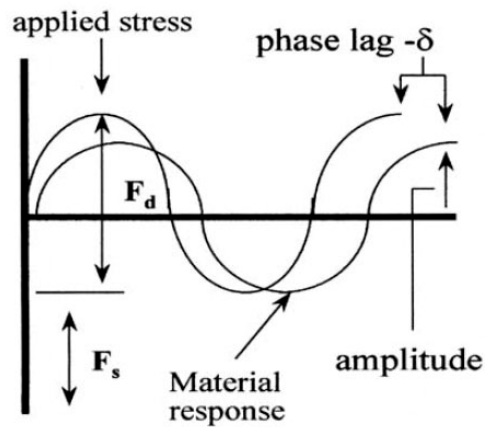


Figure 2.12 Applied oscillatory (dynamic) force (F_d) and the material response (oscillatory strain) in the dynamic mechanical analysis. F_s is the static (clamping) force and δ is the phase lag between stress and strain (Menard, 1999).

With DMA, it is possible to measure the modulus every time a sinusoidal wave is applied to the specimen using one of two modes. This measurement can be performed at a pre-determined frequency, while the temperature of the specimen is varied at some

desired rate. This mode is called “temperature sweep”. It is also possible to perform the test at a constant temperature, while the frequency of the oscillatory force is varied over some range (typically 0.01-100Hz). This mode is referred to as “frequency sweep”.

The modulus measured in DMA is not the same as the Young’s modulus calculated in quasi-static tensile, flexure, or compression tests (Menard, 1999). Here, a complex modulus (E^*) comprised of an elastic storage modulus (E') and an imaginary loss modulus (E'') is calculated. The storage modulus is a measure of the ability of the material to elastically store or return energy, while the loss modulus is a measure of the ability of the material to dissipate energy. The ratio between the loss and storage modulus is $\tan \delta$, which is referred to as “damping” (Figure 2.13).

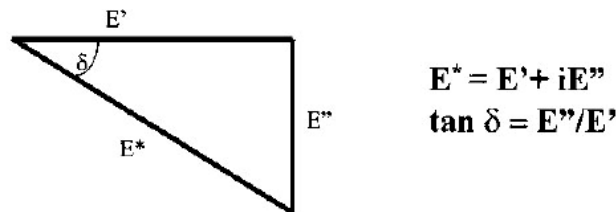


Figure 2.13 The relationship between storage modulus (E'), loss modulus (E''), and phase angle (δ). E^* is the complex modulus and $\tan \delta$ is damping (Menard, 1999).

The nature of DMA is to study the polymer relaxation phenomena or changes in the free volume (Menard, 1999). The relaxation of polymer chains through different chain movements and rearrangements at different temperatures leads to a variety of transitions. The most important of these transitions is the glass or α transition (T_g), where a huge decrease in the storage modulus (E') is observed. Figure 2.14 shows a general

curve for polymers where different transitions are shown (Menard, 1999). Some of these transitions may not be observed in certain thermoplastic or thermoset polymers.

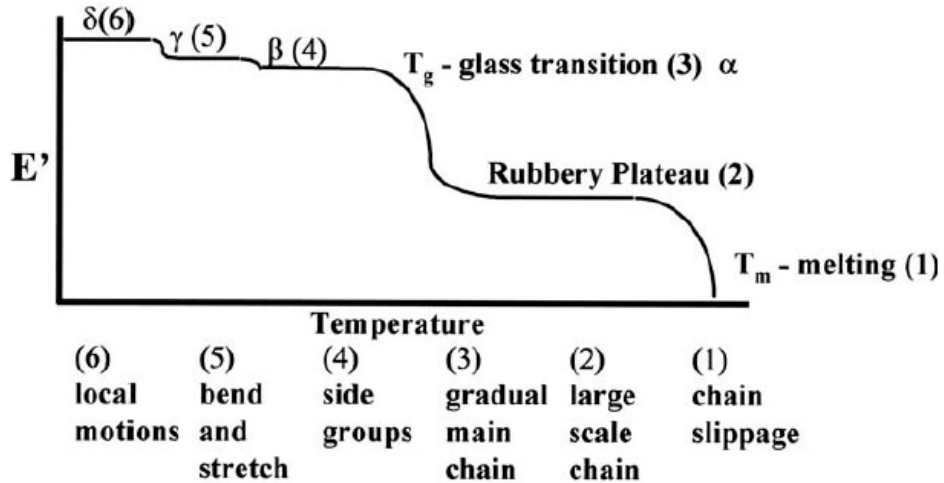


Figure 2.14 General description of the different transitions in polymers and the associated molecular motions responsible for them (Menard, 1999).

2.5. Design of Experiments

Knowledge about different systems of interest or phenomena is typically gained through experiments (Esbensen et al., 2010). Through experiments, the system is deliberately perturbed through changing of the independent variables, and the system responses are recorded. The data are then examined and fit to models. The selection of variables and responses are often based on previous experience and knowledge about the system, intuition, initial screening experiments, needs, and other factors.

Experiments can be conducted on an *ad hoc* basis (Esbensen et al., 2010), where based on the outcome of one experiment and previous experience, the next step in understanding the system is determined. This approach has many drawbacks: 1) a lack of

true knowledge about how the system really works makes the transfer of knowledge to other applications unreliable or impossible; 2) the variability in the results can often be mistaken for true information; and 3) the solution is most likely not optimal.

A traditional approach to experimentation is “one variable at a time” approach (Esbensen et al., 2010). As the name implies, only one variable is studied at any given time. Hence, no initial understanding exists about how many experiments are needed; no information can be obtained about the interaction between two variables; random variations cannot be distinguished from true effects of the variables; and no inferences and predictions can be made on the outcome of other experiments.

A better alternative to experimentation is the use of a designed experimental approach, where all desired variables can be studied at the same time with distinguishable experimental error having a minimal impact on the results (Cox & Reid, 2000; Montgomery, 2009). It is therefore possible to study both the effects associated with variables and their interactions. Furthermore, the total number of experiments is known from the beginning. When the results are obtained, a model-based mathematical analysis makes it possible to predict the outcome of any other experiment within the design space. A design of experiments consists of the following steps:

- 1) Selection of input (design) variables based on pre-defined objectives.
- 2) Selection of output (response) variables that have to be measured for each experiment.
- 3) Selection of different levels for each design variable pertaining to the range of variation desired for the study.
- 4) Selection of the appropriate design.

- 5) Running the experiments and collecting the data.
- 6) Analyzing the results through statistical tools and finding the significant effects.
- 7) Optimizing the system behavior.

2.5.1. General Full Factorial Design

Full factorial design is the most common experimental design where the whole experimental region of interest is explored yielding a maximum amount of information (Esbensen et al., 2010). The design variables are selected with their respective number of levels (referred to as general full factorial design) and combinations of all variables at all levels are used to define the set of experiments. The product of the number of levels of all design variables determines the number of total experiments required. In this design, all main effects of the design variables and all two-factor or higher order interactions are studied independent of each other. In this work, this design has been employed.

2.5.2. Terminology

Most of the terminology used in the design of experiments is standard statistical terms. However, some terms need further explanation in order to avoid confusion with terms common in other disciplines. A list of terminology follows (NIST, 2011):

- **Design of experiments:** a systematic, rigorous approach to problem-solving that applies principles and techniques of data collection as to ensure the generation of valid, defensible, and supportable conclusions. This is carried out under the constraint of a minimal expenditure of runs, time, and money.
- **Analysis of variance (ANOVA):** separation of the variability of a group of observations into assignable causes and setting up various tests to assess their significance. A standard ANOVA table contains information such as degrees of freedom, sum of squares, mean square, F -value, and p -value.

- **Factor:** input variable that the experimenter manipulates to cause a change in the output (response). This sometimes corresponds to input variable in the context of modeling.
- **Level:** a unique setting of a factor.
- **Response:** output of a process. It is also called the dependent variable.
- **Effect:** the result of a change in the setting of a factor on the response.
- **Interaction:** the effect of one factor on the response when this effect depends on the level of another factor or other factors.
- **Observation:** acquisition of information from the object of study.
- **Treatment:** factor levels whose effect is compared with other factor levels.
- **Treatment combination:** a combination of the settings (levels) of several factors in a single experimental trial. It is also called “run”.
- **Replication:** performing the same treatment combination more than once.
- **Error:** unexplained variation in a collection of observations.
- **Experimental error:** error associated with variations in response due to replications.
- **Sampling error:** error associated with variations in responses measured on samples from the same treatment combination.

2.5.3. Design of Experiments in Polymer Nanocomposites

Use of the design of experiments and optimization concept in the field of polymer nanocomposites has been limited. Yong et al. (2005) used factorial and response surface designs in order to study the effect of a coupling agent and a dispersing agent on the flexural properties of SiC/VE nanocomposites. Using a two-level full factorial design, the levels of additives were optimized and it was found that a better level of nanoparticle

dispersion did not necessarily lead to improved flexural properties. A good dispersion coupled with a strong filler-matrix interfacial bonding was the key to obtain enhanced flexural properties.

2.6. Molecular Dynamics Simulations of Polymer Nanocomposites

Because of large nanoreinforcement surface area-to-volume ratios, the volume fraction of interphase can be significant in polymer nanocomposites. Therefore, knowledge of the interphase and interfacial properties in these materials is crucial for mechanical modeling purposes (Montazeri & Naghdabadi, 2010). Due to the extremely small size of nanoreinforcements, direct measurement of mechanical properties at the interface is very difficult and expensive, if not impossible. Few researchers have attempted the direct measurement approach. Cooper et al. (2002) recorded a force-displacement trace for carbon nanotube pullout from an epoxy matrix using the tip of a scanning probe microscope (SPM). Detaching a single nanotube at the location of a suitable “hole” in the polymer, the interfacial shear strength was calculated by dividing the recorded pullout force by the interfacial area of the embedded nanotube. However, this technique is not faultless. Nanotube bending or breakage, unsheathing of inner from outer tube layers in multi-walled carbon nanotubes (MWCNTs), and other phenomena pose a challenge to the validity of such measurements. In a later attempt, Barber et al. (2003) used AFM to measure nanotube detachment force versus time. Their approach was similar to Cooper’s. Other methods have also been attempted to evaluate the interfacial region, including examination of individual nanotube fragmentation under composite loading (Wagner et al., 1998). Again, due to the extremely small size of the

interfacial region, all these attempts are either too difficult or too expensive, or the results are unreliable due to the associated errors in measurements.

One of the most powerful tools for evaluating the interfacial region of polymer nanocomposites is the use of modeling and simulation techniques. However, there are some serious issues with the simulation of polymer nanocomposites that have hindered exploitation of modeling for prediction of structure-property relationships. Polymer structures range from the Ångström level of individual backbone bonds of a single chain to the scale of the radius of gyration (Gedde, 1999), which can reach tens of nanometers (Glotzer & Paul, 2002). The corresponding time scales of the dynamic processes relevant for material properties span an even wider range: from femtoseconds (10^{-15} s) to milliseconds or even seconds or hours. No single model can span this wide range of length and time scales. Multi-scale modeling approaches have been proposed to bridge between the different scales (Buryachenko et al., 2005; Gates et al., 2005; Zeng et al., 2008). MD simulation provides a powerful modeling tool to investigate the phenomena taking place at the molecular level. Different interactions between the atoms comprising the material of study are taken into account and using the classic Newtonian equations of motion and conservation of energy principles to determine the dynamics of the system (Binder, 1995; Haile, 1999; Frenkel & Smit, 2002; Rapaport, 2004).

2.6.1. Nanocomposite Interface Simulations

Many molecular simulations to examine interfacial phenomena in polymer nanocomposites have been reported. The majority have employed MD and Monte Carlo (MC) methods. Primarily focused on nanoparticles and carbon nanotubes, limited reports

exist for simulation of carbon nanofibers with stacked-cup internal morphologies. Vacatello (2001; 2003) used MC and MD simulations to predict the molecular arrangement of model polymer chains around spherical nanoparticles embedded in a polymer nanocomposite. The polymer was modeled as unbranched sequences of 100 isodiametric (same diameter) units. Filler particles were introduced as different-sized spheres. The polymer chains surrounding the nanoparticles were further described as sequences of “interface segments” (chain segments located totally within the interface shell of a given particle), “bridge segments” (sequences of non-interface units with the two adjoining units in the interface shells of two different particles), and “loop segments” (similar to bridge segments, but starting and ending in the interface shell of the same particle). The MC cycle consisted of 10^6 attempted “reptation” moves (de Gennes, 1971) per chain. The average number of different chain segment types was then calculated as a function of particle diameter and rules were proposed for predicting the arrangement of polymer chains in the vicinity of nanoparticles.

Smith et al. (2003) used MD simulations for a nanocomposite consisting of spherical nanoparticles in a bead-spring polymer melt. A coarse-grained methodology and the Lucretius simulation package (Lucretius, 2011) were used to calculate the mean force potential as a function of nanoparticle separation. The second virial coefficient for the nanoparticle was further calculated and used as an indicator for the tendency of particles to aggregate or disperse within a solution. Results for different molecular weights of the polymer showed that matrix-induced interactions (Bedrov et al., 2003) had a greater range than did the direct nanoparticle-nanoparticle interactions. When the polymer-nanoparticle interactions were relatively weak, the polymer matrix promoted

nanoparticle aggregation, an effect that increased with polymer molecular weight. Increasingly attractive nanoparticle-polymer interactions led to strong polymer chain adsorption on the nanoparticle surfaces and promoted nanoparticle dispersion.

Kairn et al. (2005) used MD simulations to study the rheology of model polymer melts containing various concentrations of spherical filler particles. The MD results were compared with the experimental results for calcium-carbonate-filled PP. Steady-state shear viscosity trends of the simulated polymer-filler system were in agreement with the experimental results; shear viscosities, zero-shear viscosities, and the rate of shear thinning all increased with filler content in both the experimental and simulated systems.

Gersappe (2002) used MD simulations for a model linear polymer chain and filler particles at temperatures above and below the T_g of the polymer to understand the molecular mechanisms of failure in polymer nanocomposites. The force-distance correlation was determined. The ability of the nanofiller to increase the material toughness resulted from the equivalence of the time scales of motion for the polymer and the filler. The mobility of the nanofiller rather than its surface area was found to be the key to the nanocomposite's performance and this mobility was a complex function of the filler's size, the polymer/filler attraction, and the thermodynamic state of the matrix.

Cho et al. (2007) investigated the effect of inclusion size on polymer nanocomposites using MD simulations. The LAMMPS simulation package (LAMMPS, 2011) was used with a coarse-grained bead spring model for the polymer. Simulated tensile tests were performed on the simulation box containing polymer chains and filler particles. The Young's modulus was calculated for each simulated nanocomposite through stress-strain analysis. It was strongly affected by the nanoparticle size as well as

by the interaction strength between polymer chains and nanoparticles. The nanocomposite's Young's modulus was enhanced as the size of the nanoparticles was reduced, as long as the strength of the polymer-nanoparticle interaction was stronger than or equal to that of the polymer-polymer interaction.

Adnan et al. (2007) used similar MD simulations to study the size effect of fullerene bucky-balls in a polyethylene (PE) matrix. A series of unidirectional hydrostatic tests, both in tension and compression, were simulated, showing that the nanocomposite elastic properties are significantly enhanced with a reduction in bucky-ball size. The densification of the polymer matrix near the nanoparticle as well as the filler-matrix interaction energy were claimed to play major roles in the size effect.

Sikdar et al. (2006) studied the interfacial interactions between different components of intercalated organically modified montmorillonite (OMMT) and polymer clay nanocomposites using MD simulations. NAMD V2.5 MD software (NAMD, 2011) was used to conduct the simulations and to calculate the interaction energies. One interesting aspect of these simulations is that hydrogen bond energy was included in addition to van der Waals energy for the non-bonded interactions.

Sikdar et al. (2008) investigated the interfacial interactions between polymers, clays, and different organic modifiers using MD simulations. The interfacial interactions were found to have an effect on the crystallinity and nanomechanical properties of the nanocomposites.

Putz et al. (2007) used DMA to study the role of interfacial interactions in functionalized SWCNT/PS nanocomposites. The results were compared to the predictions of the Halpin-Tsai model for different concentrations of nanotubes. The

dynamic mechanical properties of these composites were shown to be very sensitive to PS-nanotube interfacial interactions and to the dispersion of nanotubes and to the size of SWCNT aggregates throughout the PS host, i.e., morphology.

Han et al. (2007) calculated elastic properties for SWCNT-reinforced PMMA and poly{(m-phenylene-vinylene)-co-((2,5-dioctoxy-p-phenylene) vinylene)} (PmPV) using MD simulations. The elastic moduli for these systems were calculated based on the concept that the stress in a solid is defined as the change in the internal energy per unit volume with respect to the strain. Upon comparison with experimental results, it was found that the general macroscopic rule-of-mixtures could not be applied directly to composites with strong interfacial interactions between nanotubes and polymer matrix.

Liao et al. (2001) studied the interfacial characteristics of a CNT/PS nanocomposite using MD simulations and elasticity calculations. A mismatch in the coefficient of thermal expansion between nanotube and polymer was reported to result in residual thermal radial stress and deformation along the tube when the polymer was cooled from its melt. This significant factor was found to contribute to the mechanical interlocking mechanism. The nanotube pullout energy was further calculated and the interfacial shear stress (ISS) was determined. It was concluded that the fiber/matrix adhesion comes from 1) electrostatic and van der Waal's interactions, 2) a mismatch in the coefficient of thermal expansion, and 3) the radial deformation induced by atomic interactions.

Frankland et al. (2002) investigated the influence of chemical crosslinks on the shear strength of CNT-polymer interfaces. Crystalline and amorphous PE matrices were used as model polymers. Using periodic boundary conditions, 880 carbon atoms in the

nanotube, 178 chains, and 42 methylene units for PE, the system was equilibrated to 300 K and then six crosslink chains containing two methylene units, each between nanotube and polymer, were introduced. Using the DL_POLY simulation package (DL_POLY, 2011), the ISS was calculated. Both shear strength and critical load transfer length were shown to be enhanced and decreased by over an order of magnitude, respectively, with the formation of crosslinks involving less than 1% of the nanotube carbon atoms. Frankland et al. (2003) used other MD simulations (using DL_POLY simulation package) to numerically determine the stress-strain behavior of a nanocomposite made of SWCNTs embedded in a PE matrix. A comparison was made between the composite response to mechanical loading with long continuous nanotubes and short discontinuous nanotubes. The MD simulation predictions were further compared with the corresponding rule-of-mixture predictions. The long-nanotube composite showed an increase in the stiffness relative to the polymer and behaved anisotropically under different loading conditions, while the short-nanotube composite showed no enhancement relative to the polymer.

Frankland et al. (2007) used yet other MD simulations to determine the local elastic constants of an epoxy/nanotube composite as a function of radial distance from the nanotube. A representative volume element (RVE) containing about 28,000 atoms of cured epoxy and 880 carbon atoms in the nanotube was used. The simulations were carried out using the DL_POLY software (DL_POLY, 2011) with the AMBER force field under an NVE (constant number of atoms, N ; constant volume, V ; constant energy, E) ensemble.

In a similar work to Frankland et al. (2007), Mokashi et al. (2007) studied the tensile response and fracture in carbon nanotube-based composites using molecular mechanics (similar to MD). The system comprised of SWCNTs in a crystalline/amorphous PE matrix. Using the DL_POLY software package (DL_POLY, 2011), they determined the elastic moduli and tensile strengths for the different nanocomposites and compared the results to those reported in the literature.

Chowdhury et al. (2007) simulated the CNT pullout from a crystalline PE matrix using MD simulations. The influences of the polymer matrix density, chemical crosslinks in the interface, and pentagon-heptagon geometrical defects in the CNTs on the ISS were examined. Using the Brenner potential for carbon-carbon interactions and the AMBER potential with some modifications for united atom model for polymer chains, it was found that 1) an increase in the matrix density resulted in an increased ISS, 2) the presence of chemical crosslinks in the interface increased the ISS, 3) the crosslink positions affected the ISS, and 4) the pentagon-heptagon geometrical defects had little effect on the ISS when there were no crosslinks in the interface; however, it significantly reduced the ISS when crosslinks were present in the interface.

Coleman et al. (2006) introduced the idea of an ordered polymer interfacial region in polymer nanocomposites. The Young's modulus was measured and calorimetry measurements were carried out for CNT-reinforced polyvinyl alcohol (PVA) at different nanotube volume fractions. A correlation was found between polymer ordering and reinforcement. Furthermore, a model was developed capable of establishing quantitatively how the ordered phase affects the increase in the Young's modulus.

Gou et al. (2004) studied the interfacial bonding of SWCNT-reinforced epoxy resin. MD simulations were combined with experiments and nanotube pullout simulations were conducted to calculate the ISS. A 3D crosslinked (cured) epoxy resin was used as the model for polymer matrix. The pullout results showed that the ISS between nanotubes and epoxy network could be as high as 75 MPa.

In another similar study, Gou et al. (2005) used MD simulations to investigate the effect of SWCNT ropes (bundles) on molecular interactions and load transfer in cured epoxy resin. Based on the results of nanotube bundle pullout simulations, it was concluded that the molecular interactions and load transfer were dependent on not only the physical interactions between the nanotubes and the epoxy resin, but also on the internal interactions within the nanotube rope system. Individual nanotubes were argued to have stronger interactions with the epoxy resin and, therefore, provided better load transfer than the nanotube rope.

2.6.2. MD Simulations of VGCNF/VE Nanocomposites

The only systematic study, to date, of the interfacial interactions between pristine and functionalized VGCNFs and a polymer resin using MD simulations was reported by Gou et al. (2007). Accelrys® Materials Studio® software (Accelrys, 2011) and its COMPASS force field (Sun, 1998) were used to perform the simulations at an initial temperature of 300 K using NVT (constant number of atoms, N; constant volume, V; constant temperature, T) ensemble. EPON 862 and DGEBA epoxy resin systems in their uncured oligomeric form were used. The functionalized nanofiber was modeled, based on XPS analysis results, by introducing some functional groups on the nanofiber surface in a

random fashion. The nature of these functionalized groups was not discussed. An increased tendency for the aromatic ring of the epoxy molecule to align on the surface of the pristine VGCNF was found compared to functionalized VGCNFs. It is noteworthy to mention that interactions for only one single epoxy chain in the vicinity of the nanofiber surface were simulated. This was a major drawback of the work as the real environment for the interfacial region was not well represented. Therefore, no interactions between epoxy chains and other associated effects were taken into account.

CHAPTER 3
DYNAMIC MECHANICAL ANALYSIS OF VAPOR-GROWN CARBON
NANOFIBER/VINYL ESTER NANOCOMPOSITES USING DESIGN OF
EXPERIMENTS PART 1: ANALYSIS AT ROOM TEMPERATURE

In automotive applications, polymer nanocomposites with improved mechanical properties and energy absorption characteristics are desired. While automotive applications for nanocomposites have been proposed (Prestin & König, 2003), commercialization has not been fully realized due to the fabrication issues discussed in section 2.3.1. The current study investigates, for the first time, the combined effect of various formulation and processing factors on the dynamic mechanical properties of VGCNF/VE nanocomposites in the framework of a robust experimental design (Montgomery, 2009; Cox & Reid, 2000). The objective is to provide a statistically reliable and reproducible way to fabricate these materials with a focus on the prediction and optimization of their mechanical performance through response surface modeling (Myers et al., 2009). These predictive models will enable composite manufacturers to tailor nanocomposites for different applications through the manipulation of state-of-the-art design factors. The design factors considered here were 1) the use of oxidized versus pristine nanofibers, 2) the use of dispersing agent versus none, 3) the mixing method (ultrasonication, high-shear mixing, and a combination of both), and 4) the nanofiber

weight fraction. These factors reflect various means to fabricate nanocomposites with well-dispersed nanoreinforcements and good nanoreinforcement-matrix interfacial adhesion as discussed in sections 2.1.2 and 2.3.1. Viscoelastic properties (storage and loss moduli) were selected as the mechanical responses since these are measures of stiffness and energy dissipation, both of interest for automotive applications. Statistical analysis was used to construct response surface predictive models and to determine the optimal nanocomposite formulation and mixing method leading to optimal viscoelastic properties.

3.1. Materials and Methods

3.1.1. Statistical Design of Experiments

A general mixed-level full factorial experimental design was used with four formulation and processing factors: a) VGCNF type (pristine, surface oxidized), b) use of dispersing agent (no, yes), c) mixing method (ultrasonication, high-shear mixing, and a combination of both), and d) VGCNF weight fraction. Experimental design factors and their levels are shown in Table 3.1.

Table 3.1 Design factors and their levels.

Factor Designation	Factor	Levels				
		1	2	3	4	5
A	VGCNF ¹ type	Pristine	Oxidized	-	-	-
B	Use of dispersing agent	No	Yes	-	-	-
C	Mixing method	US ²	HS ³	HS/US		
D	VGCNF weight fraction (phr ⁴)	0	0.25	0.50	0.75	1.00

¹ Vapor-grown carbon nanofiber

² Ultrasonication

³ High-shear mixing

⁴ Parts per hundred parts resin

The treatment combinations (see section 2.5.2) were randomized to eliminate bias in preparing the specimens. The type of VGCNF (designated as A), use of dispersing agent (B), and mixing method (C) were qualitative (discrete) in nature, whereas the VGCNF weight fraction (D) was quantitative (continuous). One VGCNF/VE liquid batch was prepared corresponding to each treatment combination. From each batch, three test specimens were molded. Storage and loss moduli were selected as the mechanical responses of interest.

3.1.2. Materials

A low styrene content (33 wt %) vinyl ester resin (Ashland Co., Derakane 441-400) was used in this study. This resin has an average molecular weight of 690 g/mol (Li, 1998) and the matrix resulting from it has superior thermal properties and corrosion resistance performance (see appendix A for datasheet). Two VGCNF commercial grades were used. The first, PR-24-XT-LHT (Applied Sciences Inc.), has been heat-treated at

1500 °C and has an average diameter of 150 nm, a surface area of 35-45 m²/g, and a dispersive surface energy of 155 mJ/m² (see appendix A for datasheet). The second, PR-24-XT-LHT-OX (Applied Sciences Inc.), is a surface-oxidized version of PR-24-XT-LHT. Surface oxidation creates hydroxyl, carbonyl, and carboxylic acid surface functions (Klein et al., 2008). These functions increase fiber-to-matrix interfacial adhesion (Fu et al., 2009). MEKP (U.S. Composites Inc.) and 6% CoNap solution (North American Composites Co.) were used as the hardener and promoter, respectively. The promoter accelerates peroxide decomposition during curing (see section 2.2.2). Air release additives (BYK Chemie GmbH, BYK-A 515 and BYK-A 555), were used to remove air bubbles introduced during mixing (see appendix A for datasheets). Air voids may degrade the cured nanocomposite properties. VGCNFs raise the pre-cured resin's viscosity, aggravating air bubble entrapment/void formation.

A commercial dispersing agent (BYK-Chemie GmbH, BYK-9076) was used to improve VGCNF dispersion in the resin (see appendix A for datasheet). This proprietary surface-active agent is a copolymer alkylammonium salt used to wet and disperse carbon blacks and carbon nanotubes in polyesters, VE, and epoxy nanocomposites (Liao et al., 2004; Xia & Song, 2005; Zhang et al., 2007). Table 3.2 shows the nanocomposite formulations used in this study. All prepared nanocomposites contained a fixed amount of resin, promoter, air release additives, and hardener.

Table 3.2 Nanocomposite formulations used in this study.

Ingredient	Weight (g)
Derakane 441-400 (vinyl ester resin)	100
Cobalt naphthenate 6% (promoter)	0.20
BYK-A 515 (air release agent)	0.20
BYK-A 555 (air release agent)	0.20
BYK-9076 (dispersing agent)	1:1 ratio with respect to VGCNF ¹
VGCNF ² (vapor-grown carbon nanofiber)	0.00/0.25/0.50/0.75/1.00
MEKP (hardener)	1.00

¹The amount of dispersing agent was varied in direct proportion to the weight fraction (and surface area) of VGCNF.

²Pristine or oxidized

3.1.3. Specimen Preparation

Test specimens were prepared using this protocol:

- 1) All ingredients except the hardener (Table 3.2) were added to a cup (a batch based on 75 g resin) in the following order: a) resin, b) promoter, c) air release additives, d) dispersing agent (when employed in the treatment combination), and e) VGCNF. The blend was thoroughly hand-mixed before nanofiber addition to insure proper mixing of the promoter, air release additives, and dispersing agent. The latter must be added before adding VGCNF.
- 2) Three nanofiber mixing procedures were used: a) ultrasonication, b) high-shear mixing, and c) coupled high-shear mixing/ultrasonication. Ultrasonication involved initial mechanical stirring (Cole-Parmer Instrument Co., Stir-Pak mixer) for 5 min at 1500 rpm followed by one hour of sonication (Geneq Inc., ultrasonic processor GEX750-5C) at a 20% amplitude (150 W) in the continuous (no pulse) mode. The batch (~70 ml) was continuously shaken using a 120 V vortex mixer (Fisher Scientific) during sonication providing a uniform ultrasonic power input,

while being continuously air-cooled using a high-speed fan. High-shear mixing employed a laboratory scale high-shear mixer (Silverson Machines Ltd., model L4RT-A) for 10 min at 3000 rpm and 5 min at 4000 rpm. The cup was cooled in an ice bath during mixing to prevent heating. Coupled high-shear mixing/ultrasonication employed high-shear mixing first followed by ultrasonication (both as described above) without mechanical stirring. The neat resin was only hand-blended. Figure 3.1 shows a schematic of how the high-shear mixer disperses the nanofibers in the resin.

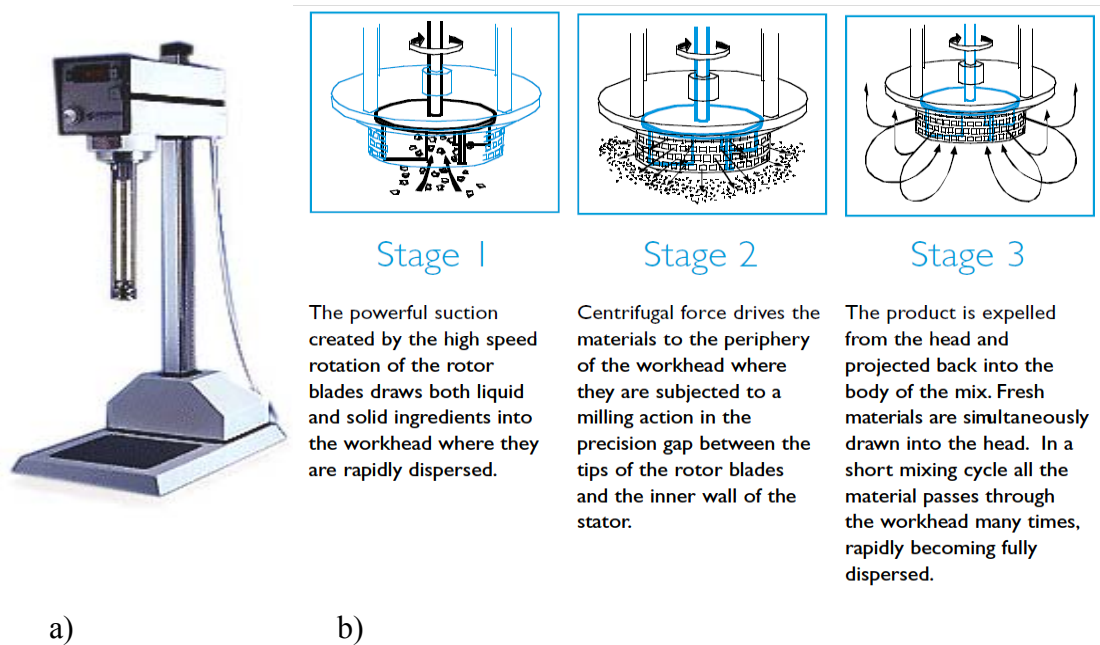


Figure 3.1 a) Silverson high-shear mixer model L4RT-A. b) A description of solid dispersion mechanism in three stages (courtesy of Silverson Machines, Ltd.).

- 3) The hardener was hand-blended for 5 min into the VGCNF/VE batch to avoid curing during preparation.

- 4) The liquid blend was degassed under vacuum for 5-15 min (depending on the blend's viscosity) at pressures of 8-10 kPa to remove air bubbles trapped during mixing.
- 5) The VGCNF/VE blend was poured in a chrome-plated mold (TMI Co.) and oven-cured for 5 h at 60 °C followed by 2 h post-curing at 120 °C. In thermosets like vinyl esters, different curing schedules generate different ultimate mechanical properties (Li, 1998).

3.1.4. Dynamic Mechanical Analysis

Nanocomposite DMA test specimens ($35 \times 12.5 \times 3.5 \text{ mm}^3$) were cut from cured specimens and polished on both sides using sandpaper to remove any defects from the surfaces. The storage and loss moduli were measured using a dynamic mechanical analyzer (TA Instruments, Model Q800) in single cantilever mode with amplitude of 15 μm , fixed frequency of 10 Hz, heating rate of 5 °C /min., over a 27 °C to 160 °C temperature range. Only the values at 27 °C (room temperature) were used in the statistical analysis. The storage and loss modulus measurements were obtained for the three specimens corresponding to each treatment combination. The average value was calculated for each response and used in the experimental design.

3.2. Results and Discussion

The average storage and loss modulus for each treatment combination (run) are shown in Table 3.3. Since three separate specimens were tested for each treatment combination, standard deviations were calculated for each run. These measures of

variation in the storage and loss modulus data gave the sampling error (see section 2.5.2), which was of no interest to the objectives of the design, and therefore, only the average standard deviations are reported here. The average standard deviation for the storage modulus data was 75 MPa and for the loss modulus data was 5 MPa. These averages were calculated based on the individual standard deviations for all treatment combinations. Treatment combinations having 0.0 phr VGCNF correspond to the unmodified neat VE resin prepared by simple hand-mixing. These all have the same storage and loss modulus values regardless of the other factor levels. They are all included in Table 3.3 to show the full factorial data set and avoid the confusion of a missing data situation. The statistical design incorporated a total of 60 ($2 \times 2 \times 3 \times 5$) treatment combinations. The numbers in the parenthesis correspond to the number of levels for each factor multiplied together to give full factorial combinations.

Table 3.3 Randomized design treatment combinations and measured average responses¹.

Run	A: VGCNF Type	B: Use of Dispersing Agent	C: Mixing Method	D: VGCNF Weight Fraction (phr)	Response 1: Storage Modulus (MPa)	Response 2: Loss Modulus (MPa)
1	Oxidized	Yes	US	0.50	2591	59
2	Pristine	No	HS/US ²	1.00	2686	43
3	Pristine	Yes	HS	1.00	2676	51
4	Pristine	No	US	0.25	2728	65
5	Oxidized	Yes	HS	0.25	2578	48
6	Pristine	Yes	US	0.50	2515	100
7	Pristine	No	US	0.50	2660	49.5
8	Pristine	No	HS/US	0.75	2566	45
9	Pristine	No	HS	0.75	2488	50
10	Pristine	Yes	HS/US	0.75	2573	42
11	Oxidized	Yes	HS	0.75	2682	47
12	Oxidized	No	HS/US	0.50	2706	45
13	Pristine	Yes	HS	0.75	2713	50
14	Oxidized	No	HS/US	1.00	2559	43
15	Pristine	No	HS	1.00	2691	50
16	Oxidized	Yes	US	0.25	2579	72
17	Pristine	No	US	1.00	2449	43
18	Oxidized	No	US	0.75	2616	55
19	Oxidized	No	US	0.25	2500	70
20	Pristine	No	HS	0.50	2527	43
21	Oxidized	No	US	0.50	2652	59
22	Pristine	No	HS	0.25	2674	48
23	Pristine	No	US	0.75	2407	43
24	Pristine	No	HS	0.00	2186	58
25	Pristine	Yes	HS	0.25	2551	51
26	Oxidized	Yes	HS	0.50	2648	59
27	Pristine	Yes	HS/US	1.00	2609	44
28	Oxidized	No	HS	0.50	2632	44

Table 3.3 continued on the next page

Table 3.3 continued

Run	A: VGCNF Type	B: Use of Dispersing Agent	C: Mixing Method	D: VGCNF Weight Fraction (phr)	Response 1: Storage Modulus (MPa)	Response 2: Loss Modulus (MPa)
29	Oxidized	No	HS	0.00	2186	58
30	Oxidized	No	HS/US	0.75	2691	43
31	Oxidized	Yes	HS/US	0.50	2517	44
32	Oxidized	No	HS/US	0.00	2186	58
33	Oxidized	No	HS	0.25	2582	45
34	Pristine	Yes	HS	0.50	2746	49
35	Oxidized	No	HS	0.75	2604	46
36	Pristine	Yes	HS/US	0.50	2768	48
37	Pristine	Yes	HS/US	0.00	2186	58
38	Oxidized	Yes	HS/US	0.75	2599	47
39	Oxidized	Yes	US	1.00	2566	69
40	Oxidized	No	HS	1.00	2673	45
41	Oxidized	Yes	HS/US	0.00	2186	58
42	Pristine	Yes	HS/US	0.25	2661	45
43	Oxidized	Yes	HS	0.00	2186	58
44	Oxidized	Yes	US	0.00	2186	58
45	Oxidized	Yes	HS/US	1.00	2728	45
46	Pristine	No	HS/US	0.00	2186	58
47	Pristine	No	HS/US	0.25	2563	45
48	Pristine	No	HS/US	0.50	2603	43
49	Oxidized	No	US	0.00	2186	58
50	Pristine	Yes	HS	0.00	2186	58
51	Oxidized	Yes	US	0.75	2650	68
52	Pristine	No	US	0.00	2186	58
53	Pristine	Yes	US	1.00	2652	64
54	Pristine	Yes	US	0.75	2481	53
55	Oxidized	Yes	HS	1.00	2643	49
56	Oxidized	No	HS/US	0.25	2575	41
57	Pristine	Yes	US	0.00	2186	58
58	Oxidized	Yes	HS/US	0.25	2532	42
59	Oxidized	No	US	1.00	2587	52
60	Pristine	Yes	US	0.25	2598	76

¹ The average value of three independent samples was used to obtain the responses. The average standard deviation for the storage modulus data was 75 MPa and for the loss modulus data was 5 MPa.

² US = ultrasonication, HS = high-shear mixing

3.2.1. Statistical Analysis of the Storage Modulus Data

The measured storage moduli were analyzed using SAS 9.2 statistical analysis software (SAS, 2011). The SAS program code is given in Appendix B. Since each treatment combination was replicated once (see section 2.5.2), there was no experimental error in the analysis. Therefore, it was assumed that three-factor and four-factor interactions are negligible to construct an error term. An analysis of variance (ANOVA) was performed on storage modulus data to assess the importance of the main and two-factor interaction effects (see section 2.5.2). The ANOVA results are shown in Table 3.4. Hierarchical (ordered) F -tests (Ellison et al., 2009), or equivalently a test of p -values determined from the F statistics, were conducted on the factorial effects starting from the highest order (two-factor) interactions. In the table, factorial effects with p -values less than a significance level (α) of 0.10 (10%) are considered significant. Since the ANOVA results are used as a screening mechanism for this study to help and guide in the model development, the choice of α has largely been at our discretion in order to render one of the interactions significant and analyze it in more detail.

In Table 3.4, the interaction between VGCNF type (A) and weight fraction (D) significantly affects the mean storage modulus (p -value = 0.0989 < α), while other factorial effects are not significant. The VGCNF weight fraction (D) with a p -value less than 0.10 is involved in the higher order interaction with VGCNF type (A). Because of the significance of A×D interaction, separate regression equations were developed for nanocomposites with pristine and oxidized VGCNFs.

Table 3.4 Analysis of variance (ANOVA) for the storage modulus data.

Source of Variation	Degrees of Freedom	Sum of Squares	Mean Square	F-value	p-value ¹
Model	29	1862151.783	64212.130	11.75	<0.0001
A: VGCNF Type	1	183.750	183.750	0.03	0.8557
B: Use of Dispersing Agent	1	3182.817	3182.817	0.58	0.4513
C: Mixing Method	2	21595.633	10797.817	1.98	0.1563
D: VGCNF Weight fraction	4	1741811.767	435452.942	79.69	<0.0001 ²
A×B	1	5320.417	5320.417	0.97	0.3317
A×C	2	3739.300	1869.650	0.34	0.7130
<u>A×D</u>	<u>4</u>	<u>47017.500</u>	<u>11754.375</u>	<u>2.15</u>	<u>0.0989</u>
B×C	2	3641.633	1820.817	0.33	0.7192
B×D	4	11306.433	2826.608	0.52	0.7236
C×D	8	24352.533	3044.067	0.56	0.8039
Error	30	163936.400	5464.547	-	-
Total (Corrected)	59	2026088.183	-	-	-
Other Model Statistics					
Mean: 2525.117			R ² : 0.919		
Coefficient of variation: 2.93%			Standard deviation: 73.92		

¹ Values <0.10 are considered significant in the analysis.

² Factor is involved in interaction.

Note: The underlined two-factor interaction (VGCNF Type×VGCNF weight fraction) is significant.

Different polynomial fits were considered to the data points (linear, quadratic, cubic, etc.). A cubic response surface model was ultimately developed for each VGCNF type to characterize the nanocomposite storage modulus as a function of VGCNF weight fraction because both models had relatively high R²/adjusted R² values (Table 3.5). The R² value indicates the amount of variation explained by a model.

The general cubic response surface model for the storage modulus can be written as:

$$S_i = \beta_0 + \beta_1 D_i + \beta_2 D_i^2 + \beta_3 D_i^3 + e_i \quad (3.1)$$

where S_i is the storage modulus, β_0 is the intercept, β_i 's are model parameters, D_i represents the VGCNF weight fraction (phr), and e_i is the error term. In Table 3.5, the model parameters, their estimates, t - and p -values (Ott & Longnecker, 2010) are shown. Parameters with p -values of less than α (typically 0.05) are considered significant model terms.

Table 3.5 Regression analyses for the storage modulus data.

Parameter	Degrees of Freedom	Parameter Estimate	Standard Error	t -value	p -value
Pristine VGCNF:					
β_0	1	2186.52143	33.74629	64.79	<0.0001
β_1	1	3033.92857	343.38845	8.84	<0.0001
β_2	1	-5918.09524	872.08273	-6.79	<0.0001
β_3	1	3325.33333	573.25678	5.80	<0.0001
R ² : 0.8320		Adjusted R ² : 0.8126			
Max storage modulus=2667 MPa at $D_i=0.37$ phr					
Oxidized VGCNF:					
β_0	1	2189.34286	19.73748	110.92	<0.0001
β_1	1	2112.63492	200.84052	10.52	<0.0001
β_2	1	-3137.52381	510.06242	-6.15	<0.0001
β_3	1	1464.88889	335.28556	4.37	0.0002
R ² : 0.9353		Adjusted R ² : 0.9278			
Max storage modulus=2646 MPa at $D_i=0.54$ phr					

The final response surface models for predicting storage modulus (S) as a function of VGCNF weight fraction (D) are expressed as:

$$S_{Pristine} = 2186.521 + 3033.929D - 5918.095D^2 + 3325.333D^3 \quad (3.2)$$

$$S_{Oxidized} = 2189.343 + 2112.635D - 3137.524D^2 + 1464.889D^3 \quad (3.3)$$

Based on the R^2 values (Table 3.5), the fitted cubic response surface models for $S_{Pristine}$ and $S_{Oxidized}$ explain 83% and 94% of the storage modulus variation, respectively. Response surface models for the storage modulus are plotted in Figure 3.2. Included in the figure, are the actual mean values of the experimental measurements at each weight fraction and their corresponding average standard deviations. Each mean data point corresponds to six actual data points that have been grouped together because of their insignificant differences. Both response surface models approximate the observed mean response over the range of nanofiber weight fractions and asymptotically approach the neat VE property as the weight fraction of VGCNF approaches 0.0 phr. In general, the predicted storage modulus obtained with each model increased with increasing VGCNF weight fractions up to a local maximum; a further increase in the weight fraction of VGCNF did not result in additional improvement in the predicted storage modulus.

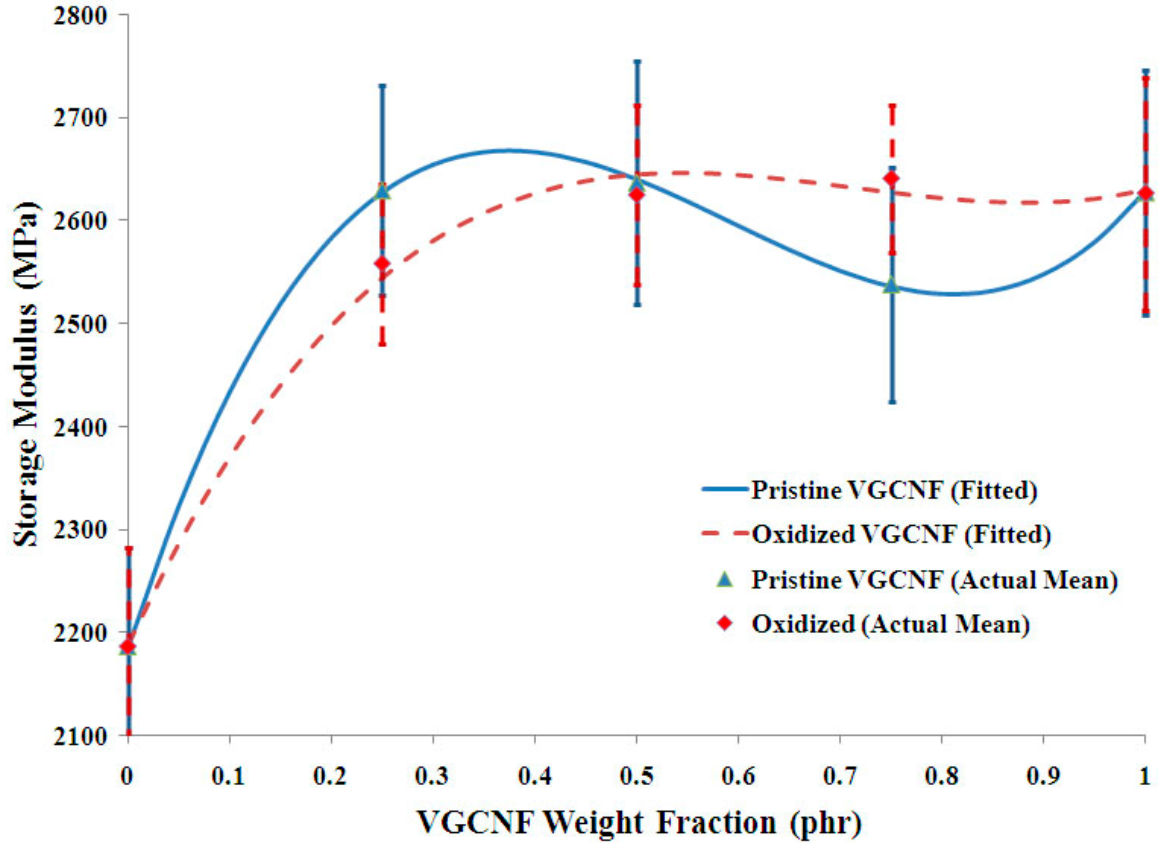


Figure 3.2 Predicted storage modulus versus actual mean data for different VGCNF types as a function of VGCNF weight fraction.

Nanocomposites containing pristine VGCNFs yielded a higher maximum predicted storage modulus (2667 MPa) at 0.37 phr VGCNF, while oxidized VGCNF nanocomposites resulted in a peak predicted storage modulus (2646 MPa) at 0.54 phr VGCNF. At higher VGCNF weight fractions (>0.50 phr), pristine VGCNF nanocomposites show a significant storage modulus drop due either to the presence of nanofiber agglomerates or to poor dispersion in the matrix. At still higher weight fractions, the storage modulus increases slightly. As the nanofiber weight fraction increases beyond some optimal value, the deteriorating effect of a greater number of

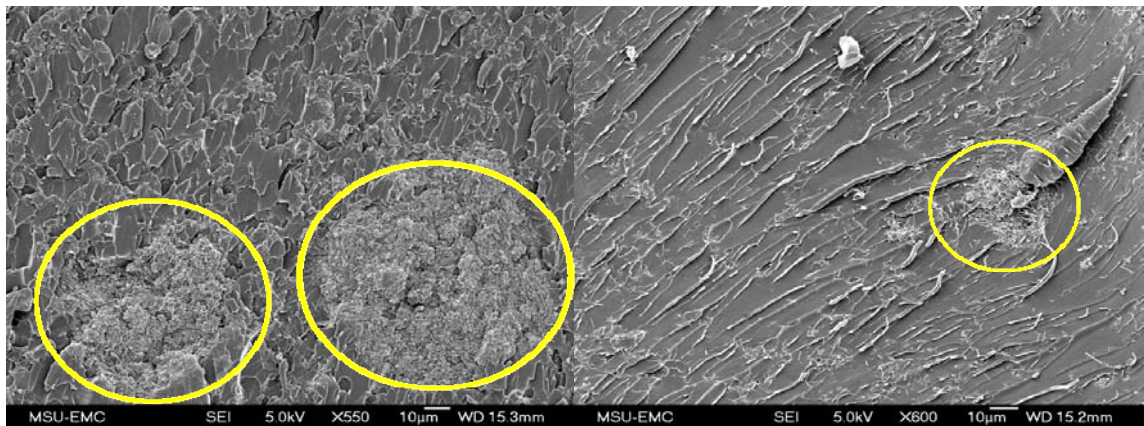
larger agglomerates on mechanical properties becomes more noticeable. Pristine nanofibers agglomerate more than oxidized nanofibers due to larger van der Waals surface interactions; the oxidized nanofiber surface energy is lower due to the presence of functional groups capable of interacting with matrix molecules. Oxidized VGCNF nanocomposites show a smoother predicted storage modulus plateau at higher VGCNF weight fractions due to their smaller content of agglomerates, but they exhibit less improvement in the storage modulus. Reducing the number and size of VGCNF agglomerates, and enhancing nanofiber dispersion remain key challenges in maximizing nanocomposite properties, particularly at higher nanofiber weight fractions, where the uncured resin/nanofiber blend viscosity significantly increases. Nanofiber agglomerations decrease the storage modulus (stiffness) due to lowered matrix-nanofiber interfacial contact and can lead to premature failure (fracture) due to local stress concentration. Overall, the inclusion of relatively small weight fractions of nanofibers (<0.50 parts per hundred parts resin) led to roughly a 20% increase in the predicted storage modulus in comparison to that of the neat cured resin.

The ANOVA results showed that the mixing method (ultrasonication, high-shear, or coupled mixing) did not significantly affect the mean storage modulus. This suggests that high-shear mixing may be used to fabricate nanocomposites without degradation in the storage modulus. High-shear mixing is less expensive and labor-intensive than ultrasonication, and may be used to produce commercial resin/nanofiber blend volumes.

The use of a dispersing agent did not significantly affect the predicted storage modulus, but it did dramatically reduce the viscosity of the resin/nanofiber blend. Maintaining low blend viscosity is important for commercialization of nanocomposites

and for infusing VGCNF/VE blends into continuous woven fibers. High aspect ratio VGCNFs agglomerate due to a combination of mechanical interlocking and fiber-to-fiber surface interactions. Use of a dispersing agent coupled with aggressive mixing may significantly disentangle nanofibers and inhibit their re-agglomeration.

Figure 3.3 shows typical scanning electron micrographs of the fracture surface from two 1.00 phr nanocomposites prepared using ultrasonication. Figure 3.3a and 3.3b contain ~600X magnification images of specimens prepared with and without a dispersing agent, respectively. Both the number density and size of VGCNF agglomerates are reduced for specimens prepared using a dispersing agent. However, this reduction is not yet sufficient at current levels of mixing to have a significant effect on the storage modulus.



a)

b)

Figure 3.3 Scanning electron micrographs of the fracture surfaces of two VGCNF/VE nanocomposites: a) 1.0 phr pristine nanofibers without dispersing agent mixed with ultrasonication, where two large-size VGCNF agglomerates (50-75 μm) can be seen. b) 1.0 phr pristine nanofibers with dispersing agent mixed with ultrasonication, where a smaller agglomerate is observed (25 μm).

3.2.2. Statistical Analysis of the Loss Modulus Data

Similar to the storage modulus, three and four-factor interactions were considered negligible to construct an error term for the loss modulus data. Therefore, analysis of variance was conducted on the loss modulus data to study the main and two-factor interaction effects (see the SAS program code in Appendix B). The ANOVA results are shown in Table 3.6. Hierarchical *F*-tests starting from two-factor interactions resulted in two significant interactions at 10% level of significance ($\alpha = 0.10$): a) mixing method/VGCNF weight fraction interaction (C×D), and b) use of dispersing agent/mixing method interaction (B×C). Factors B (use of dispersing agent), C (mixing method), and D (VGCNF weight fraction) are involved in higher order interactions. Furthermore, VGCNF type was not significant.

Since C×D interaction is significant, separate regression equations need to be fit to the data associated with the three mixing methods. Furthermore, a significant B×C interaction indicates that the data associated with each mixing method may further be separated into those with dispersing agent present in the formulation and those with dispersing agent absent (a total of six actual mean data points per each VGCNF weight fraction). To further analyze the B×C interaction, multiple comparisons between the mean data was conducted using Fisher's least significant difference (LSD) method (Myers et al., 2009). In Table 3.7, each dispersing agent/mixing method combination can be compared with the other ones. Only those with different letters (here arbitrarily chosen as X, Y, and Z) in the *t*-grouping column (grouping based on the *t*-tests) are significantly different from each other. On this basis, the use of the dispersing agent only changes the mean loss modulus for the case of ultrasonication mixing. Therefore, only the data

associated with ultrasonication are further separated into those associated with the use and non-use of the dispersing agent. The total number of mean data points per VGCNF weight fraction is, therefore, reduced to four.

Table 3.6 Analysis of variance (ANOVA) for the loss modulus data.

Source of Variation	Degrees of Freedom	Sum of Squares	Mean Square	F-value	p-value ¹
Model	29	5280.821	182.097	4.15	0.0001
A: VGCNF Type	1	0.204	0.204	0.00	0.9461
B: Use of Dispersing Agent	1	462.038	462.038	10.52	0.0029 ²
C: Mixing Method	2	2332.708	1166.354	26.55	<0.0001 ²
D: VGCNF Weight fraction	4	619.233	154.808	3.52	0.0179 ²
A×B	1	33.004	33.004	0.75	0.3929
A×C	2	10.608	5.304	0.12	0.8867
A×D	4	103.400	25.850	0.59	0.6735
<u>B×C</u>	<u>2</u>	<u>371.475</u>	<u>185.738</u>	<u>4.23</u>	<u>0.0241</u>
B×D	4	274.733	68.683	1.56	0.2095
<u>C×D</u>	<u>8</u>	<u>1073.417</u>	<u>134.177</u>	<u>3.05</u>	<u>0.0123</u>
Error	30	1317.725	43.924	-	-
Total (Corrected)	59	6598.546	-	-	-
Other Model Statistics					
Mean: 52.892			R ² : 0.800		
Coefficient of variation: 12.53%			Standard deviation: 6.63		

¹ Values <0.10 are considered significant in the analysis.

² Factors are involved in interaction.

Note: The underlined two-factor interactions are significant.

Table 3.7 Multiple comparison results using least significant differences (LSD) for the interaction between the use of dispersing agent and mixing method (B×C).

<i>t</i> -grouping	Least squares means for the loss modulus data	Use of dispersing agent (B)	Mixing method (C)
X ¹	67.70	Yes	US ²
Y	55.25	No	US
Z	52.00	Yes	HS ³
Z	48.70	No	HS
Z	47.30	Yes	HS/US
Z	46.40	No	HS/US

¹ Least squares means with the same letters are not significantly different from each other.

² Ultrasonication

³ High-shear mixing

The regression analysis for the loss modulus is shown in Table 3.8. Different polynomial fits were considered for the loss modulus data and those yielding adequate R² and adjusted R² values were selected. A cubic polynomial was fit to the loss modulus data associated with the ultrasonication and coupled high-shear mixing/ultrasonication methods. A quadratic function was fit to the high-shear mixing data. The R² and adjusted R² values for the loss modulus regression equations were not as high as the storage modulus equations due to larger data scatter.

Table 3.8 Regression analyses for the loss modulus data.

Parameter	Degrees of Freedom	Parameter Estimate	Standard Error	t-value	p-value
Ultrasonication with dispersing agent:					
β_0	1	57.09286	9.45672	6.04	0.0009
β_1	1	154.02381	96.22770	1.60	0.1606
β_2	1	-334.85714	244.38364	-1.37	0.2197
β_3	1	189.33333	160.64368	1.18	0.2832
R ² : 0.3305		Adjusted R ² : -0.0043			
Min loss modulus=57 MPa at $D_t=0$ phr					
Ultrasonication without dispersing agent:					
β_0	1	58.50000	4.10482	14.25	<0.0001
β_1	1	76.16667	41.76898	1.82	0.1180
β_2	1	-228.0000	106.07814	-2.15	0.0752
β_3	1	141.33333	69.72964	2.03	0.0890
R ² : 0.7008		Adjusted R ² : 0.5512			
Min loss modulus=45 MPa at $D_t=0.87$ phr					
High-shear mixing:					
β_0	1	56.82143	1.84690	30.77	<0.0001
β_1	1	-29.87143	8.75117	-3.41	0.0033
β_2	1	22.57143	8.39173	2.69	0.0155
R ² : 0.4830		Adjusted R ² : 0.4222			
Min loss modulus=46.94 MPa at $D_t=0.66$ phr					
Coupled high-shear mixing/ultrasonication:					
β_0	1	57.68929	1.04779	55.06	<0.0001
β_1	1	-87.29762	10.66192	-8.19	<0.0001
β_2	1	159.71429	27.07744	5.90	<0.0001
β_3	1	-86.66667	17.79914	-4.87	0.0002
R ² : 0.8940		Adjusted R ² : 0.8741			
Min loss modulus=42.77 MPa at $D_t=0.41$ phr					

Based on the model parameters in Table 3.8, the final response surface models for predicting loss modulus (L) as a function of VGCNF weight fraction (D) are expressed as:

$$L_{US-DA} = 57.093 + 154.024D - 334.857D^2 + 189.333D^3 \quad (3.4)$$

$$L_{US-No DA} = 58.500 + 76.167D - 228.000D^2 + 141.333D^3 \quad (3.5)$$

$$L_{HS} = 56.820 - 29.870D + 22.570D^2 \quad (3.6)$$

$$L_{HS/US} = 57.689 - 87.297D + 159.714D^2 - 86.667D^3 \quad (3.7)$$

where *US* in the subscript denotes ultrasonication, *HS* denotes high-shear mixing, and *DA* denotes dispersing agent. Here, 48% of the variation in high-shear mixing data and 89% of the variation in coupled mixing data are explained by the response surface models, respectively. Moreover, 70% of the variation in the ultrasonication data is explained by the model where dispersing agent is absent, while only 33% of the variation is explained by the model where dispersing agent is present (Table 3.8). Figure 3.4 contains a plot of the predicted loss modulus associated with each mixing method as a function of VGCNF weight fraction. Included in the figure are the actual mean values and their corresponding average standard deviations. The predicted loss moduli for nanocomposites prepared using high-shear and coupled mixing decrease with increasing VGCNF weight fractions. Well-dispersed VGCNFs and fewer agglomerates will reduce the resin's bulk ductility leading to lower energy dissipation and reduced loss modulus. The lowest predicted loss modulus appears for the nanocomposite prepared by coupled high-shear mixing/ultrasonication at 0.41 phr.

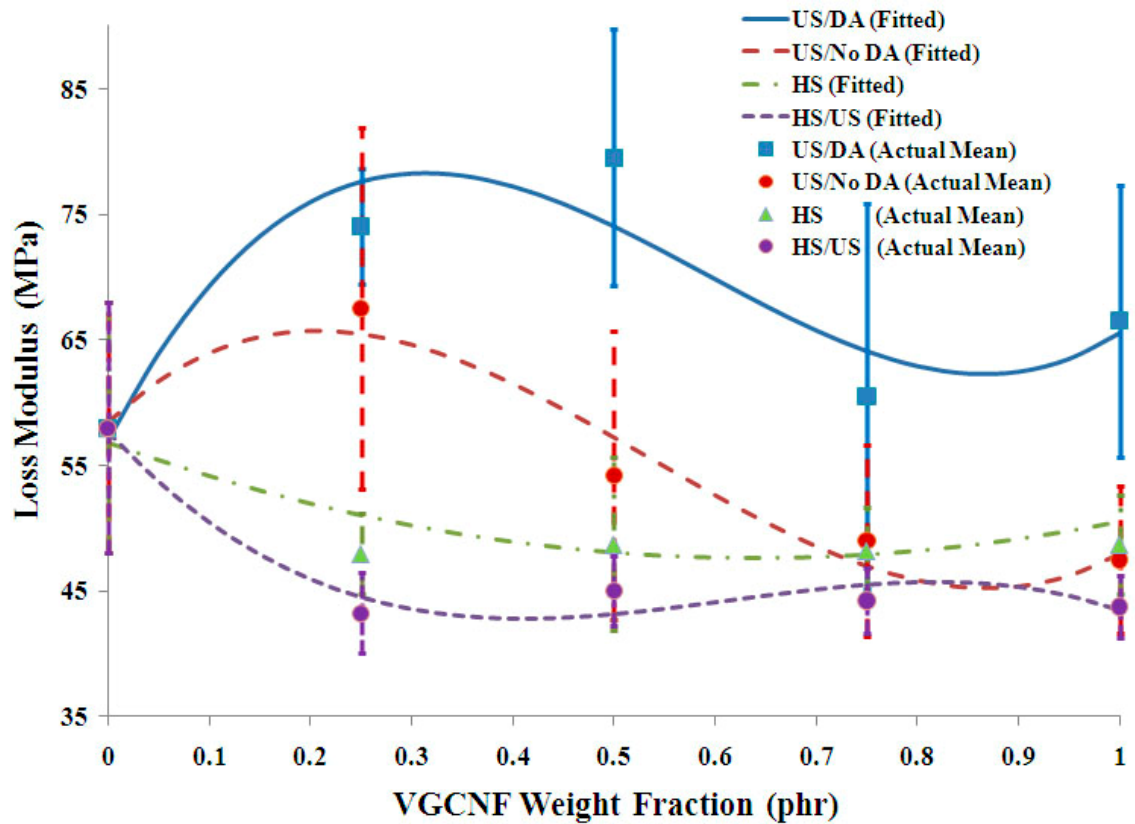


Figure 3.4 Predicted loss modulus versus actual mean data for different mixing methods as a function of VGCNF weight fraction.

In contrast to high-shear mixed samples, the predicted loss moduli were somewhat higher for nanocomposites prepared using ultrasonication with no dispersing agent (Figure 3.4). Ultrasonication is less effective than the other mixing methods in disentangling mechanically interlocked and agglomerated nanofibers. Thus, the nanocomposite energy dissipation capability may be similar to that of the neat resin, particularly at lower VGCNF weight fractions. In addition, use of a dispersing agent plasticizes the VE resin resulting in an increased loss modulus. This effect is arguably more pronounced for nanocomposites prepared by ultrasonication, where nanofiber

dispersion is relatively poor. Consistent with this observation, the highest predicted loss modulus is obtained for nanocomposites prepared using ultrasonication with dispersing agent at 0.32 phr VGCNF.

3.2.3. Nanocomposite Optimization

Response surface models of the storage and loss moduli may be used to tailor nanocomposite designs in order to obtain enhanced viscoelastic properties over a range of processing conditions. For example, if the goal of a given structural application is to maximize VGCNF/VE storage modulus (stiffness) while simultaneously minimizing the loss modulus, comparing Figure 3.2 and Figure 3.4 suggests that such a nanocomposite will be achieved from using coupled mixing with 0.41 phr pristine VGCNF nanofibers. In addition, a dispersing agent may be used to minimize the liquid resin blend viscosity (if desired) since it will have no significant effect on moduli for this case. Such a determination may not be obvious when employing more traditional, and perhaps *ad hoc*, experimental strategies prevalent in the literature. Thus, response surface models can effectively facilitate nanocomposite design by establishing relationships between materials and processing parameters that lead to improved properties.

3.3. Conclusions

A designed experimental study was conducted to evaluate the effect of formulation and processing factors on the dynamic mechanical (viscoelastic) responses of vapor-grown carbon nanofiber (VGCNF)/vinyl ester (VE) nanocomposites. Statistically reliable response surface models were developed to predict storage and loss moduli as a

function of four independent factors: 1) VGCNF type, 2) use of dispersing agent, 3) mixing method, and 4) VGCNF weight fraction. The coupled effects of each factor on the predicted moduli were explicitly evaluated. The predicted nanocomposite storage modulus was primarily a function of both VGCNF type and weight fraction; the mixing method and use of a dispersing agent did not significantly affect the mean storage modulus. In contrast, the nanofiber weight fraction, mixing method, and presence of dispersing agent all had a significant coupled effect on the predicted loss modulus, while the type of VGCNF was an insignificant factor. The inclusion of relatively small weight fractions of nanofibers (<0.50 parts per hundred parts resin) led to roughly a 20% increase in the predicted storage modulus in comparison to that of the neat cured resin at typical mixing times (<1 hr). The response surface models may be readily used to identify combinations of formulation and processing factors that lead to optimal nanocomposite viscoelastic properties; such a determination would be very difficult using standard test strategies. Employing the methodology outlined here, it is possible to tailor nanocomposite designs in order to obtain enhanced mechanical properties over a range of typical processing conditions. Response surface models can facilitate nanocomposite design by establishing relationships between materials and processing parameters that lead to improved nanocomposite properties.

CHAPTER 4
DYNAMIC MECHANICAL ANALYSIS OF VAPOR-GROWN CARBON
NANOFIBER/VINYL ESTER NANOCOMPOSITES USING
DESIGN OF EXPERIMENTS PART 2: ANALYSIS
WITH TEMPERATURE AS A FACTOR

Polymers are typically used as structural materials below their T_g , the temperature where mechanical properties show a significant change (Nielsen & Landel, 1994). For example, the elastic modulus may decrease by a factor of over 1000 times as the temperature is raised through T_g (Nielsen & Landel, 1994). Therefore, for engineering purposes, the thermal behavior of polymers must be characterized as part of component design and during assessments of the material's in-service performance. The inclusion of the nanoreinforcements may significantly affect the thermo-mechanical behavior of the nano-phased matrix, including its T_g and thermal expansion behavior (Yoon et al., 2002; Ellis & D'Angelo, 2003; Ash et al., 2004; Yasmin et al., 2006; Li et al., 2007). Therefore, knowledge of the relationship between a composite's microstructure and its thermal/mechanical behavior is crucial for design and optimization of material performance.

Since polymers are viscoelastic materials, their thermal behavior is often efficiently studied using DMA (Menard, 1999). The designed experimental study of

VGCNF/VE nanocomposites presented in Chapter 3 is extended to include temperature as a continuous factor. By including temperature in the design, the influence of its variation on the nanocomposites' viscoelastic properties (stiffness and energy dissipation characteristics) during service can be analyzed and incorporated into the response surface models. This provides the material design engineer with a predictive tool for estimation of the nanocomposite mechanical properties at both room and elevated temperatures.

The materials, specimen preparation protocol, and testing procedure for this study have been described previously in sections 3.1.2, 3.1.3, and 3.1.4, respectively. The design is similar to the one in chapter 3, except that temperature is introduced as the fifth factor.

4.1. Statistical Experimental Design

The extended experimental design factors and their respective levels are shown in Table 4.1. A general mixed-level full factorial design was used to investigate and model the effects of three qualitative (discrete) factors on the storage and loss moduli of VGCNF/VE nanocomposites. These factors include the type of VGCNF (A), the use of dispersing agent (B), and the mixing method (C). Additionally, two quantitative (continuous) factors, VGCNF weight fraction (D) and temperature (T), were used. The temperature levels ($T = 30, 60, 90, 120$ °C) were selected in equally spaced intervals ranging from nearly room temperature (30 °C) up to a temperature within the material's T_g region (120 °C). Data analysis was performed using the SAS 9.2 statistical analysis

software (SAS, 2011). The SAS codes for the analyses of storage and loss modulus data are given in Appendix B.

Table 4.1 Factors used for the study and their levels¹.

Factor Designation	Factor	Levels				
		1	2	3	4	5
A	VGCNF ² type	Pristine	Oxidized	-	-	-
B	Use of dispersing agent	No	Yes	-	-	-
C	Mixing method	US ³	HS ⁴	HS/US		
D	VGCNF weight fraction (phr ⁵)	0	0.25	0.50	0.75	1.00
T	Temperature (°C)	30	60	90	120	-

¹ For materials and specimen preparation protocol see sections 3.1.2 and 3.1.3.

² Vapor-grown carbon nanofiber

³ Ultrasonication

⁴ High-shear mixing

⁵ Parts per hundred parts resin

4.2. Results and Discussion

Table 4.2 shows the average storage and loss modulus for each treatment combination (or run) for a total of 240 (2×2×3×5×4) treatment combinations calculated from three separate measurements. As before, the average standard deviation was taken to be 75 MPa for the storage modulus and 5 MPa for the loss modulus. There may actually be some slight changes in the average standard deviations due to large number of treatment combinations in this design. Nevertheless, it was assumed that these values remained essentially the same as those calculated for the four-factor design presented in Chapter 3. Forty eight treatment combinations correspond to the neat resin and these all have the same response values regardless of other factor levels. The neat VE was

considered as part of the design and not as a control factor since it was of critical interest to capture neat VE's responses in the response surface models.

Table 4.2 Randomized treatment combinations and their average responses¹.

Run	A: VGCNF Type	B: Use of dispersing agent	C: Mixing Method	D: VGCNF Weight Fraction (phr)	T: Temperature (°C)	Response 1: Storage Modulus (MPa)	Response 2: Loss Modulus (MPa)
1	Oxidized	Yes	HS ²	1.00	30	2631	49
2	Oxidized	Yes	US ³	0.00	60	1918	70
3	Pristine	No	US	1.00	120	812	150
4	Pristine	No	HS/US	1.00	120	1311	193
5	Pristine	No	HS	0.75	60	2313	58
6	Pristine	Yes	HS	1.00	90	2027	80
7	Oxidized	No	HS	0.00	120	910	109
8	Oxidized	No	US	0.00	60	1918	70
9	Pristine	Yes	HS	0.25	30	2551	50
10	Pristine	Yes	HS	0.75	60	2477	56
11	Pristine	No	HS	0.25	120	1337	171
12	Oxidized	No	HS/US	1.00	120	1352	186
13	Oxidized	Yes	HS/US	1.00	30	2723	45
14	Pristine	No	HS/US	0.00	60	1918	70
15	Pristine	Yes	HS/US	0.00	30	2178	59
16	Oxidized	Yes	HS/US	0.25	30	2528	42
17	Oxidized	No	HS/US	0.75	60	2525	48
18	Oxidized	Yes	US	0.75	60	2373	77
19	Pristine	No	HS/US	0.00	90	1412	92
20	Oxidized	Yes	HS/US	0.75	120	1122	185
21	Pristine	Yes	HS/US	0.25	60	2476	51
22	Oxidized	No	US	0.25	90	1490	97
23	Pristine	Yes	HS	0.75	120	1342	172
24	Oxidized	No	HS/US	0.50	120	1314	193
25	Oxidized	Yes	HS	0.75	30	2676	46
26	Pristine	No	HS	0.25	60	2460	55
27	Pristine	No	HS/US	0.75	60	2435	48
28	Oxidized	Yes	US	0.00	30	2178	59
29	Pristine	Yes	HS	0.00	120	910	109
30	Pristine	Yes	HS	0.75	90	2087	75
31	Oxidized	No	HS	0.25	120	1446	151
32	Pristine	Yes	HS	0.75	30	2702	49
33	Oxidized	No	HS	1.00	60	2480	52
34	Oxidized	Yes	HS	1.00	120	1319	168
35	Oxidized	No	HS	0.75	90	2027	68

Table 4.2 continued on the next page

Table 4.2 continued

Run	A: VGCNF Type	B: Use of dispersing agent	C: Mixing Method	D: VGCNF Weight Fraction (phr)	T: Temperature (°C)	Response 1: Storage Modulus (MPa)	Response 2: Loss Modulus (MPa)
36	Oxidized	No	HS/US	0.25	60	2412	46
37	Oxidized	No	US	0.00	30	2178	59
38	Oxidized	Yes	US	0.50	90	1897	99
39	Pristine	Yes	HS/US	1.00	60	2431	47
40	Pristine	Yes	US	1.00	30	2651	64
41	Pristine	No	HS/US	0.50	30	2598	42
42	Oxidized	Yes	HS	0.25	90	1987	78
43	Pristine	No	US	0.25	120	550	173
44	Pristine	No	HS	0.00	30	2178	59
45	Oxidized	No	HS	1.00	120	1450	152
46	Oxidized	Yes	HS	0.75	120	1391	162
47	Pristine	No	US	0.25	60	2245	131
48	Pristine	No	US	0.00	30	2178	59
49	Pristine	No	HS	0.25	30	2662	47
50	Pristine	No	HS/US	0.25	30	2561	45
51	Oxidized	No	HS	0.75	30	2603	45
52	Oxidized	Yes	HS	0.00	60	1918	70
53	Oxidized	No	HS	0.00	90	1412	92
54	Oxidized	No	HS/US	0.25	90	2017	83
55	Oxidized	No	HS	0.00	60	1918	70
56	Pristine	Yes	HS/US	0.00	90	1412	92
57	Pristine	No	US	0.75	30	2396	44
58	Oxidized	Yes	HS/US	0.00	90	1412	92
59	Oxidized	Yes	HS	1.00	60	2420	53
60	Pristine	Yes	HS/US	0.75	60	2400	48
61	Oxidized	No	HS	1.00	90	2092	71
62	Oxidized	No	US	0.50	60	2247	105
63	Oxidized	Yes	HS	0.25	30	2575	48
64	Oxidized	No	HS/US	0.75	30	2689	43
65	Pristine	No	HS	0.00	90	1412	92
66	Oxidized	No	HS/US	0.00	30	2178	59
67	Pristine	No	US	0.25	90	1548	117
68	Pristine	No	HS/US	1.00	30	2684	42
69	Oxidized	No	HS	1.00	30	2671	45
70	Pristine	No	HS/US	1.00	60	2514	48

Table 4.2 continued on the next page

Table 4.2 continued

Run	A: VGCNF Type	B: Use of dispersing agent	C: Mixing Method	D: VGCNF Weight Fraction (phr)	T: Temperature (°C)	Response 1: Storage Modulus (MPa)	Response 2: Loss Modulus (MPa)
71	Oxidized	No	HS/US	0.75	90	2153	74
72	Pristine	Yes	US	0.75	30	2476	52
73	Oxidized	No	HS	0.50	30	2630	44
74	Pristine	Yes	HS	1.00	120	1214	183
75	Pristine	Yes	HS	0.50	120	1405	176
76	Oxidized	Yes	US	0.75	90	1907	98
77	Oxidized	No	HS/US	1.00	30	2556	42
78	Pristine	No	HS	1.00	60	2475	63
79	Oxidized	No	HS/US	0.50	60	2553	49
80	Pristine	Yes	HS	1.00	60	2426	57
81	Oxidized	Yes	HS/US	1.00	60	2548	49
82	Pristine	No	US	0.50	90	1620	104
83	Oxidized	No	HS/US	0.00	60	1918	70
84	Pristine	Yes	HS/US	1.00	30	2605	43
85	Pristine	Yes	HS	0.25	90	1953	77
86	Pristine	Yes	HS	0.00	60	1918	70
87	Oxidized	No	US	0.50	90	1616	102
88	Pristine	No	US	0.00	60	1918	70
89	Pristine	No	HS	0.00	60	1918	70
90	Pristine	No	HS	0.00	120	910	109
91	Pristine	Yes	US	0.75	60	2236	60
92	Oxidized	Yes	HS/US	1.00	120	1420	186
93	Oxidized	Yes	HS	0.00	90	1412	92
94	Oxidized	Yes	HS/US	0.50	90	1983	77
95	Pristine	No	US	0.75	120	842	149
96	Pristine	Yes	HS/US	0.75	30	2570	42
97	Pristine	No	HS/US	0.25	90	2083	73
98	Pristine	Yes	HS/US	0.00	60	1918	70
99	Oxidized	Yes	US	1.00	60	2323	64
100	Pristine	Yes	US	0.00	30	2178	59
101	Oxidized	No	HS/US	0.75	120	1332	204
102	Pristine	Yes	US	0.75	120	966	167
103	Pristine	Yes	HS/US	0.75	120	1250	171
104	Pristine	No	US	0.75	90	1607	89
105	Pristine	Yes	HS/US	1.00	120	1348	163

Table 4.2 continued on the next page

Table 4.2 continued

Run	A: VGCNF Type	B: Use of dispersing agent	C: Mixing Method	D: VGCNF Weight Fraction (phr)	T: Temperature (°C)	Response 1: Storage Modulus (MPa)	Response 2: Loss Modulus (MPa)
106	Oxidized	No	US	0.25	30	2485	70
107	Oxidized	No	US	0.25	60	2071	103
108	Pristine	Yes	US	0.25	90	1454	108
109	Oxidized	No	HS	0.75	60	2409	52
110	Oxidized	Yes	HS	0.50	120	1196	156
111	Pristine	Yes	HS	0.00	30	2178	59
112	Oxidized	No	US	0.75	60	2199	100
113	Pristine	Yes	US	1.00	90	1867	101
114	Pristine	Yes	HS/US	0.50	30	2766	47
115	Oxidized	Yes	US	0.00	120	910	109
116	Pristine	No	HS/US	0.75	90	2090	75
117	Pristine	No	HS/US	0.00	30	2178	59
118	Pristine	Yes	HS	0.50	60	2521	53
119	Oxidized	No	US	0.25	120	815	149
120	Pristine	Yes	US	0.25	30	2577	79
121	Oxidized	Yes	HS	1.00	90	2043	73
122	Oxidized	Yes	US	0.25	30	2567	73
123	Oxidized	Yes	HS	0.50	60	2369	71
124	Oxidized	Yes	US	0.50	120	1040	176
125	Oxidized	No	US	1.00	60	2185	101
126	Pristine	Yes	US	0.25	120	652	152
127	Oxidized	No	HS/US	0.00	90	1412	92
128	Oxidized	No	HS/US	0.25	30	2572	41
129	Oxidized	Yes	US	0.75	120	1112	165
130	Oxidized	Yes	HS/US	1.00	90	2172	74
131	Oxidized	No	HS	0.00	30	2178	59
132	Pristine	No	US	0.00	90	1412	92
133	Pristine	No	HS/US	0.50	120	1356	175
134	Pristine	No	HS	0.25	90	2065	73
135	Oxidized	Yes	HS/US	0.50	120	1230	188
136	Oxidized	Yes	HS/US	0.75	30	2593	46
137	Pristine	Yes	US	0.25	60	2076	109
138	Pristine	Yes	HS	0.50	90	2126	74
139	Pristine	No	HS	1.00	120	1262	176

Table 4.2 continued on the next page

Table 4.2 continued

Run	A: VGCNF Type	B: Use of dispersing agent	C: Mixing Method	D: VGCNF Weight Fraction (phr)	T: Temperature (°C)	Response 1: Storage Modulus (MPa)	Response 2: Loss Modulus (MPa)
140	Pristine	Yes	HS/US	0.25	30	2657	44
141	Oxidized	Yes	HS	0.75	90	2113	68
142	Oxidized	Yes	HS	0.00	120	910	109
143	Pristine	No	HS	1.00	30	2686	49
144	Oxidized	Yes	HS/US	0.25	90	2014	77
145	Pristine	Yes	US	0.00	120	910	109
146	Pristine	No	US	0.25	30	2716	67
147	Oxidized	Yes	HS/US	0.50	60	2343	51
148	Oxidized	Yes	HS/US	0.00	30	2178	59
149	Pristine	No	HS	0.50	120	981	165
150	Pristine	No	HS/US	0.00	120	910	109
151	Oxidized	Yes	HS/US	0.25	60	2376	48
152	Oxidized	Yes	HS/US	0.75	60	2395	54
153	Pristine	Yes	US	0.00	60	1918	70
154	Pristine	Yes	HS/US	0.25	120	1277	190
155	Oxidized	No	HS	0.25	30	2580	45
156	Oxidized	No	HS	0.50	60	2430	54
157	Pristine	No	US	0.75	60	2117	68
158	Pristine	Yes	US	1.00	120	933	187
159	Oxidized	No	US	0.00	90	1412	92
160	Oxidized	Yes	HS	0.25	60	2385	55
161	Pristine	Yes	US	0.00	90	1412	92
162	Oxidized	Yes	US	0.50	30	2585	58
163	Oxidized	Yes	HS/US	0.50	30	2512	44
164	Oxidized	No	HS/US	0.50	30	2706	43
165	Pristine	No	HS	0.75	30	2486	49
166	Pristine	Yes	US	0.50	30	2501	99
167	Pristine	Yes	HS	0.50	30	2737	49
168	Oxidized	No	US	0.75	30	2597	57
169	Pristine	No	HS/US	0.75	120	1348	168
170	Pristine	Yes	HS/US	0.50	120	1182	190
171	Oxidized	No	US	1.00	120	748	167
172	Pristine	Yes	US	0.50	120	834	159
173	Pristine	Yes	US	0.75	90	1750	86

Table 4.2 continued on the next page

Table 4.2 continued

Run	A: VGCNF Type	B: Use of dispersing agent	C: Mixing Method	D: VGCNF Weight Fraction (phr)	T: Temperature (°C)	Response 1: Storage Modulus (MPa)	Response 2: Loss Modulus (MPa)
174	Pristine	No	HS	0.50	90	1755	103
175	Pristine	Yes	HS/US	0.75	90	2010	82
176	Oxidized	Yes	HS/US	0.00	120	910	109
177	Pristine	No	US	0.00	120	910	109
178	Pristine	No	HS/US	0.25	120	1405	158
179	Oxidized	No	US	0.50	30	2634	59
180	Oxidized	Yes	US	0.25	120	1042	150
181	Oxidized	Yes	HS/US	0.00	60	1918	70
182	Pristine	No	HS	0.50	60	2315	51
183	Oxidized	No	HS/US	0.00	120	910	109
184	Oxidized	Yes	US	1.00	120	1103	179
185	Pristine	Yes	US	1.00	60	2413	69
186	Pristine	Yes	HS/US	0.50	60	2553	59
187	Oxidized	Yes	US	0.50	60	2345	67
188	Pristine	Yes	HS/US	0.50	90	2050	96
189	Oxidized	No	US	0.50	120	747	175
190	Oxidized	No	HS	0.25	90	2067	65
191	Oxidized	No	HS	0.75	120	1385	152
192	Oxidized	Yes	US	0.00	90	1412	92
193	Pristine	No	US	1.00	30	2443	43
194	Oxidized	No	US	1.00	90	1579	109
195	Pristine	No	HS/US	1.00	90	2132	78
196	Pristine	No	US	1.00	60	2188	70
197	Pristine	Yes	US	0.50	90	1618	99
198	Oxidized	No	HS/US	0.50	90	2167	85
199	Pristine	Yes	US	0.50	60	2160	98
200	Pristine	No	HS	0.75	90	1948	75
201	Pristine	No	HS/US	0.50	60	2442	47
202	Oxidized	No	HS/US	1.00	90	2085	67
203	Pristine	Yes	HS	0.25	120	1328	142
204	Oxidized	No	US	0.00	120	910	109
205	Oxidized	Yes	HS/US	0.75	90	1987	92
206	Oxidized	Yes	US	0.25	60	2158	99
207	Oxidized	No	HS/US	0.25	120	1071	208

Table 4.2 continued on the next page

Table 4.2 continued

Run	A: VGCNF Type	B: Use of dispersing agent	C: Mixing Method	D: VGCNF Weight Fraction (phr)	T: Temperature (°C)	Response 1: Storage Modulus (MPa)	Response 2: Loss Modulus (MPa)
208	Oxidized	Yes	HS	0.75	60	2482	52
209	Pristine	Yes	HS	0.25	60	2361	56
210	Oxidized	Yes	HS/US	0.25	120	1250	184
211	Oxidized	Yes	US	1.00	90	1921	86
212	Oxidized	Yes	HS	0.50	30	2641	60
213	Pristine	Yes	HS	1.00	30	2664	51
214	Pristine	Yes	HS	0.00	90	1412	92
215	Oxidized	Yes	US	1.00	30	2557	67
216	Oxidized	Yes	US	0.25	90	1686	94
217	Pristine	Yes	HS/US	1.00	90	2054	71
218	Pristine	No	HS	0.50	30	2520	43
219	Pristine	No	US	0.50	60	2275	104
220	Pristine	No	HS	1.00	90	2025	88
221	Oxidized	No	US	0.75	120	781	166
222	Pristine	No	HS	0.75	120	1170	185
223	Oxidized	No	HS	0.25	60	2420	49
224	Oxidized	Yes	US	0.75	30	2641	67
225	Pristine	Yes	HS/US	0.25	90	2079	78
226	Pristine	Yes	HS/US	0.00	120	910	109
227	Oxidized	No	US	1.00	30	2575	53
228	Oxidized	Yes	HS	0.25	120	1317	152
229	Oxidized	Yes	HS	0.00	30	2178	59
230	Pristine	No	US	1.00	90	1600	103
231	Pristine	No	HS/US	0.75	30	2568	44
232	Pristine	No	HS/US	0.50	90	2092	69
233	Oxidized	No	HS	0.50	90	2027	71
234	Oxidized	No	HS/US	1.00	60	2408	47
235	Oxidized	No	HS	0.50	120	1388	152
236	Oxidized	No	US	0.75	90	1598	100
237	Pristine	No	US	0.50	120	808	163
238	Pristine	No	HS/US	0.25	60	2400	49
239	Pristine	No	US	0.50	30	2651	50
240	Oxidized	Yes	HS	0.50	90	1920	95

¹ The average value of three independent samples was used to obtain the responses. The average standard deviations were assumed to be the same as in Chapter 3 (75 MPa for the storage modulus and 5 MPa for the loss modulus data).

² HS = high-shear mixing

³ US = ultrasonication

4.2.1. Statistical Analysis of the Storage Modulus Data

The storage modulus data were analyzed using ANOVA before predictive response surface models were developed (see SAS program codes in Appendix B). Each treatment combination was replicated once. Thus, there was no experimental error associated with the storage modulus data. To construct an error term for the ANOVA, it was assumed that four- and five-factor interactions (the two highest order interactions) were negligible. The ANOVA results are shown in Table 4.3, where the main, two-, and three-factor interaction effects were studied. Ordered F -tests (Ellison et al., 2009), or equivalently a test of p -values determined from the F statistics, were conducted on the factorial effects starting from the highest order (three-factor) interactions. For this analysis, the factorial effects with p -values less than $\alpha = 0.05$ (5% level of significance) were considered significant (Table 4.3). On this basis, five three-factor interactions (all underlined in Table 4.3) were considered significant. These include:

- 1) Interaction between the VGCNF type (A), the use of dispersing agent (B), and the mixing method (C), i.e., $A \times B \times C$;
- 2) Interaction between the VGCNF type (A), the use of dispersing agent (B), and the VGCNF weight fraction (D), i.e., $A \times B \times D$;
- 3) Interaction between the use of dispersing agent (B), the mixing method (C), and the VGCNF weight fraction (D), i.e., $B \times C \times D$;
- 4) Interaction between the use of dispersing agent (B), the mixing method (C), and the temperature (T), i.e., $B \times C \times T$;
- 5) Interaction between the mixing method (C), the VGCNF weight fraction (D), and the temperature (T), i.e., $C \times D \times T$.

Table 4.3 Analysis of variance (ANOVA) for the storage modulus data.

Source of Variation	Degrees of Freedom	Sum of Squares	Mean Square	F-value	p-value ¹
Model	141	81807482.39	580194.91	126.28	<.0001
A: VGCNF Type	1	28427.27	28427.27	6.19	0.0146
B: Use of Dispersing Agent	1	49020.42	49020.42	10.67	0.0015
C: Mixing Method	2	2466492.17	1233246.09	268.43	<.0001
D: VGCNF Weight fraction	4	6441727.23	1610431.81	350.52	<.0001
T: Temperature	3	69692014.43	23230671.48	5056.36	<.0001
A×B	1	546.02	546.02	0.12	0.7310
A×C	2	46155.81	23077.90	5.02	0.0084
A×D	4	35429.23	8857.31	1.93	0.1118
A×T	3	21266.70	7088.90	1.54	0.2082
B×C	2	137845.41	68922.70	15.00	<.0001
B×D	4	50122.67	12530.67	2.73	0.0335
B×T	3	9973.88	3324.63	0.72	0.5402
C×D	8	694447.12	86805.89	18.89	<.0001
C×T	6	767507.29	127917.88	27.84	<.0001
D×T	12	426069.73	35505.81	7.73	<.0001
<u>A×B×C</u>	<u>2</u>	<u>114141.01</u>	<u>57070.50</u>	<u>12.42</u>	<u><.0001</u>
<u>A×B×D</u>	<u>4</u>	<u>74059.23</u>	<u>18514.81</u>	<u>4.03</u>	<u>0.0046</u>
A×B×T	3	6214.88	2071.63	0.45	0.7172
A×C×D	8	40655.07	5081.88	1.11	0.3658
A×C×T	6	26980.32	4496.72	0.98	0.4438
A×D×T	12	46375.13	3864.59	0.84	0.6083
<u>B×C×D</u>	<u>8</u>	<u>256564.38</u>	<u>32070.55</u>	<u>6.98</u>	<u><.0001</u>
<u>B×C×T</u>	<u>6</u>	<u>78605.19</u>	<u>13100.87</u>	<u>2.85</u>	<u>0.0133</u>
B×D×T	12	12397.37	1033.11	0.22	0.9968
<u>C×D×T</u>	<u>24</u>	<u>284444.42</u>	<u>11851.85</u>	<u>2.58</u>	<u>0.0006</u>
Error	98	450246.01	4594.35	-	-
Total (Corrected)	239	82257728.40	-	-	-
Other Model Statistics					
Mean: 1929.200			R ² : 0.995		
Coefficient of variation: 3.51%			Standard deviation: 67.78		

¹ Values <0.05 are considered significant in the analysis.

Note: The underlined three-factor interactions are significant. The lower order significant interactions were not considered in the analysis, because they are all contained in higher order interactions.

Most of the factors and their two-factor interactions in Table 4.3 were not “clean”, i.e., were completely contained in higher order significant three-factor interactions. Therefore, the two-factor interactions and main factors were not further analyzed even if

their p -values were less than 0.05. The only clean two-factor interaction, i.e., A×B interaction, was insignificant (p -value = 0.2082 > 0.05). Two quantitative factors were used to generate the response surface models: VGCNF weight fraction (D) and temperature (T). Without any analysis, 12 different response surfaces (3D surfaces) could be generated from all combinations of the qualitative factors ($2 \times 2 \times 3 = 12$ combinations, where the numbers denote factor levels) as functions of VGCNF weight fraction and temperature. The analysis of significant A×B×C interaction, where all three factors are qualitative, can be enlightening in determining the significant factor combinations (out of the 12 combinations) in order to reduce the total number of generated response surfaces. All the other significant three-factor interactions involve the quantitative factors, i.e., VGCNF weight fraction and temperature, which are considered in the response surfaces anyway. So, they were not further analyzed. On this basis, Fisher's LSD multiple comparisons (Myers et al., 2009) were conducted on the mean data associated with the A×B×C interaction to isolate significant factor combinations. The results are shown in Table 4.4, where the mean data associated with each VGCNF type/dispersing agent/mixing method combination is compared with the mean data for the other combinations. In the LSD comparisons, an LSD value is calculated (Myers et al., 2009) and t -tests are run on pair-wise differences between the mean data. If the calculated t -value is greater than the LSD value, the difference is deemed significant and vice versa. These comparisons of the mean data are better represented by a format introduced in Table 4.4. Comparing any two mean data, only those with differing letters in the t -grouping column, which is constructed from the results of the t -tests, are significantly different from each other. The letters in the t -grouping column, which can be composed

of two or more sub-columns, are arbitrary and only used for visualization purposes. In this respect, there could be more than one letter associated with a mean data depending on the complexity of the relationships between the means. The neighboring pairs with no significant difference are “linked” together with a similar letter to better give a total picture of the significant versus insignificant differences. This is better understood with an example: The combination pristine/no dispersing agent/(HS/US) has letters V and W in its *t*-grouping column and therefore, its associated mean storage modulus is significantly different from the mean storage modulus for the combination pristine/no dispersing agent/HS, which has only letter X in its *t*-grouping column. If a single letter was common between the two combinations, then it would have resulted in an insignificant difference.

The first eight combinations in Table 4.4, i.e., high-shear mixing and coupled high-shear mixing/ultrasonication combinations, are “chained” in the *t*-grouping column, i.e., most of the combinations have mean storage moduli that are not significantly different from each other. In general, a set of mean data are chained if a blank row cannot be located between the groups of letters in their *t*-grouping column with its sub-columns. The data associated with the first eight combinations can be grouped into one set of mean storage modulus data for the purpose of response surface modeling. The same is true for the last three combinations involving ultrasonication, where these are chained in the *t*-grouping column. The combination of oxidized VGCNF/dispersing agent/ultrasonication is the only combination differing significantly from the other combinations involving ultrasonication. Therefore, three separate response surfaces were generated for the data associated with the combinations of the qualitative factors (Table 4.4): 1) high-shear

mixing or coupled high-shear mixing (HS or HS/US), 2) oxidized VGCNF/dispersing agent/ultrasonication combination (OX/DA/US), and 3) other ultrasonication combinations (US (Other)). Hence, the 12 possible response surfaces were reduced to only three, simplifying data analysis and subsequent modeling.

Table 4.4 Multiple comparison results for the mean storage modulus data using least significant differences (LSD) for the interaction between the VGCNF type, use of dispersing agent, and mixing method (A×B×C).

<i>t</i> -grouping	Least squares means for the storage modulus data	VGCNF type (A)	Use of dispersing agent (B)	Mixing method (C)	
	V ¹	2026.2	Oxidized	No	HS ²
	V				
W	V	2021.9	Pristine	No	HS/US ³
W	V				
W	V	2017.0	Pristine	Yes	HS
W	V				
W	V	2016.5	Oxidized	No	HS/US
W	V				
W	V	2006.3	Pristine	Yes	HS/US
W	V				
W	V	1994.2	Oxidized	Yes	HS
W	V				
W	X	1980.7	Oxidized	Yes	HS/US
	X				
	X	1943.9	Pristine	No	HS
	Y	1883.8	Oxidized	Yes	US
	Z	1779.1	Pristine	Yes	US
	Z				
	Z	1741.8	Pristine	No	US
	Z				
	Z	1739.3	Oxidized	No	US

¹ Least squares means with the same letters are not significantly different from each other.

² High-shear mixing

³ Ultrasonication

A general cubic response surface model for two independent variables (X_1 and X_2) can be expressed as:

$$Y_i = \beta_0 + \sum_{i=1}^2 \beta_i X_i + \sum_{i=1}^2 \beta_{ii} X_i^2 + \beta_{12} X_1 X_2 + \sum_{i=1}^2 \beta_{iii} X_i^3 + \beta_{112} X_1^2 X_2 + \beta_{122} X_1 X_2^2 + e_i \quad (4.1)$$

where Y_i is the dependent variable, β_0 is the intercept, all the other β 's are model parameters, and e_i is the model error term. Here, VGCNF weight fraction ($X_1 = D$) and temperature ($X_2 = T$) were independent variables and the storage modulus ($Y_i = S$) was the dependent variable. Cubic equations were fitted to the mean storage modulus data and through backward elimination (Kleinbaum & Klein, 2010), the insignificant model terms were removed to further revise the model. This involved conducting t -tests for the parameters by comparing their p -values, which are associated with their calculated t -values. Those with p -values greater than 0.05 (5% level of significance) were removed. However, based on the "hierarchy principle" (Kleinbaum & Klein, 2010), the lower order terms completely contained in significant higher order terms were retained in the models. The results of the regression analyses are summarized in Table 4.5. In this table, the model parameters, their estimates, their associated t - and p -values (Ott & Longnecker, 2010), and R^2 and adjusted R^2 values are shown. Parameters with p -values of less than $\alpha = 0.05$ were considered significant model terms. The t -values are given for reference purposes.

Table 4.5 Regression analyses for the storage modulus data.

Paramter	Degrees of Freedom	Parameter Estimate	Standard Error	t-value	p-value
High-shear mixing or coupled high-shear mixing/ultrasonication ($R^2 = 0.978$, adjusted $R^2 = 0.977$):					
β_0	1	2231.233929	64.1016676	34.81	<.0001
β_1	1	2567.261905	180.2160148	14.25	<.0001
β_2	1	0.937833	1.9293903	0.49	0.6276
β_{11}	1	-5025.928571	377.4531662	-13.32	<.0001
β_{12}	1	10.584167	3.1506811	3.36	0.0010
β_{22}	1	-0.102306	0.0126616	-8.08	<.0001
β_{111}	1	2678.666667	248.1158940	10.80	<.0001
β_{122}	1	-0.072028	0.0206763	-3.48	0.0006
Ultrasonication with Oxidized VGCNF and Dispersing agent ($R^2 = 0.996$, adjusted $R^2 = 0.994$):					
β_0	1	2398.407143	104.5460584	22.94	<.0001
β_1	1	1299.742857	292.7751728	4.44	0.0008
β_2	1	-4.311762	3.0644601	-1.41	0.1848
β_{11}	1	-1341.142857	242.9620681	-5.52	0.0001
β_{12}	1	6.979429	5.7812910	1.21	0.2506
β_{22}	1	-0.068278	0.0199637	-3.42	0.0051
β_{112}	1	8.068571	2.9572401	2.73	0.0183
β_{122}	1	-0.108444	0.0326005	-3.33	0.0060
Ultrasonication (other combinations) ($R^2 = 0.980$, adjusted $R^2 = 0.977$):					
β_0	1	2439.054762	127.7898839	19.09	<.0001
β_1	1	1383.961905	357.8681579	3.87	0.0003
β_2	1	-4.315127	3.7457845	-1.15	0.2546
β_{11}	1	-1355.428571	296.9800578	-4.56	<.0001
β_{12}	1	-4.104762	7.0666510	-0.58	0.5638
β_{22}	1	-0.074944	0.0244022	-3.07	0.0034
β_{112}	1	14.046984	3.6147262	3.89	0.0003
β_{122}	1	-0.083259	0.0398486	-2.09	0.0416

Note: The significant model parameters are different for each of the three combinations.

Based on the LSD multiple comparison results in Table 4.4 and regression analyses in Table 4.5, the response surface models are expressed as:

$$S_{HS \text{ or } HS/US} = 2231.2 + 2567.3D + 0.9T - 5025.9D^2 - 10.6DT - 0.1T^2 + 2678.7D^3 - 0.07DT^2 \quad (4.2)$$

$$S_{OX/DA/US} = 2398.4 + 1299.7D - 4.3T - 1341.1D^2 + 7.0DT - 0.07T^2 + 8.1D^2T - 0.1DT^2 \quad (4.3)$$

$$S_{US \text{ (other)}} = 2439.1 + 1384.0D - 4.3T - 1355.4D^2 - 4.1DT - 0.07T^2 + 14.0D^2T - 0.08DT^2 \quad (4.4)$$

where S is the storage modulus, D is the VGCNF weight fraction, and T is the temperature. The subscripts HS , US , OX , and DA stand for high-shear mixing, ultrasonication, oxidized VGCNF, and dispersing agent, respectively. The subscript “other” denotes all other ultrasonication combinations except for $OX/DA/US$. These models describe 97.8%, 99.6%, and 98.0% of the variations in the mean storage modulus for HS or HS/US , $OX/DA/US$, and US (other) cases, respectively. The three response surfaces for the storage modulus versus temperature and VGCNF weight fraction for HS or HS/US , $OX/DA/US$, and US (other) are shown in Figures 4.1, 4.2, and 4.3. In these figures, the 3D surfaces are color-coded to indicate regions of high (red) and of low storage modulus (blue). The contour plots are also shown on the xy planes to show the regions with constant storage modulus. Overall, the storage modulus decreases with increasing temperature for all three combinations. Furthermore, an overall increase in the storage modulus is observed for the VGCNF/VE nanocomposites compared to the neat VE.

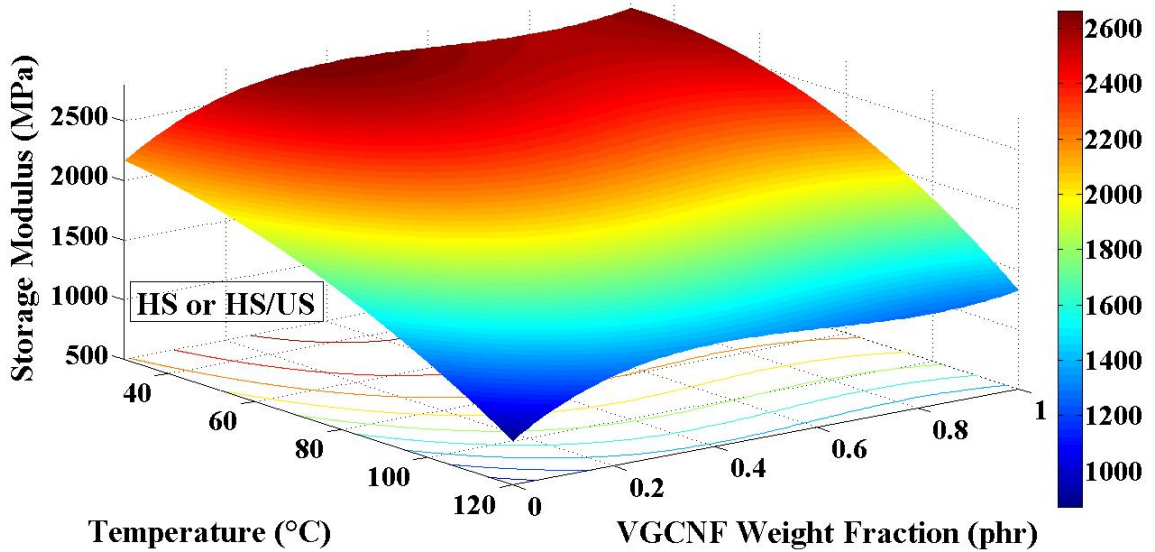


Figure 4.1 The predicted response surface and contour plots for the storage modulus as a function of VGCNF weight fraction and temperature for the case where either high-shear mixing (HS) or coupled high-shear mixing/ultrasonication (HS/US) is used.

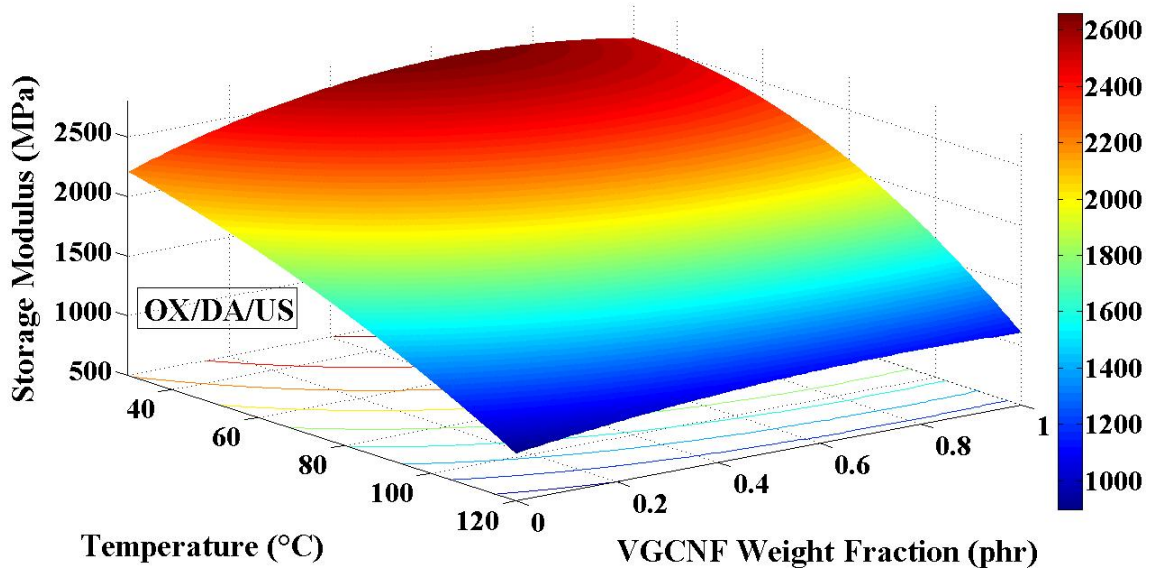


Figure 4.2 The predicted response surface and contour plots for the storage modulus as a function of VGCNF weight fraction and temperature for the case where oxidized VGCNF (OX), dispersing agent (DA), and ultrasonication (US) are used.

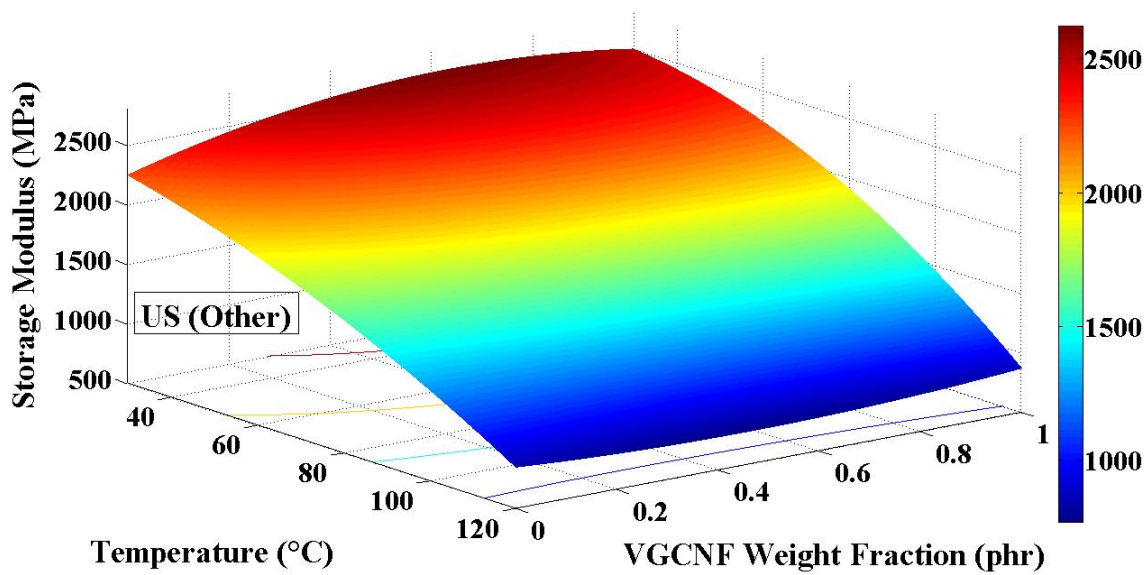


Figure 4.3 The predicted response surface and contour plots for the storage modulus as a function of VGCNF weight fraction and temperature for the case where ultrasonication (US) is used with any of combinations other than that of oxidized VGCNF and dispersing agent.

Two-dimensional (2D) graphs were generated from the response surfaces in Figures 4.1, 4.2, and 4.3 (or Equations 4.2, 4.3, and 4.4) to better depict the behavior of the predicted storage modulus as a function of VGCNF weight fraction and temperature. Figure 4.4 shows the predicted storage modulus as a function of temperature for different fixed VGCNF weight fractions. In this figure, all VGCNF weight fractions show a marked increase in the predicted storage modulus over the entire temperature range compared to that of neat VE (0 phr).

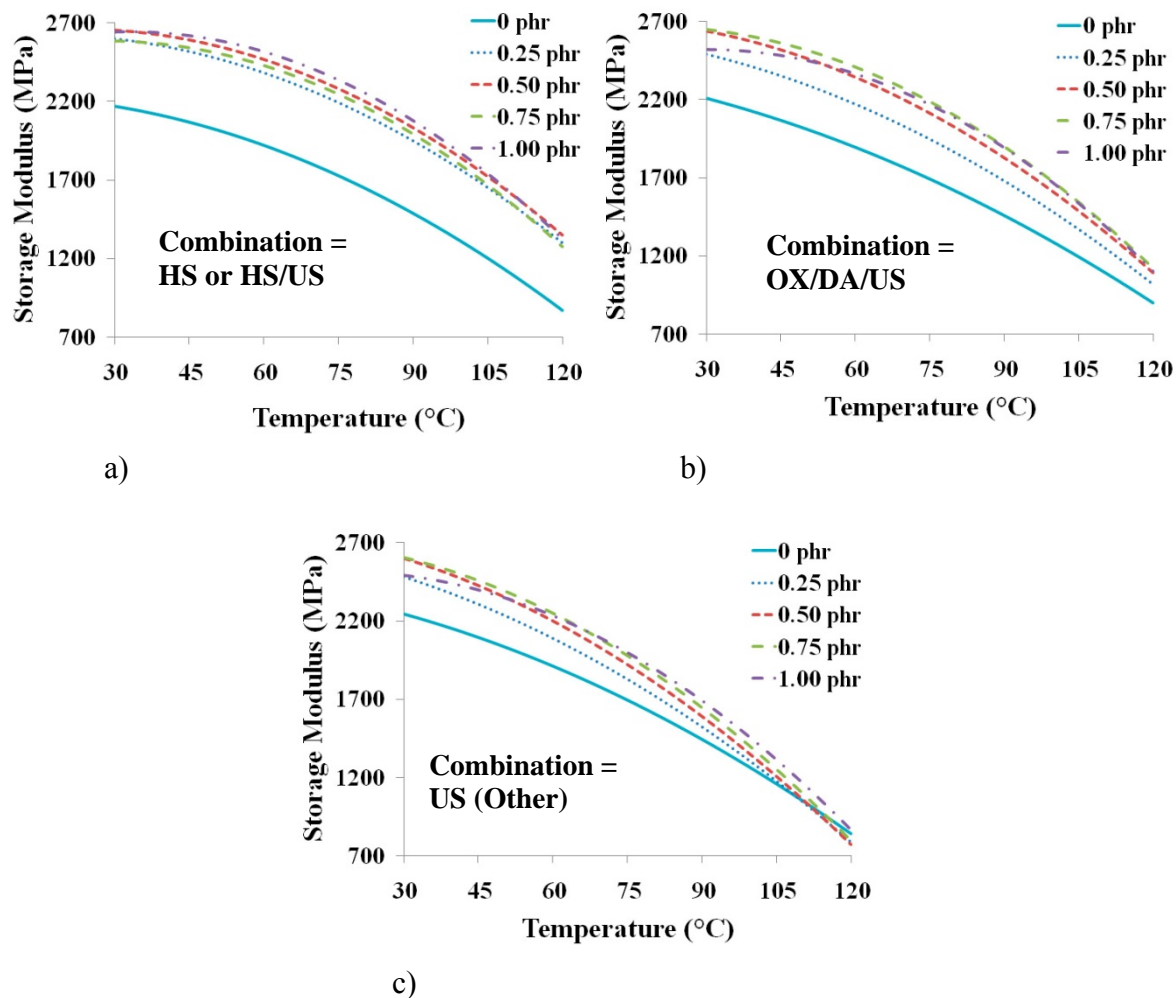


Figure 4.4 Predicted storage modulus as a function of temperature for different VGCNF weight fractions for three cases: a) high-shear mixing (HS) or high-shear mixing/ultrasonication (HS/US), b) oxidized VGCNF/dispersing agent/ultrasonication combination (OX/DA/US), and c) ultrasonication with other combinations except in b) (US (Other)).

Below 45 °C (Figure 4.4), a VGCNF weight fraction of 0.50 phr gave the highest predicted storage modulus for all three cases, HS or HS/US, OX/DA/US, and US (other). At the same temperature range, a VGCNF weight fraction of 1.00 phr and 0.75 phr also gave the highest predicted storage modulus (comparable with the 0.50 phr case) for HS or HS/US and the other two US combinations, respectively. However, the 0.50 phr weight

fraction is recommended because of lower cost associated with the use of nanofibers, and lower VGCNF/VE resin blend viscosity. Above 45 °C, there is a slight change in the order of highest predicted storage modulus between VGCNF weight fractions of 0.50, 0.75, and 1.00 phr for all three combinations. For the HS or HS/US combination, the VGCNF weight fraction of 1.00 phr yields slightly higher storage moduli. For the other two combinations, VGCNF weight fractions of 0.75 and 1.00 phr yield slightly higher storage moduli. The VGCNF weight fraction of 0.50 phr can still be considered the recommended weight fraction because these changes are minor. Compare this value to the optimal VGCNF weight fractions predicted for the storage modulus in Chapter 3 (0.37 phr for the pristine and 0.54 phr for the oxidized VGCNFs), respectively. Here, the highest storage modulus over the entire temperature range of study is considered.

In Figure 4.5, the predicted storage moduli are plotted as functions of VGCNF weight fraction for different temperatures. While the predicted storage moduli decreased as the temperature increased, the shapes of the plots remained essentially the same. This suggests that the effect of VGCNF weight fraction on the predicted storage modulus remained essentially unchanged at elevated temperatures.

Based on the LSD comparisons (Table 4.4) and the developed response surface models (Equations 4.2-4.4) HS or HS/US gave higher mean storage modulus over the entire temperature range compared to all the other US combinations. The three cases of HS or HS/US, OX/DA/US, and US (other) combinations are compared for different VGCNF weight fractions as functions of temperature in Figure 4.6. In this figure, the HS or HS/US mixing method yielded the highest predicted storage modulus for all VGCNF

weight fractions (except for 0.75 phr at temperatures below ~ 45 °C). This was especially true for the recommended VGCNF weight fraction of 0.50 phr.

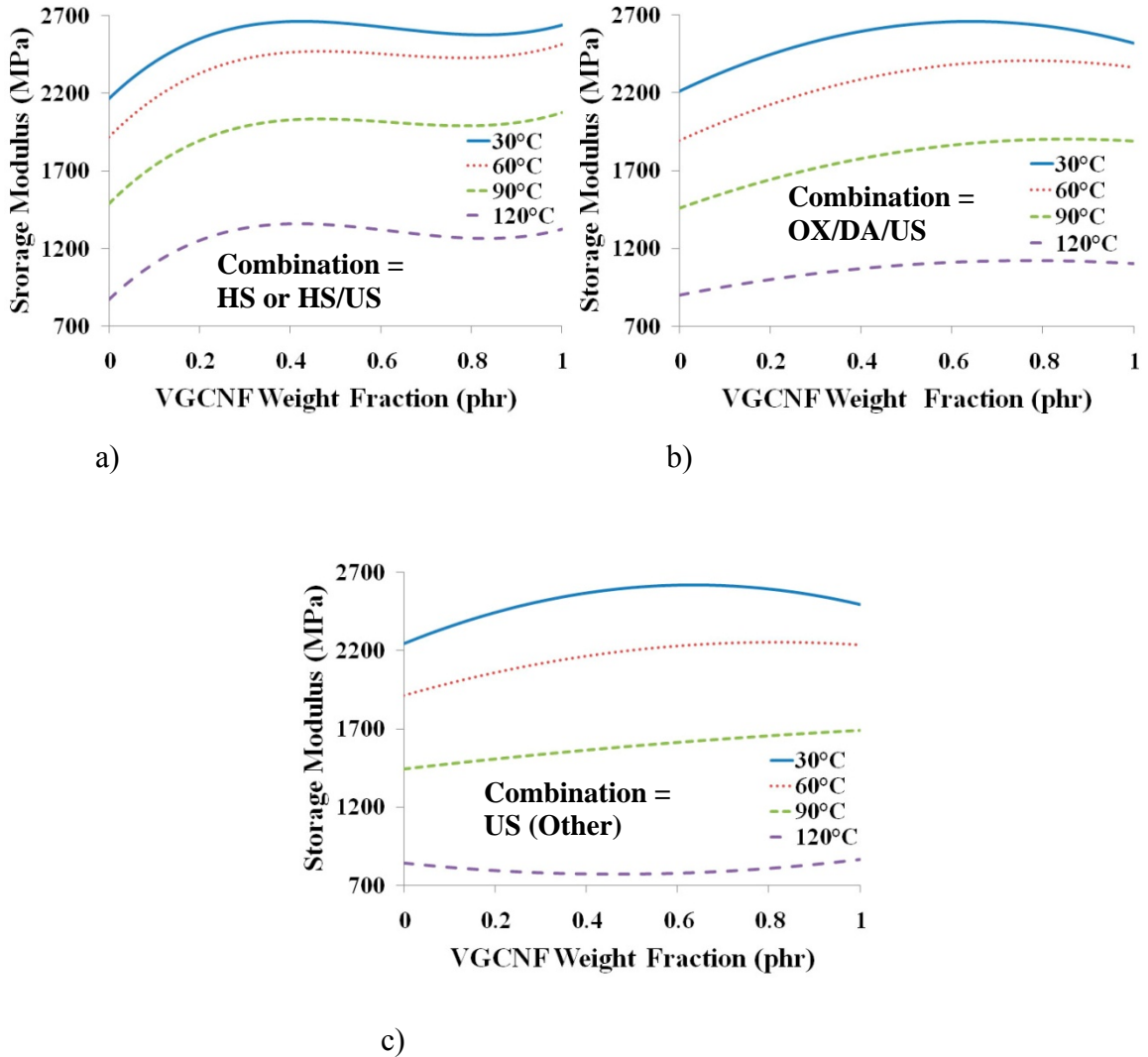


Figure 4.5 Predicted storage modulus as a function of VGCNF weight fraction for different temperatures for three cases: a) high-shear mixing (HS) or high-shear mixing/ultrasonication (HS/US), b) oxidized VGCNF/dispersing agent/ultrasonication combination (OX/DA/US), and c) ultrasonication with other combinations except in b) (US (Other)).

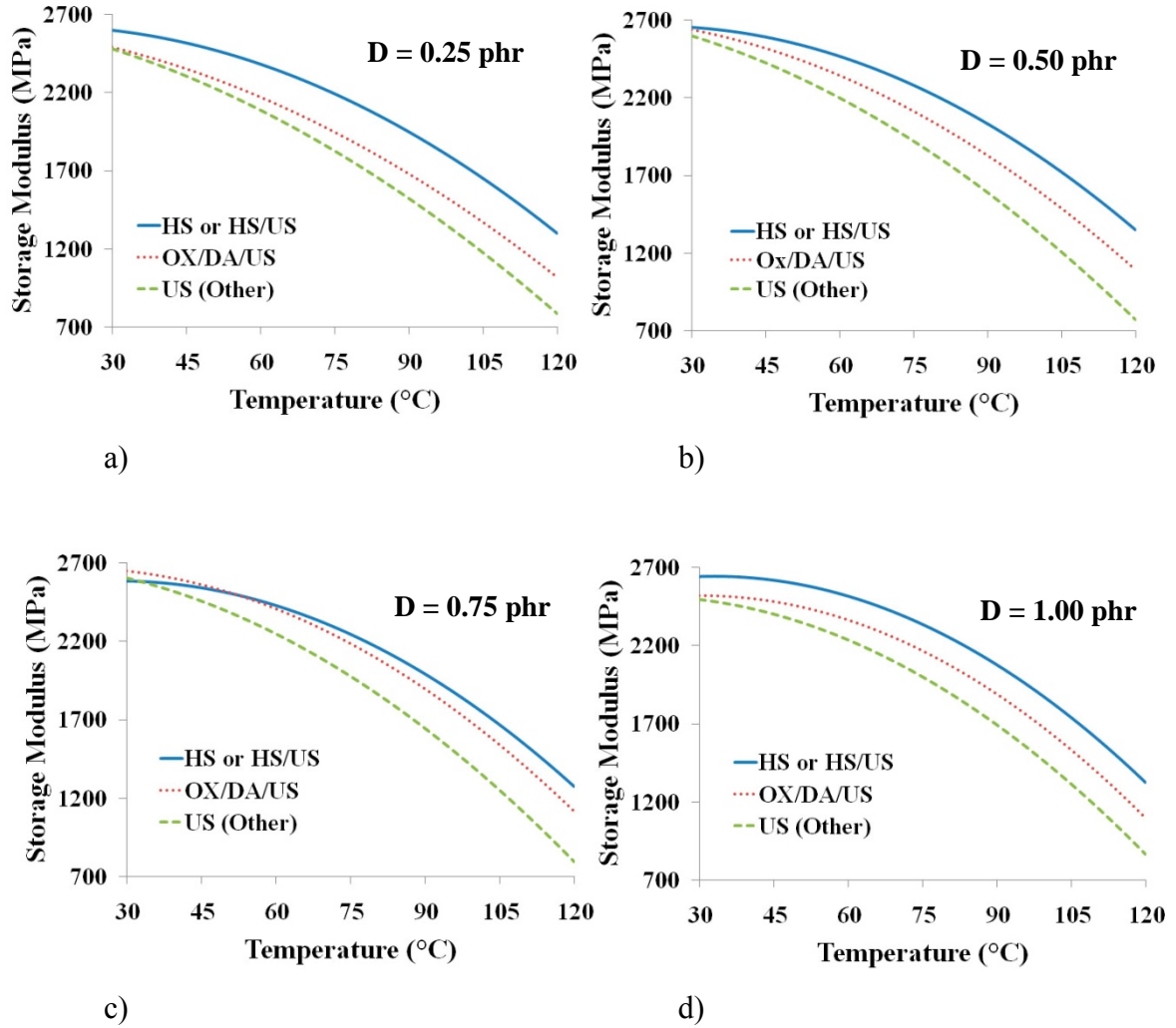


Figure 4.6 Comparisons between predicted storage modulus for high-shear mixing (HS) or high-shear mixing/ultrasonication (HS/US), oxidized VGCNF/dispersing agent/ultrasonication combination (OX/DA/US), and ultrasonication with other combinations (US (Other)) for VGCNF weight fractions (D) of a) 0.25 phr, b) 0.50 phr, c) 0.75 phr, and d) 1.00 phr.

In Figure 4.7, the predicted storage moduli are plotted as functions of VGCNF weight fraction for different mixing combinations (HS or HS/US, OX/DA/US, and US (other)) at different temperatures (30-120 °C). All three mixing combinations demonstrated nearly the same behavior when the temperature was around 30 °C (Figure

4.7a). This is consistent with the results obtained for the room temperature analysis in Chapter 3, where the storage modulus was independent of the mixing method. As the temperature increased, the HS or HS/US method showed a markedly higher storage modulus over the entire range of the VGCNF weight fractions than did all of the US combinations, i.e., OX/DA/US and US (Other) combinations.

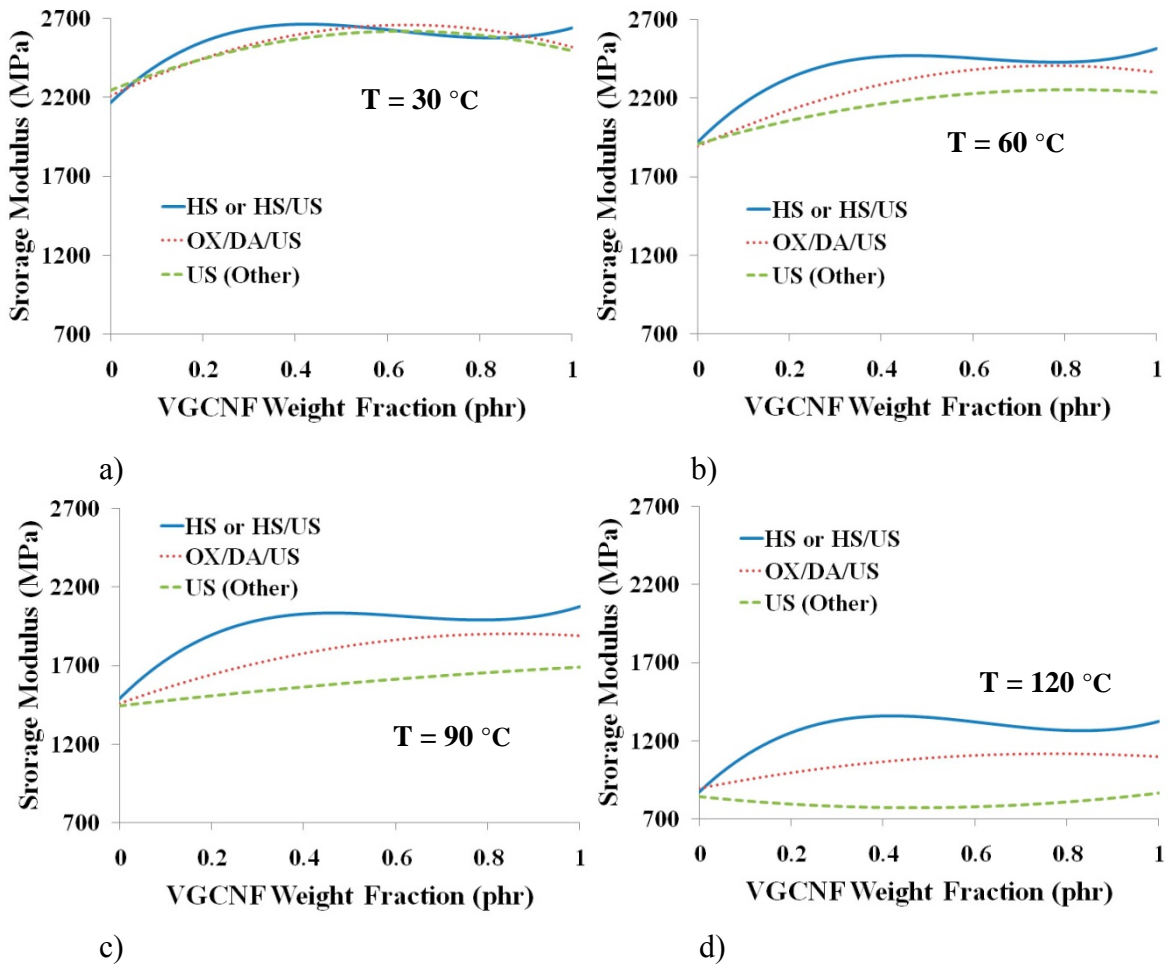


Figure 4.7 Comparisons between predicted storage modulus for high-shear mixing (HS) or high-shear mixing/ultrasonication (HS/US), oxidized VGCNF/dispersing agent/ultrasonication combination (OX/DA/US), and ultrasonication with other combinations (US (Other)) for temperatures (T) of a) 30 °C, b) 60 °C, c) 90 °C, and d) 120 °C.

Since the effects of HS and HS/US mixing methods on the predicted storage moduli of VGCNF/VE nanocomposites were not significantly different (Table 4.4), the HS method is recommended for maximizing the storage modulus over the entire temperature range (30-120 °C) because it takes less time at less cost. On this basis, a careful examination of the HS combinations in Table 4.4 reveals that oxidized VGCNFs

in the absence of dispersing agent, or pristine VGCNFs in the presence of dispersing agent are preferred for maximizing the storage modulus. So, depending on cost considerations, either combination may be used.

The LSD multiple comparisons in Table 4.4 suggest that the use of dispersing agent in conjunction with high-shear mixing boosts the storage modulus of the nanocomposites prepared from pristine VGCNFs over the entire temperature range, but has no significant effect on the storage modulus of nanocomposites prepared from oxidized VGCNFs. Furthermore, the effect of VGCNF surface oxidation on the nanocomposite's storage modulus was similar to the use of dispersing agent for specimens prepared using high-shear mixing. These two options provide flexibility in the formulation of VGCNF/VE nanocomposites with the goal of maximizing the storage modulus over a range of temperatures. For specimens prepared using ultrasonication, both the use of oxidized VGCNFs and dispersing agent are needed to achieve a significantly higher nanocomposite storage modulus compared to other combinations. The use of high-shear mixing should result in better nanofiber dispersions in VE. This dispersion influences the storage modulus at higher temperatures.

4.2.2. Statistical Analysis of the Loss Modulus Data

Similar to the storage modulus data, the ANOVA was used to analyze the loss modulus data before predictive response surface models were developed (see Appendix B for the SAS program codes). Since each treatment combination was replicated once, there was no experimental error associated with the loss modulus data. The four- and five-factor interactions were assumed to be negligible for the loss modulus data to construct an error term for the ANOVA analysis. The ANOVA results are shown in Table 4.6. In this table, factorial effects were analyzed using ordered F -tests starting from the three-factor interactions. The factorial effects with p -values less than $\alpha = 0.05$ (5% level of significance) were considered significant. By comparing the actual p -values of the factorial effects with the selected α value (0.05), five significant three-factor effects (underlined in Table 4.6) were isolated:

- 1) Interaction between the VGCNF type (A), the use of dispersing agent (B), and the mixing method (C), i.e., $A \times B \times C$;
- 2) Interaction between the VGCNF type (A), the mixing method (B), and the VGCNF weight fraction (D), i.e., $A \times C \times D$;
- 3) Interaction between the VGCNF type (A), the mixing method (C), and the temperature (T), i.e., $A \times C \times T$;
- 4) Interaction between the use of dispersing agent (B), the mixing method (C), and the temperature (T), i.e., $B \times C \times T$;
- 5) Interaction between the mixing method (C), the VGCNF weight fraction (D), and the temperature (T), i.e., $C \times D \times T$.

Table 4.6 Analysis of variance (ANOVA) for the loss modulus data.

Source of Variation	Degrees of Freedom	Sum of Squares	Mean Square	F-value	p-value ¹
Model	141	477367.8667	3385.5877	49.25	<.0001
A: VGCNF Type	1	12.1500	12.1500	0.18	0.6751
B: Use of Dispersing Agent	1	32.2667	32.2667	0.47	0.4949
C: Mixing Method	2	9460.1083	4730.0542	68.81	<.0001
D: VGCNF Weight fraction	4	4900.8583	1225.2146	17.82	<.0001
T: Temperature	3	397789.1000	132596.3667	1928.86	<.0001
A×B	1	22.8167	22.8167	0.33	0.5659
A×C	2	672.3250	336.1625	4.89	0.0095
A×D	4	455.8083	113.9521	1.66	0.1660
A×T	3	86.3500	28.7833	0.42	0.7400
B×C	2	67.6083	33.8042	0.49	0.6131
B×D	4	173.2750	43.3187	0.63	0.6421
B×T	3	563.6333	187.8778	2.73	0.0478
C×D	8	4117.7667	514.7208	7.49	<.0001
C×T	6	12349.7250	2058.2875	29.94	<.0001
D×T	12	35027.6083	2918.9674	42.46	<.0001
<u>A×B×C</u>	<u>2</u>	<u>736.5583</u>	<u>368.2792</u>	<u>5.36</u>	<u>0.0062</u>
A×B×D	4	97.0583	24.2646	0.35	0.8414
A×B×T	3	75.6167	25.2056	0.37	0.7772
<u>A×C×D</u>	<u>8</u>	<u>1738.4667</u>	<u>217.3083</u>	<u>3.16</u>	<u>0.0032</u>
<u>A×C×T</u>	<u>6</u>	<u>1037.3750</u>	<u>172.8958</u>	<u>2.52</u>	<u>0.0263</u>
A×D×T	12	318.8583	26.5715	0.39	0.9655
B×C×D	8	269.8500	33.7312	0.49	0.8602
<u>B×C×T</u>	<u>6</u>	<u>1445.2917</u>	<u>240.8819</u>	<u>3.50</u>	<u>0.0035</u>
B×D×T	12	626.3250	52.1937	0.76	0.6902
<u>C×D×T</u>	<u>24</u>	<u>5291.0667</u>	<u>220.4611</u>	<u>3.21</u>	<u><.0001</u>
Error	98	6736.8667	68.7435	-	-
Total (Corrected)	239	484104.7333	-	-	-
Other Model Statistics					
Mean: 90.783			R ² : 0.986		
Coefficient of variation: 9.13%			Standard deviation: 8.29		

¹ Values <0.05 are considered significant in the analysis.

Note: The underlined three-factor interactions are significant. The lower order significant interactions were not considered in the analysis, because they are all contained in higher order interactions.

None of the factors involved in the significant three-factor interactions (A, B, C, D, and T) were clean since they were all contained in significant higher order interactions. The only clean two-factor interaction was B×D, which was not significant (p -value = 0.6421 > 0.05). So, the remaining two-factor interactions and main factors

were not further analyzed. Similar to the case of the storage modulus, the $A \times B \times C$ interaction was significant. This interaction, where all three factors were qualitative, was analyzed to reduce the total number of generated response surfaces. Likewise for the case of the storage modulus data, all the other significant three-factor interactions involved the quantitative factors, i.e., VGCNF weight fraction and temperature, which were considered in the response surfaces. As a result, LSD multiple comparisons were conducted on the mean data for the $A \times B \times C$ combinations to identify the significant ones. These are shown in Table 4.7, where each VGCNF type/dispersing agent/mixing method combination can be compared with the other combinations. For the interpretation of Table 4.7, see section 4.2.1. The letters in the t -grouping column are arbitrary.

Table 4.7 Multiple comparison results for the mean loss modulus data using least significant differences (LSD) for the interaction between the VGCNF type, use of dispersing agent, and mixing method (A×B×C).

<i>t</i> -grouping	Least squares means for the loss modulus data	VGCNF type (A)	Use of dispersing agent (B)	Mixing method (C)
W ¹	102.15	Oxidized	No	US ²
W				
W	100.95	Pristine	Yes	US
W				
W	97.75	Pristine	No	US
W				
W	97.45	Oxidized	Yes	US
X	89.45	Oxidized	No	HS ³ /US
X				
Y X	89.05	Pristine	No	HS
Y X				
Y X	88.60	Oxidized	Yes	HS/US
Y X				
Y X	87.60	Pristine	Yes	HS/US
Y X				
Y X	86.50	Pristine	Yes	HS
Y X				
Y X	85.80	Oxidized	Yes	HS
Y				
Y Z	84.20	Pristine	No	HS/US
Z				
Z	79.90	Oxidized	No	HS

¹ Least squares means with the same letters are not significantly different from each other.

² Ultrasonication

³ High-shear mixing

All combinations involving ultrasonication alone gave the highest mean loss modulus, which were not significantly different from each other (the first four combinations in Table 4.7). The last eight high-shear mixing and coupled high-shear mixing/ultrasonication combinations are chained in the *t*-grouping column. Thus, all 12 combinations can be grouped into two sets of mean loss modulus data, one for specimens prepared using ultrasonication (US) and another one for specimens prepared using high-

shear mixing (HS) or high-shear mixing/ultrasonication (HS/US), for the purpose of response surface modeling.

Cubic equations were fitted to the mean loss modulus data (see Equation 4.1), where VGCNF weight fraction (D) and temperature (T) were independent variables and the loss modulus (L) was the dependent variable. The insignificant model terms were removed through backward elimination. The lower order terms related to significant higher order terms were retained in the models according to the hierarchy principle (Kleinbaum & Klein, 2010) similar to the storage modulus. The regression analysis results are given in Table 4.8. In this table, parameters with p -values of less than $\alpha = 0.05$ are considered significant model terms.

Table 4.8 Regression analysis for the loss modulus data.

Parameter	Degrees of Freedom	Parameter Estimate	Standard Error	<i>t</i> -value	<i>p</i> -value
High-shear mixing or coupled high-shear mixing/ultrasonication ($R^2 = 0.944$, adjusted $R^2 = 0.941$):					
β_0	1	11.8169643	17.07323999	0.69	0.4899
β_1	1	-73.1982143	25.88403207	-2.83	0.0053
β_2	1	2.6975020	0.80782788	3.34	0.0011
β_{11}	1	118.2857143	21.48009308	5.51	<.0001
β_{12}	1	-0.5819881	0.51111957	-1.14	0.2567
β_{22}	1	-0.0432569	0.01152875	-3.75	0.0002
β_{112}	1	-1.7680952	0.26144737	-6.76	<.0001
β_{122}	1	0.0200972	0.00288219	6.97	<.0001
β_{222}	1	0.0002373	0.00005063	4.69	<.0001
Ultrasonication ($R^2 = 0.913$, adjusted $R^2 = 0.903$):					
β_0	1	-49.3491071	24.35328825	-2.03	0.0465
β_1	1	220.1220238	36.18147778	6.08	<.0001
β_2	1	5.2688889	1.16253856	4.53	<.0001
β_{11}	1	-435.6428571	75.78024271	-5.75	<.0001
β_{12}	1	-1.4433333	0.63255365	-2.28	0.0255
β_{22}	1	-0.0717222	0.01660452	-4.32	<.0001
β_{111}	1	248.3333333	49.81355132	4.99	<.0001
β_{122}	1	0.0138889	0.00415113	3.35	0.0013
β_{222}	1	0.0003272	0.00007293	4.49	<.0001

Note: The significant model parameters are different for each of the three combinations.

The final response surface models for the loss moduli can be expressed as:

$$L_{HS \text{ or } HS/US} = 11.8 - 73.2D + 2.7T + 118.3D^2 - 0.6DT - 0.04T^2 - 1.8D^2T + 0.02DT^2 + 0.0002T^3 \quad (4.5)$$

$$L_{US} = -49.3 + 220.1D + 5.3T - 435.6D^2 - 1.4DT - 0.07T^2 + 248.3D^3 + 0.01DT^2 + 0.0003T^3 \quad (4.6)$$

where L is the storage modulus, D is the VGCNF weight fraction, and T is the temperature. The subscripts HS and US stand for high-shear mixing and ultrasonication,

respectively. These models describe 94.4% and 91.3% of the variations in the mean loss modulus data for HS or HS/US and US cases, respectively. These response surfaces are plotted in Figures 4.8 and 4.9. In contrast to the response surfaces developed for the mean storage modulus data, the interpretation of the response surfaces for the mean loss modulus data is difficult and therefore, 2D graphs are used.

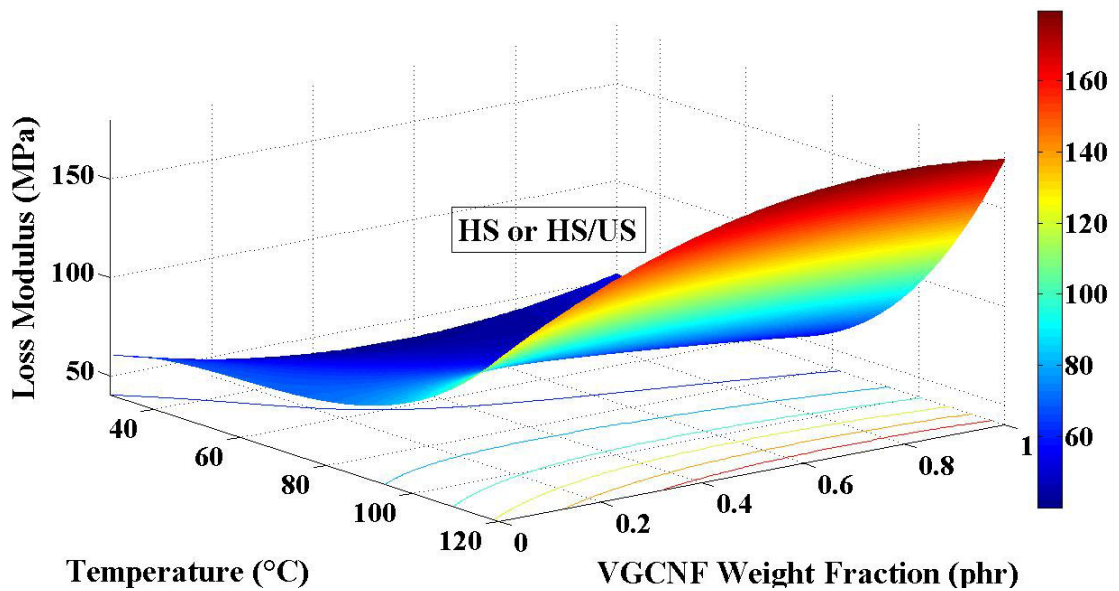


Figure 4.8 The predicted response surface and contour plots for the loss modulus as a function of VGCNF weight fraction and temperature for the case where either high-shear mixing (HS) or coupled high-shear mixing/ultrasonication (HS/US) is used.

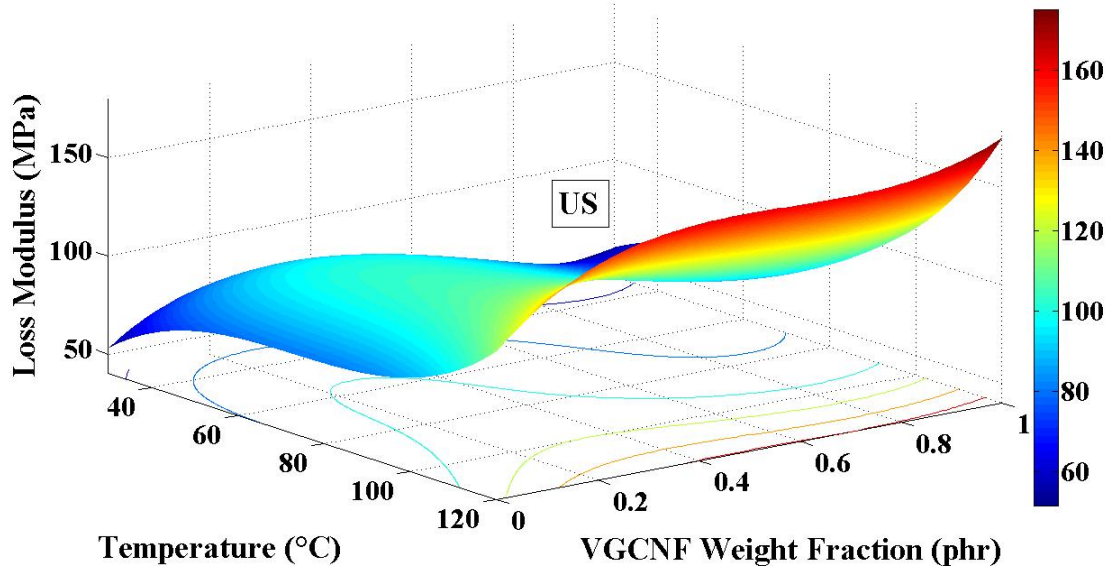


Figure 4.9 The predicted response surface and contour plots for the loss modulus as a function of VGCNF weight fraction and temperature for the case where ultrasonication (US) is used.

2D graphs were generated from the response surfaces (Equations 4.5 and 4.6) to clearly visualize the effects of VGCNF weight fraction, temperature, and the two mixing combinations (HS or HS/US and US) on the predicted nanocomposite loss moduli. In Figure 4.10, the effect of temperature on the predicted loss modulus for different mixing combinations (US and (HS or HS/US)) at fixed VGCNF weight fractions is shown. In the case of HS or HS/US combinations (Figure 4.10a), all VGCNF weight fractions yielded lower predicted loss moduli values compared to the neat VE at temperatures below ~80-90 °C. This is anticipated to be the result of better nanofiber dispersion in the VE matrix by utilizing high-shear mixing. Hence, fewer and smaller size agglomerates lead to lower energy dissipation. In general, the higher the VGCNF weight fraction is, the lower the predicted loss modulus will be. At higher temperatures, the predicted loss moduli for all

nanocomposites exceeded those of the neat VE. It is anticipated that at these high temperatures, the individual and agglomerated nanofibers contribute to the energy dissipation by providing a better heat distribution throughout the nanocomposite specimen. This, in turn, leads to a higher mobility of the crosslinked VE chain segments, and hence, higher energy dissipation is observed. A similar trend is observed for higher VGCNF weight fractions at temperatures above ~ 70 °C using ultrasonication (Figure 4.10b). Moderate to low VGCNF weight fractions yielded predicted loss moduli that were higher than those of the neat VE at all temperatures. Since ultrasonication yields poor nanofiber dispersion in the VE resin compared to high-shear mixing (see section 3.2.2), larger VGCNF agglomerates are present in the nanocomposites prepared using ultrasonication. VGCNFs tend to reduce the ductility of the VE matrix (see section 3.2.2). In contrast, VGCNF agglomerates may tend to dissipate energy through friction between the entangled nanofibers that are loosely held together by the infused cured resin. Therefore, larger agglomerates and subsequently more energy dissipation is the outcome for specimens prepared using ultrasonication, especially at lower VGCNF weight fractions.

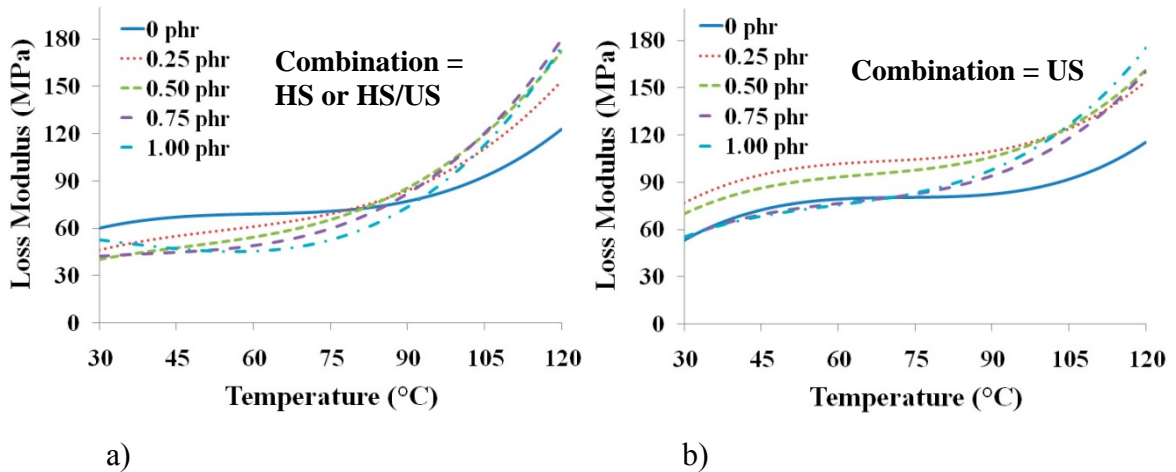


Figure 4.10 Predicted loss modulus as a function of temperature for different VGCNF weight fractions for two cases: a) high-shear mixing (HS) or high-shear mixing/ultrasonication (HS/US) and b) ultrasonication (US).

In Figure 4.11, the predicted loss moduli are plotted as functions of VGCNF weight fraction for different temperatures and mixing combinations. The shapes of the curves changed dramatically for the HS or HS/US case (Figure 4.11a) as the temperature increased, while they remained almost the same for the case of ultrasonication (Figure 4.11b). With adequate VGCNF dispersion in the VE matrix, the use of nanofibers results in reduced nanocomposite ductility. However, this effect is most noticeable at low temperatures and VGCNF weight fractions ($< \sim 0.6$ phr for 30 °C plot) for HS or HS/US mixing combinations (Figure 4.11a). When the temperature is increased, this effect is slowly reversed and the nanocomposite starts to dissipate more energy, which is clearly evident at 120 °C.

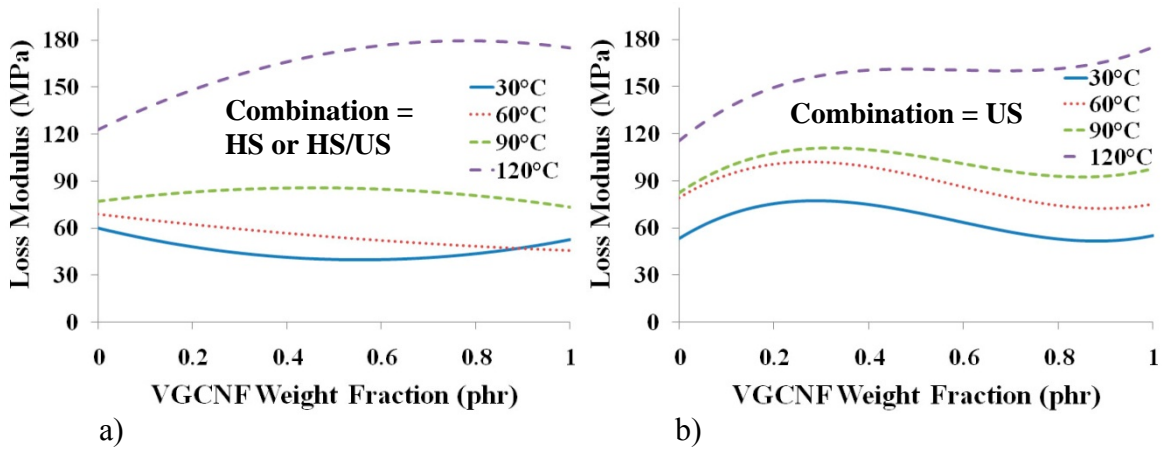


Figure 4.11 Predicted loss modulus as a function of VGCNF weight fraction for different temperatures for two cases: a) high-shear mixing (HS) or high-shear mixing/ultrasonication (HS/US) and b) ultrasonication (US).

The predicted loss moduli are compared for HS or HS/US and US combinations and for different VGCNF weight fractions ($D = 0.25, 0.50, 0.74,$ and 1.00 phr) as functions of temperature in Figure 4.12. As the VGCNF weight fraction increased, specimens prepared using both mixing combinations (HS or HS/US and US) showed a slightly decreased loss modulus. However, for most VGCNF weight fractions, the specimens prepared using ultrasonication alone showed higher loss moduli over the entire temperature range. The plots almost merge for both mixing combinations at higher temperatures, indicating that energy dissipation is primarily matrix-dominated at these temperatures.

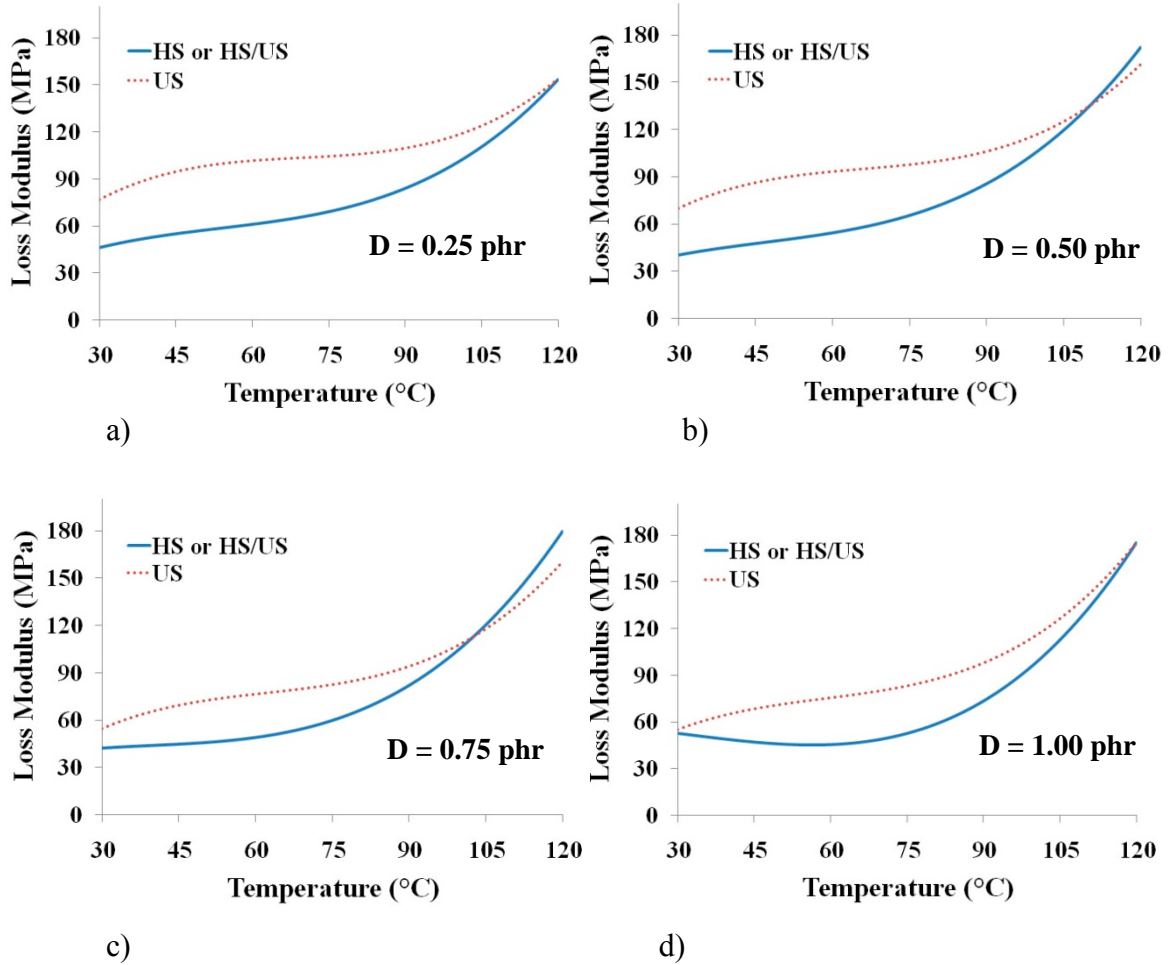


Figure 4.12 Comparisons between predicted loss modulus for high-shear mixing (HS) or high-shear mixing/ultrasonication (HS/US) and ultrasonication (US) for VGCNF weight fractions (D) of a) 0.25 phr, b) 0.50 phr, c) 0.75 phr, and d) 1.00 phr.

In Figure 4.13, the predicted loss moduli are plotted as functions of VGCNF weight fraction for different mixing combinations at different temperatures ($T = 30, 60, 90,$ and 120 °C). As expected, specimens prepared using the US combinations alone yielded higher loss moduli than the specimens prepared using HS or HS/US combinations at low to moderate temperatures. However, at high temperatures, the specimens prepared using both mixing combinations showed similar behavior. This, again, shows that at high

temperatures, the energy dissipation is dominated by the matrix and is independent of the mixing method utilized for dispersing the nanofiber in the matrix.

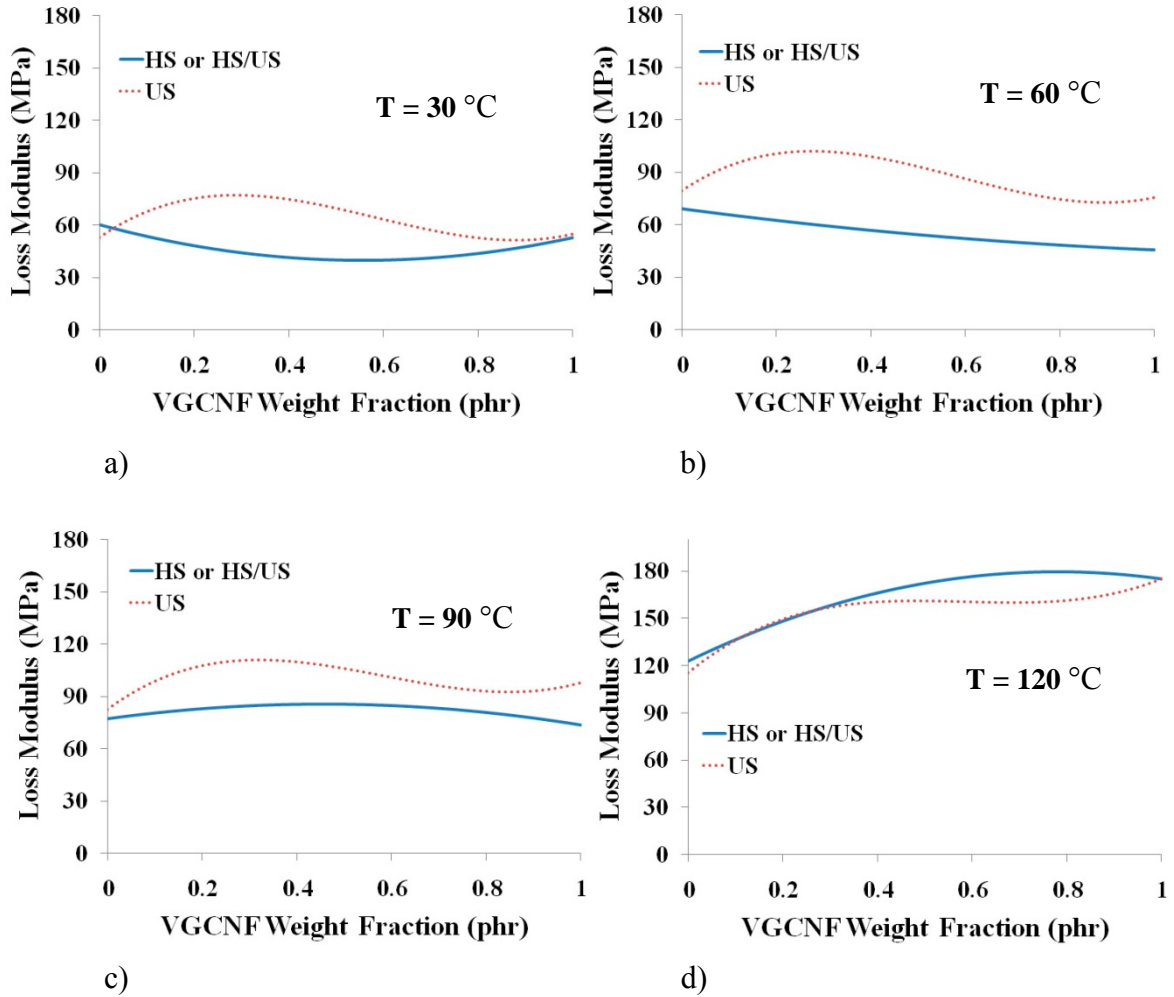


Figure 4.13 Comparisons between predicted loss modulus for high-shear mixing (HS) or high-shear mixing/ultrasonication (HS/US) and ultrasonication (US) for temperatures (T) of a) 30 °C, b) 60 °C, c) 90 °C, and d) 120 °C.

4.2.3. Nanocomposite Optimization

The response surface models for the storage and loss moduli developed in this chapter provide a statistically validated tool for predicting the viscoelastic properties of VGCNF/VE nanocomposites over a wide temperature range. The response behavior of these materials is quite complex. However, general recommendations can be given about the choice of factor levels that would fulfill certain engineering goals. For example, higher storage modulus (stiffness) is typically desired for structural applications. Therefore, based on the analyses in section 4.2.1, high-shear mixing should be utilized in nanocomposite preparation. This saves both time and money as compared to the high-shear mixing/ultrasonication combination, which gave similar predicted storage moduli. Furthermore, the use of either oxidized VGCNFs in the absence of dispersing agent, or pristine VGCNFs in the presence of dispersing agent is recommended. A VGCNF weight fraction of 0.50 phr is also preferred to maintain the highest storage modulus over the entire temperature range (see Figures 4.5 and 4.6b). If a lower loss modulus is desired for the same temperature range, then the combination of oxidized VGCNFs with no dispersing agent is recommended (Table 4.7). But, if moderate energy dissipation is sought for the nanocomposite, then combination of pristine VGCNFs with dispersing agent is preferred (Table 4.7). The use of ultrasonication with ~0.25 phr VGCNF fulfills the goal of maximizing the loss modulus over the entire temperature range (see Figures 4.11b and 4.12a). However, the storage modulus will be lower than the high-shear mixing case. Again, such determinations may not be obvious when employing more traditional *ad hoc* or *one-at-a-time* experimental strategies (see section 2.5).

4.3. Conclusions

The designed experimental study in chapter 3 was extended to include the effect of temperature on the dynamic mechanical responses of VGCNF/VE nanocomposites. New response surface models were developed to predict storage and loss moduli as functions of five independent factors: 1) VGCNF type (A), 2) use of dispersing agent (B), 3) mixing method (C), 4) VGCNF weight fraction (D), and 5) temperature (T). Through ANOVA and subsequent LSD multiple comparisons, the predicted nanocomposite storage modulus was found to be primarily a function of three mixing combinations, i.e., high-shear mixing (or high-shear mixing/ultrasonication), ultrasonication with oxidized VGCNFs in the presence of dispersing agent, and ultrasonication with other VGCNF type/dispersing agent combinations over the entire temperature range (30-120 °C). A similar dependence was observed for the loss modulus except for the ultrasonication combinations, which all had the same effect on the loss modulus.

The response surface models were used to identify combinations of formulation and processing factors that lead to optimal predicted nanocomposite viscoelastic properties over the entire temperature range of study. For example, the use of high-shear mixing, oxidized VGCNFs without dispersing agent or pristine VGCNFs with dispersing agent, and a VGCNF weight fraction of 0.50 phr is recommended for maximizing the storage modulus at both low, moderate, and high temperatures. The response surface models developed in this chapter may be used to tailor the viscoelastic properties of VGCNF/VE nanocomposites for use in structural applications where the structural component may be exposed to variations in temperature.

CHAPTER 5
MOLECULAR DYNAMICS SIMULATIONS OF VINYL ESTER RESIN
MONOMER INTERACTIONS WITH A PRISTINE VAPOR-GROWN
CARBON NANOFIBER AND THEIR IMPLICATIONS
FOR COMPOSITE INTERPHASE FORMATION

The formation and characteristics of an interphase in VGCNF/VE nanocomposites and mechanisms leading to its creation are not understood and have never been studied using MD simulation. However, the interphase formation in both “unsized” and “sized” long carbon fibers with oxidized surface functions (AS4 fibers) in VE resins has been experimentally studied by Xu (2003). In this study, diffusion of styrene into lightly crosslinked carbon fiber sizing was proposed, resulting in a smoother gradient at the interphase compared to pure bisphenol A epoxy-based VE resin. The interactions between liquid monomers of thermosetting resins, such as VE, and VGCNF surfaces, prior to crosslinking, could lead to different mole ratios of these monomers in the interface region compared to those in the bulk resin. After curing, the resulting crosslinked network may therefore have a different crosslink structure in the interphase region. Hence, gradients in mechanical properties may develop (Schadler et al., 2007).

The present work provides an improved understanding of the VE liquid resin monomer interactions (prior to curing) with a pristine VGCNF during processing of

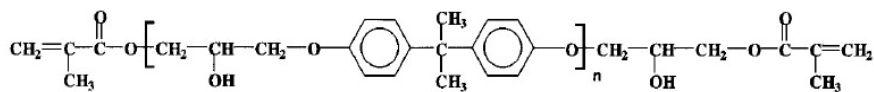
VGCNF/VE nanocomposites. The MD simulations were conducted on a VGCNF/VE nanocomposite comprised of a VE resin corresponding to resin monomer mole ratios giving 33 wt% styrene and the remaining 67 wt% split between two VE monomers. This work is a collaborative effort with Changwoon Jang. The computations were performed by Jang at the Center for Advanced Vehicular Systems (CAVS) of Mississippi State University. The unique feature of this work is the simulation of a relatively large system containing 17,055 atoms with a large number of time steps (total simulation time of ~13 ns). The concentrations of the three monomers in the proximity of idealized nanofiber surfaces, after equilibration had occurred, differed from those in the bulk resin. This suggests that the creation of an interphase region during resin crosslinking could occur.

5.1. Molecular Models

5.1.1. Models of Vinyl Ester Monomers

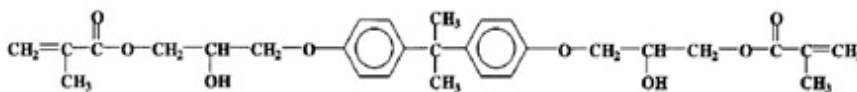
The vinyl ester resin used in the simulation was the same commercial grade (Derakane 441-400) used for the experimental studies in Chapters 3 and 4. It is a mixture of VE dimethacrylates with an average molecular weight of 690 g/mol (Li, 1998) and also contains 33 wt% styrene. Derakane 441-400 has an average of 1.62 bisphenol A groups ($n = 1.62$, where n is the number of bisphenol A groups) in the dimethacrylate backbone (Li, 1998). Figure 5.1 shows the general chemical formula of the two VE dimethacrylate molecules that were employed in the simulations and the molecular

models created for $n = 1$ and $n = 2$. For simplicity, these two dimethacrylate monomers are designated VE1 and VE2 corresponding to $n = 1$ and $n = 2$, respectively.

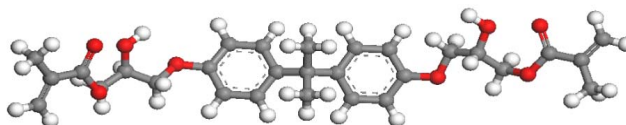


General VE formula

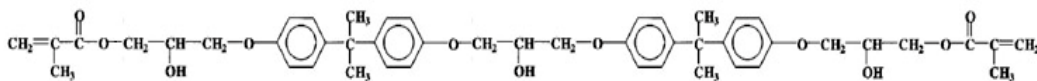
a)



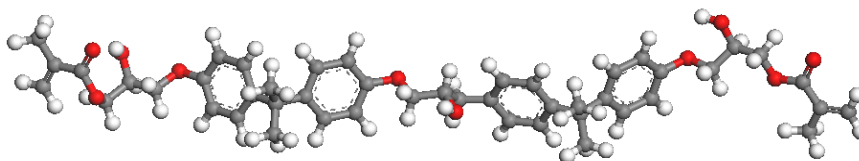
VE1



b)



VE2



c)

Figure 5.1 Bisphenol A-based dimethacrylate monomers of the vinyl ester resin: a) General formula ($n = 1.62$ for Derakane 441-400). b) Chemical formula and model created for $n = 1$. c) Chemical formula and model created for $n = 2$.

A mixture of VE1 and VE2 was used in the simulations at a VE1/VE2 mole ratio of 37/61. This corresponds to the average value of $n = 1.62$ present in Derakane 441-400. The chemical formula and model for styrene are shown in Figure 5.2.

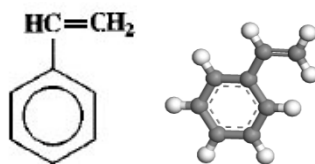


Figure 5.2 Chemical structure and the model created for styrene.

5.1.2. Model of the Carbon Nanofiber Surface

VGCNFs typically have a stacked-cone (Dixie cup) structure (Figures 5.3a and 5.3b) (Maruyama & Alam, 2002). In this work, the surface of a VGCNF was idealized using two overlapping flat graphene sheets stacked on top of each other in a shingled form to resemble the overlapping region of stacked nanocones along the outer surface of a VGCNF. This structure is shown in Figure 5.3c. The nanocone structure used previously by Gou et al. (2007) was avoided because it employed an artificially small radius leading to a highly curved π -electron structure. This would distort its interaction with the three monomers. The VGCNF diameters range from 70 to 200 nm (700-2000 Å), which are large in comparison with typical MD simulation cell dimensions (~125-350 nm³). The simulation cell used in this work was 60×50×60 Å³ (180 nm³) in size. Hence, the surface of a VGCNF, which appears essentially flat at the scale of a styrene or vinyl ester molecule, can be approximated using graphene sheets. This is clearly illustrated in Figure 5.3c for a 6 nm wide section on a nanofiber cone's surface.

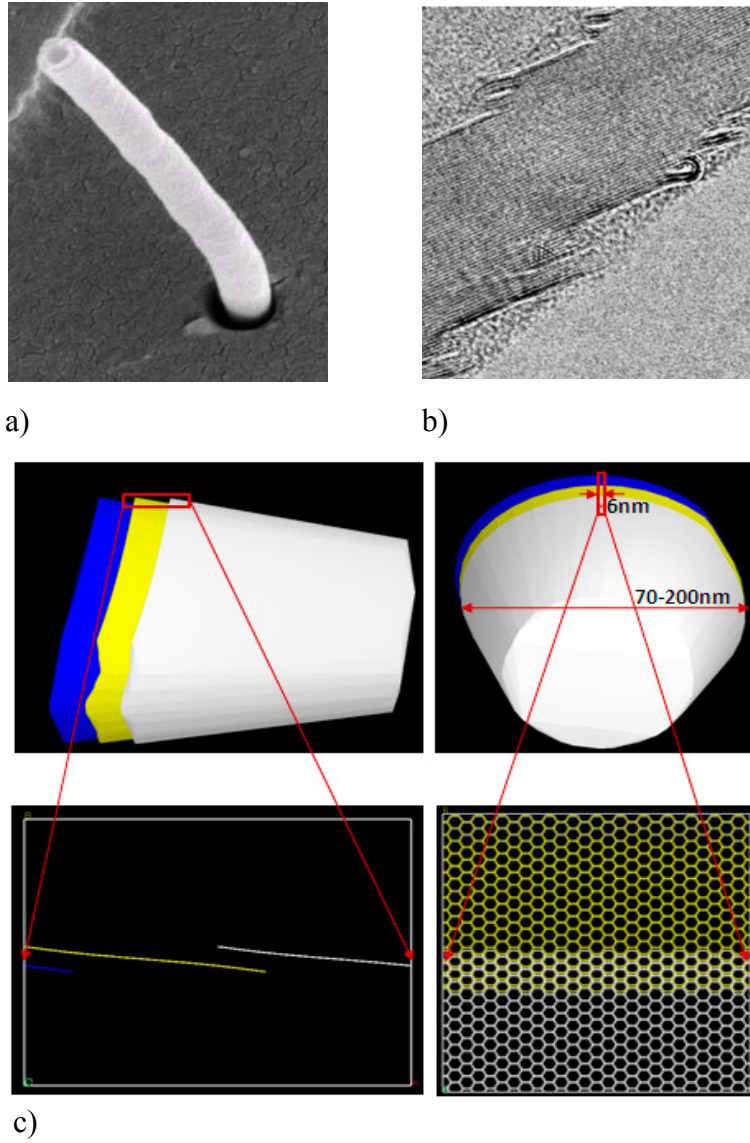


Figure 5.3 a) View of a single carbon nanofiber. b) Cross section of the stacked nanocone structure of VGCF with shingled graphene sheets (adapted from (Uchida et al., 2006)). c) A schematic of overlapping graphene sheets along the outer edge of VGCF stacked nanocones (courtesy of Changwoon Jang).

5.2. MD Simulation Details

5.2.1. The MD Simulation Cell

All simulations were performed using Accelrys® Materials Studio® V5.0 software (Accelrys, 2011). A cell of size $60 \times 50 \times 60 \text{ \AA}^3$ was created and two parallel graphene sheets were stacked in the middle of the simulation cell to form a shingle. Shingling is necessary if the stacked-cone VGCNF morphology is to be simulated. The distance between the cone edges (represented as the edge plane where the overlap takes place) varies somewhat in real VGCNFs based on high-resolution transmission electron microscopy (TEM) studies (Uchida et al., 2006). The model employed in the present work represents the case where a cone edge is encountered once every 30 \AA along the nanofiber. This is an estimate from the TEM examinations (Uchida et al., 2006). Furthermore, the shingled structure better represents real VGCNFs because it exposes the liquid monomers to both edges and basal graphitic planes.

The sheets are roughly perpendicular to the y-direction or (0 1 0) plane and parallel to the x- (1 0 0) and z-directions (0 0 1) (Figure 5.4). 3D periodic boundary conditions were used. The sheets have an inter-planar spacing of 3.5 \AA , which is close to the value of 3.4 \AA reported by Zhu et al. (2005) for fishbone-type carbon nanofibers. The sheets have a slight angle relative to the basal (xz) plane of the cell to allow for a shingled graphene sheet structure to be constructed in the x-direction (Figure 5.4). The distance between the shingle steps is about 30 \AA . In a real carbon nanofiber, the typical distance between the shingle steps is about 10-20 nm (Uchida et al., 2006). To prevent distortion and separation of the graphene sheets and their inter-planar distances during dynamics

simulations, their atomic coordinates were fixed. This is justified because multiple layers of rigid stacked cones in real VGCNFs prevent graphene sheet distortions.

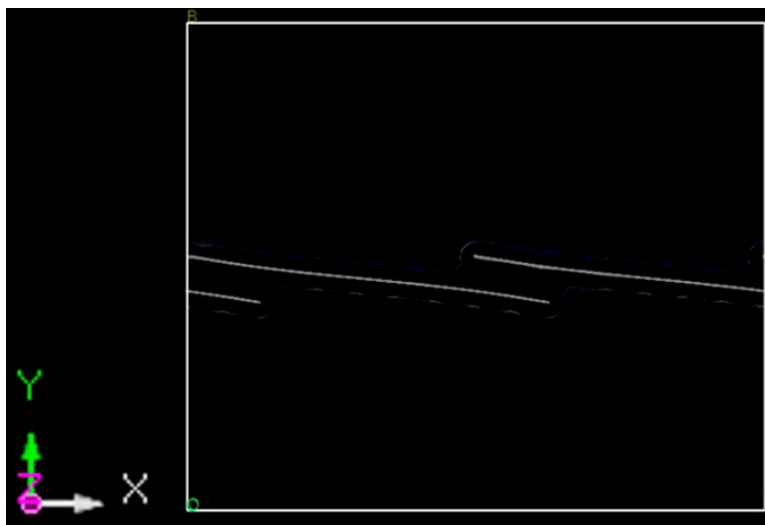


Figure 5.4 View of stacked (periodic) graphene sheets resembling the surface of carbon nanofiber.

VE resin monomers (VE1, VE2, and styrene) were initially randomly packed around the graphene sheets using the iso-surface feature in the Amorphous Cell® module of Materials Studio® to yield a final simulation cell density of 1.18 g/cm^3 (Figure 5.5). This density value was previously measured experimentally, as part of this study, for a cured VGCNF/VE composite with 1 wt % VGCNFs. The iso-surface was removed after monomer packing to permit monomer-nanofiber surface interactions. The total number of monomer molecules used and their weight fractions are given in Table 5.1.

Table 5.1 Total number and weight fractions of vinyl ester resin monomers.

Resin monomer ¹	Number of molecules	Mass (u)	Weight %
VE1 ²	37	512.599	18.8
VE2 ³	61	796.954	48.2
Styrene	320	104.152	33.0

¹ Vinyl ester resin (Derakane 441-400) with $n = 1.62$ (n is the number of bisphenol A groups in the dimethacrylate's backbone).

² The dimethacrylate with $n = 1$.

³ The dimethacrylate with $n = 2$.

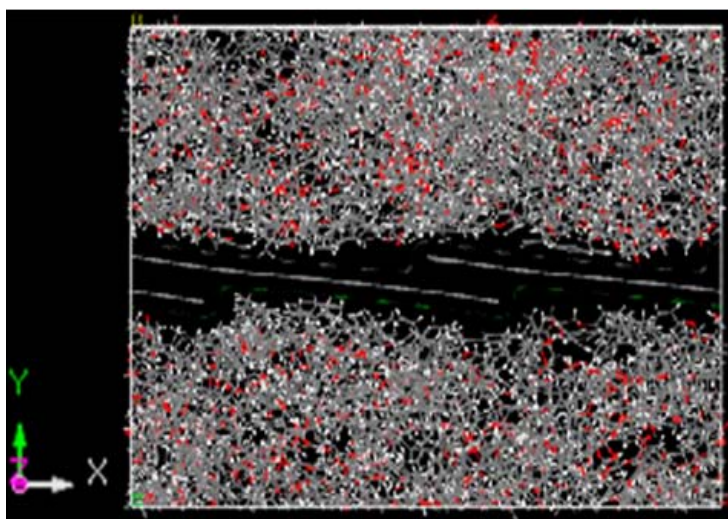


Figure 5.5 The periodic simulation cell packed with resin monomers.

5.2.2. Dynamics Simulations

The Condensed-Phase Optimized Molecular Potentials for Atomistic Simulation Studies (COMPASS) force field developed by Sun (1998) was used for this study. This force field is widely used for organic and inorganic systems. The total potential energy (E_{pot}) in this force field is defined as (Sun, 1998):

$$E_{pot} = E_{valence} + E_{nonbond} \quad (5.1)$$

$$E_{valence} = E_{diagonal} + E_{coupling} \quad (5.2)$$

$$E_{diagonal} = E_{bond} + E_{angle} + E_{torsion} + E_{out-of-plane} \quad (5.3)$$

$$E_{nonbond} = E_{elec} + E_{vdW} \quad (5.4)$$

where E_{bond} , E_{angle} , $E_{torsion}$, $E_{out-of-plane}$, E_{elec} , and E_{vdW} are the energies associated with bond stretching, angle bending, torsion, out-of-plane (inversion), electrostatic (Coulombic), and van der Waals interactions, respectively. $E_{coupling}$ refers to coupled (cross-term) energies, which are bond-bond, angle-angle, bond-angle, bond-torsion, angle-torsion, and angle-angle-torsion. The diagonal and coupling energies are defined by the following terms (Sun, 1998):

$$E_{bond} = \sum_b [k_2(b - b_0)^2 + k_3(b - b_0)^3 + k_4(b - b_0)^4] \quad (5.5)$$

$$E_{angle} = \sum_\theta [h_2(\theta - \theta_0)^2 + h_3(\theta - \theta_0)^3 + h_4(\theta - \theta_0)^4] \quad (5.6)$$

$$E_{torsion} = \sum_\varphi \left[\begin{array}{l} v_1[1 - \cos(\varphi - \varphi_1^0)] + v_2[1 - \cos(2\varphi - \varphi_2^0)] + \\ v_3[1 - \cos(3\varphi - \varphi_3^0)] \end{array} \right] \quad (5.7)$$

$$E_{out-of-plane} = \sum_\chi K_2 \chi^2 \quad (5.8)$$

$$E_{bond-bond} = \sum_b \sum_{b'} f_{bb'}(b - b_0)(b' - b'_0) \quad (5.9)$$

$$E_{angle-angle} = \sum_\theta \sum_{\theta'} f_{\theta\theta'}(\theta - \theta_0)(\theta' - \theta'_0) \quad (5.10)$$

$$E_{bond-angle} = \sum_b \sum_\theta f_{b\theta}(b - b_0)(\theta - \theta_0) \quad (5.11)$$

$$E_{bond-torsion} = \sum_b \sum_{\varphi} (b - b_0) [v_1 \cos \varphi + v_2 \cos 2\varphi + v_3 \cos 3\varphi] + \sum_{b'} \sum_{\varphi} (b' - b'_0) [v_1 \cos \varphi + v_2 \cos 2\varphi + v_3 \cos 3\varphi] \quad (5.12)$$

$$E_{angle-torsion} = \sum_{\theta} \sum_{\varphi} (\theta - \theta_0) [v_1 \cos \varphi + v_2 \cos 2\varphi + v_3 \cos 3\varphi] \quad (5.13)$$

$$E_{angle-angle-torsion} = \sum_{\theta} \sum_{\theta'} \sum_{\varphi} k_{\theta\theta'\varphi} (\theta - \theta_0) (\theta' - \theta'_0) \cos \varphi \quad (5.14)$$

where b is the bond distance, θ is the angle, φ is the dihedral angle, χ is the inversion angle, and k , K , h , v , and f are model parameters. The Coulombic interaction is given by (Sun, 1998):

$$E_{elec} = \sum_{i>j} \frac{q_i q_j}{\epsilon r_{ij}} \quad (5.15)$$

where q_i and q_j are atomic charges, ϵ is the proportionality constant, and r_{ij} is the interatomic distance. The van der Waals interaction between two atoms is described using the Lennard-Jones (LJ) potential as follows (Sun, 1998):

$$E_{vdW} = \sum_{i>j} \left[\frac{A_{ij}}{r_{ij}^9} - \frac{B_{ij}}{r_{ij}^6} \right] \quad (5.16)$$

where r_{ij} is the inter-atomic distance, and A_{ij} and B_{ij} are model parameters. In the COMPASS force field, an inverse 9th power is used for the repulsive part (first term in the equation) instead of more commonly used empirical inverse 12th power. There is no strong theoretical reason to prefer any one of these forms.

A geometry optimization was carried out for 10,000 iterations using the conjugate gradient method to partially relax the molecular structures and minimize the total energy of the system. Then the MD simulation was started using an NVT ensemble (constant number of atoms, N ; constant volume, V ; and constant temperature, T) at 10 K with a

time step of 0.5 fs. An NVT ensemble was selected here for technical reasons. Since position constraints were placed on the graphene sheets, the box scaling which occurs during constant pressure (NPT) simulations would have led to unrealistic distortions of the sheets.

The simulation was run for 1 ps at 10 K. Then the temperature was increased to 50 K and then further up to 600 K in increments of 50 K. At each intermediate temperature, the dynamics simulation was run for 1 ps, except at 300 K where it was run for 100 ps. At 600 K, the simulation was run for a total time of 4 ns with a time step of 0.5 fs.

Next, the temperature was increased to 1000 K using 50 K increments and 1 ps dynamics simulation runs at intermediate temperatures. The dynamics simulations were run to obtain equilibrium monomer distributions in the simulation cell. This was achieved through successive simulations at elevated temperatures. It was found that high simulation temperatures were required to reach equilibrium monomer distributions equilibrium within a reasonable simulation time. Since equilibrium was not achieved at 600 K, the temperature was further increased to 1000 K.

The system was then cooled to 300 K in two different ways: 1) 10 K decrements (designated as C1), and 2) 50 K decrements (C2), both with 1 ps dynamics simulation runs at intermediate temperatures. After cooling, the dynamics simulation was continued for 5 ns at 300 K to ensure system equilibration. A summary of the simulation parameters is given in Table 5.2. In Figure 5.6, two snapshots of the simulation are shown: one after the geometry optimization step and the other after running the simulation for a total simulation time of ~13 ns (following cooling procedure C1). Complete wetting of the

graphene surface by monomers at the end of the simulations can be seen in contrast to the initial randomly packed structure. The closest distance between atoms on opposite sides of the graphene sheets is $\sim 7 \text{ \AA}$ (Fig. 6). Since this distance is a bit shorter than the cut off distance for van der Waals interactions (9.5 \AA), some cross sheet interactions may occur between monomers near opposite surfaces of the sheets, which are unrealistic. Any potential effects of these interactions were neglected in this work.

Table 5.2 Summary of the molecular dynamics simulation parameters.

Total number of atoms	17055
Ensemble	NVT
Thermostat (temperature control)	Anderson
van der Waals (vdW) cutoff distance	9.5 \AA

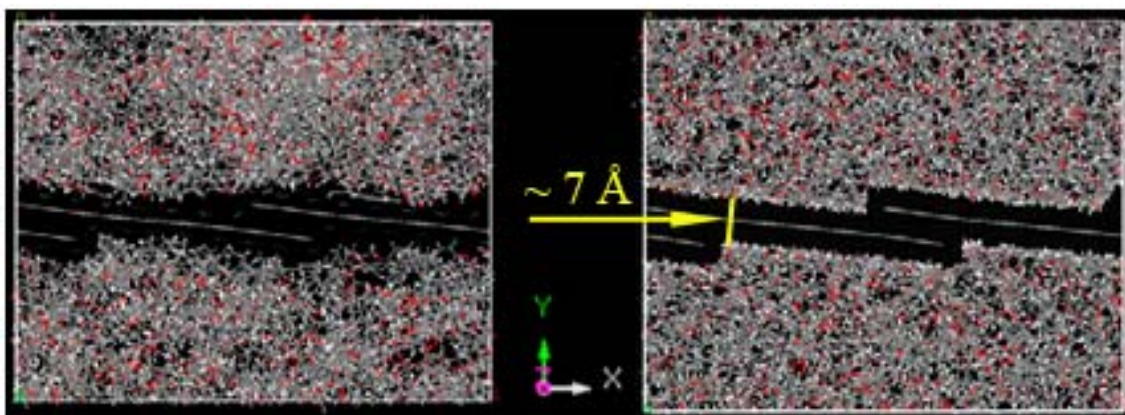


Figure 5.6 Snapshots of the initial frame after geometry optimization (left) and final frame after dynamics simulation (right) for a total simulation time of $\sim 13 \text{ ns}$ (following cooling procedure C1).

5.3. Results and Discussion

To analyze the distribution of liquid resin monomers at the nanofiber-resin interface and in the direction roughly perpendicular to the graphene sheets, concentration profiles were generated for different monomers in the y -direction (Figures 5.4 and 5.5), or perpendicular to the (0 1 0) plane, using the Forcite® analysis tool of Materials Studio®. The concentration profile is the relative concentration of a given monomer as a function of the distance from the origin of the simulation cell (here in the y -direction). It is generated for 3D periodic structures by determining the density of atoms or a set of atoms comprising a molecule within evenly spaced slabs (subvolumes) parallel to the axes of the simulation cell or any other direction of choice.

The dimensionless relative concentration (C) of a specific monomer's atoms contained in a given slab in the liquid resin is defined as:

$$C = \frac{N_{slab}}{V_{slab}} \cdot \frac{V_{tot}}{N_{tot}} \quad (5.17)$$

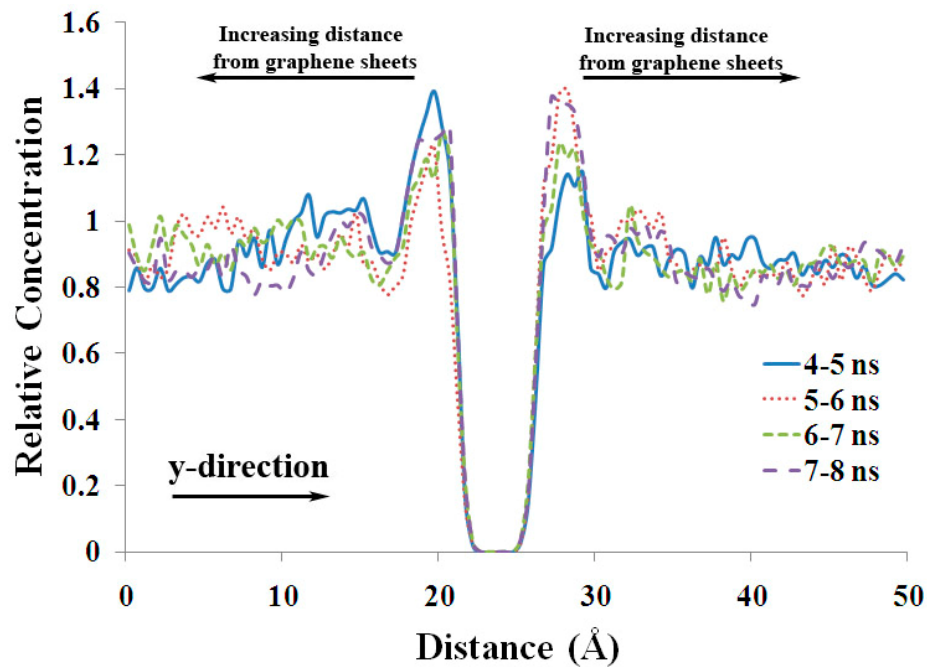
where N_{slab} is the number of monomer atoms in the slab, V_{slab} is the slab volume, N_{tot} is the total number of monomer atoms in the liquid resin, and V_{tot} is the total liquid resin volume in the simulation cell. A relative concentration of 1.0 within any liquid resin volume region of the cell (e.g., a slab) means that the ratio of the three monomers in that slab is the same as the average ratio throughout the liquid resin (e.g., the original mole ratio of the three monomers at the experimental density). A value of 2.0 indicates that twice the number of atoms from a specific monomer is in that slab compared to the case where all the monomers are distributed homogeneously across the liquid resin volume. In this study, the simulation cell was divided into 50 slabs (1 Å thick) parallel to the xz -

plane, and the monomer concentration profiles were generated for each of the three monomer molecules.

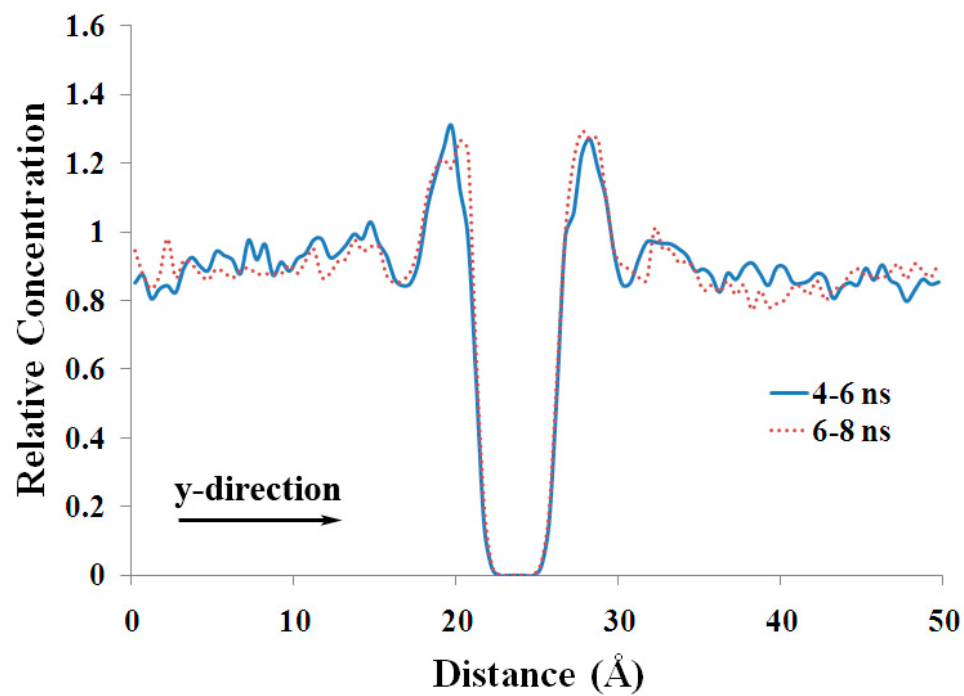
The interactions of each of these three resin monomers with the nanofiber surface and other neighboring monomers are different than the monomer-monomer interactions in regions removed from the surface. The initial randomly located monomers will try to reach a minimum energy, imparting a diffusion-controlled process, which moves towards equilibrium. The diffusion rate of the different monomers ultimately plays no role in the equilibrium distribution of the monomers within the simulation cell. It only determines how long the simulation will take to reach equilibrium. A state of equilibrium must be reached before post-processing of the acquired data. A definition of equilibrium in MD simulations should be established, since unfeasibly long simulation times may be needed to reach true equilibrium. The time-averaged monomer concentration profiles at 1000 K were used in this study as the basis for checking the equilibrium status of the system and determining when to start the cooling process. The relative monomer concentrations were determined every 50 ps and then time-averaged over each successive 1 and 2 ns intervals for the total simulation time of 4 ns performed at 1000 K.

Some time-averaged concentration profiles for styrene are shown in Figure 5.7. The domain, $22 \text{ \AA} < y < 25 \text{ \AA}$, denotes the vertical distance between the edges of the overlapping graphene sheets in the simulation cell, where the relative concentration goes to zero. Similar concentration profiles were generated for VE1 and VE2 and these are presented in the appendix C (Figures A.1 and A.2). The spatial and temporal evolutions of the concentration profiles were monitored, and the profiles were compared with each other to ensure that a suitable equilibrium had been reached before cooling the system to

300 K. Comparing the different time-averaged concentration profiles in Figure 5.7 reveals that there is consistency in the successive time-averaged profiles. Therefore, it was concluded that the system approached equilibrium at 1000 K after about 4 ns of simulation. So, a simulation time of 4 ns at 600 K and another 4 ns at 1000 K ensured that the monomers have equilibrated before cooling the system.



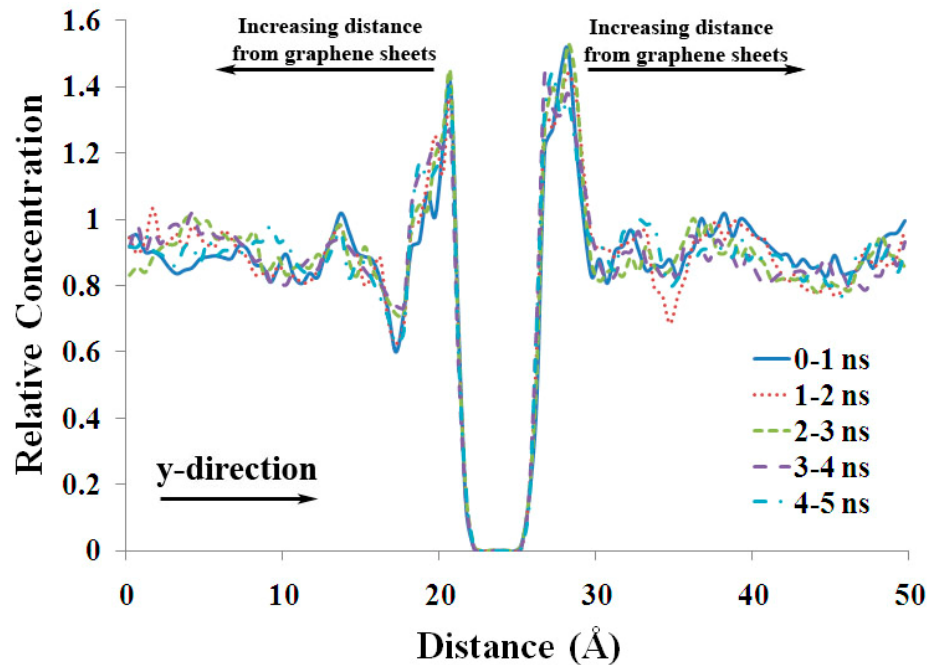
a)



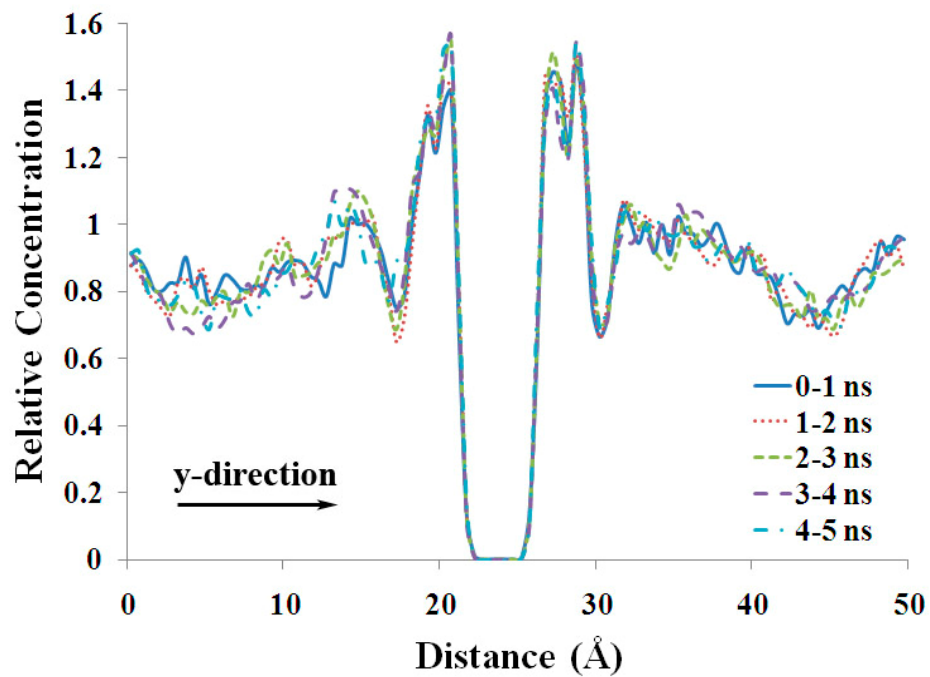
b)

Figure 5.7 Styrene concentration profiles, time-averaged over each successive 1 ns (a) and 2 ns (b) time intervals at 1000 K.

Upon cooling, the equilibrium of the system was verified. Two cooling procedures were followed to investigate the effect of cooling on the concentration profiles and the re-equilibration process. After the system was cooled to 300 K, the time-averaged concentration profiles for styrene were compared (Figure 5.8). Cooling was conducted by both C1 (10 K decrements) and C2 (50 K decrements) procedures, which were defined earlier. No major differences were observed between the two cooling procedures. The averages were calculated for both C1 and C2 over each 1 ns time interval within a total simulation time of 5 ns. The time-averaged concentration profiles closely matched each other, indicating that equilibrium had been reestablished at the lower temperature. The VE1 and VE2 concentration profiles for C1 and C2 cooling procedures are given in Appendix C (Figures A.3 and A.4).



a)



b)

Figure 5.8 Styrene concentration profiles, time-averaged over each successive 1 ns time interval at 300 K (total simulation time of 5 ns) for simulations following cooling procedures C1 (a) and C2 (b).

The monomer concentration profiles obtained through simulations following cooling procedures C1 and C2 were averaged over both simulations and over the total simulation time of 5 ns at 300 K to get a better estimate of the monomer distributions in the simulation cell. These simulation and time-averaged concentration profiles are shown in Figure 5.9.

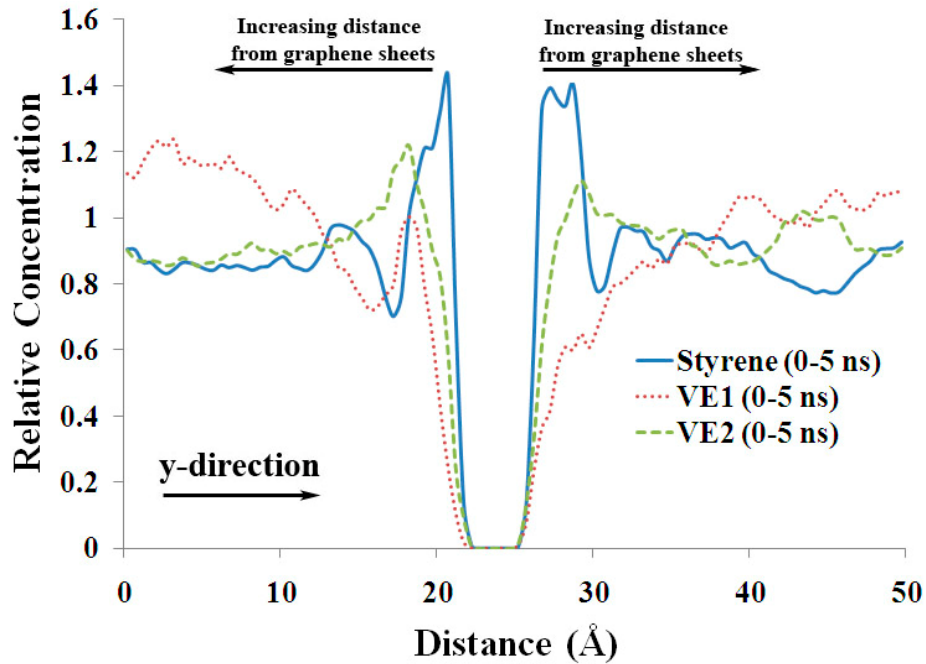
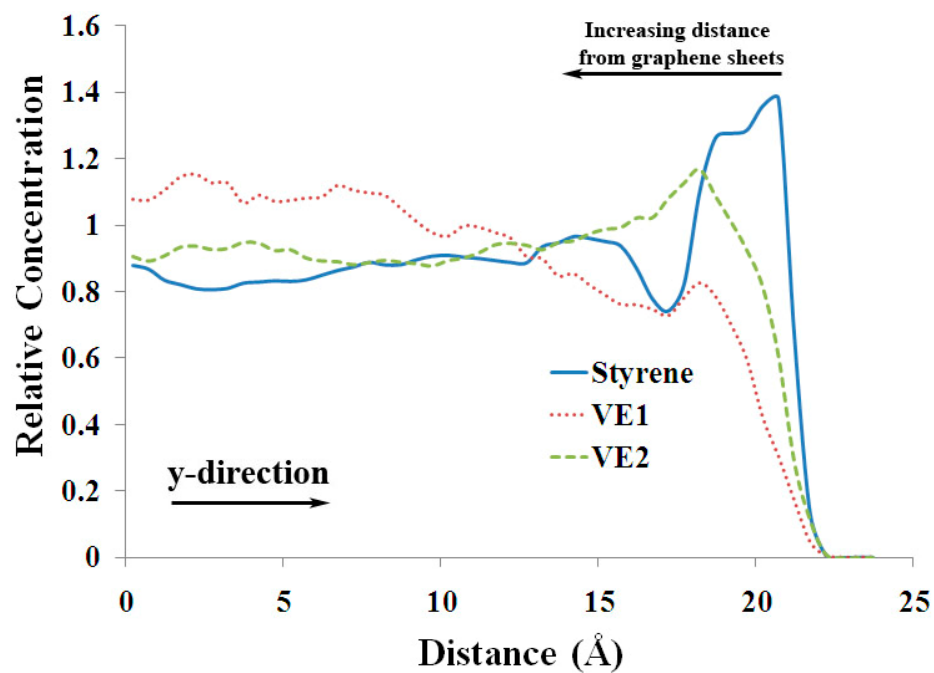


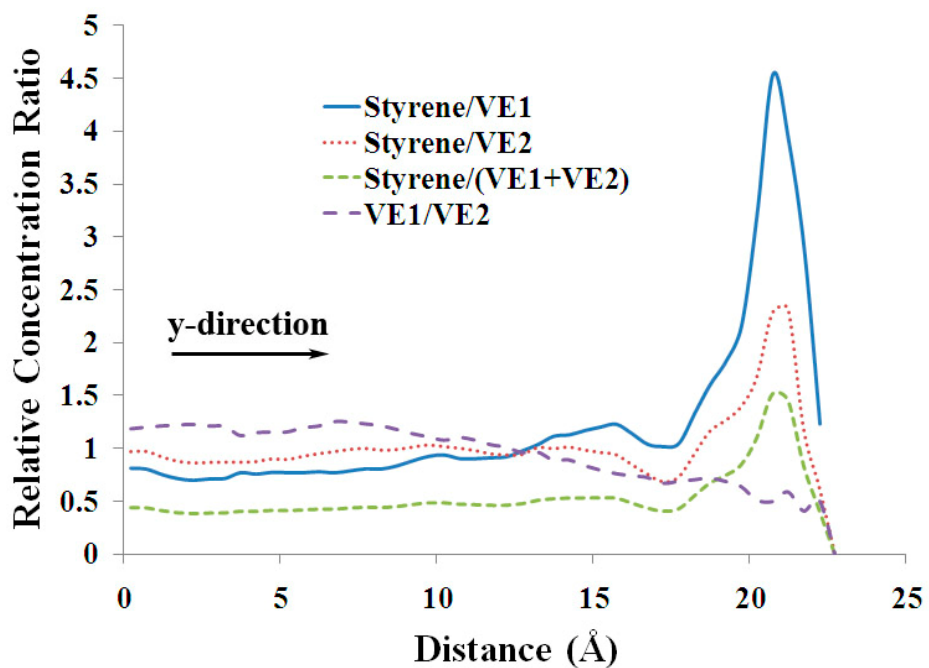
Figure 5.9 Concentration profiles of styrene, VE1, and VE2 averaged over the two simulations, which employed cooling procedures C1 and C2, respectively, and over 5 ns at 300 K for each simulation.

To obtain a more realistic estimate of the monomer distributions perpendicular to the nanofiber surface, the relative concentrations were averaged over both sides of the overlapping graphene sheets as shown in Figure 5.10. In a real VGCNF/VE composite, the resin monomers can only wet the *outer* nanofiber surface (here, one side of the

graphene sheet assembly). In the figure, the graphene sheets lie in the region corresponding to $y > 22 \text{ \AA}$. The surface relative concentrations of styrene and VE2 are higher than in the bulk resin, while the VE1 relative concentration adjacent to the surface is lower. It should be emphasized again that the effects of unrealistic cross-sheet interactions between monomers (as discussed in 3.2) would tend to be stronger between polar VE/VE than nonpolar styrene/styrene molecules. This would occur because the magnitude of polar interactions is inversely proportional to the third power of their separation distance, while nonpolar interactions decrease with the sixth power of separation distance. Thus, the relative concentration of styrene at the surface would likely be a little higher than what was observed here if these cross-sheet interactions had not existed. On this basis, our predicted enhancement of the relative styrene concentration at the nanofiber surface is a conservative value.



a)



b)

Figure 5.10 Concentration profiles of styrene, VE1, and VE2 (a) and monomer relative concentration ratios (b), where simulations were averaged after following cooling procedures C1 and C2 over the total simulation times of 5 ns at 300 K for each procedure (results are averaged over both sides of the graphene sheets).

The final simulated monomer distributions represent the amount of each monomer at each plane roughly parallel to the nanofiber surface. This is better depicted by calculating the relative monomer concentration ratios (equivalent to relative mole ratios) available versus distance from the nanofiber surface (Figure 5.10b). It is clearly evident in Figure 5.10b that the styrene/VE1 relative concentration ratio starts to increase about 10 Å away from the graphene surface and reaches a peak relative concentration ratio that is 4.5 times that of the bulk value near the surface.

The styrene/VE2 relative concentration ratio shows a peak of 2.5 near the surface (Figure 5.10). Thus, the relative concentration ratio of styrene to the sum of both VE monomers is higher near the nanofiber surface, while the VE1/VE2 ratio is a relative minimum. These simulations predict that styrene migration will occur, producing a higher styrene concentration within an approximately 5 Å thick region adjacent to the nanofiber surface. The near-surface concentration of VE1 decreases significantly, while that of VE2 is less depleted. The interaction of styrene molecules with the graphene surface plus the remaining surrounding molecules is more favorable than the interactions of styrene with surrounding molecules in the original bulk liquid resin.

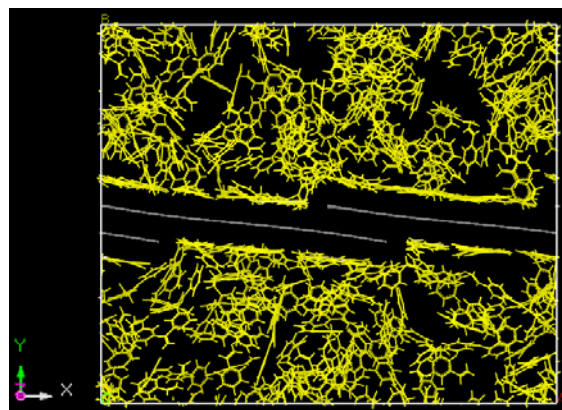
The major changes in the relative monomer concentration ratios occur in the 5 Å thick region surrounding the graphene sheets extending further out to about 10 Å. This may have significant consequences for composites made by curing a VE resin with dispersed nanofibers. If the VE matrix produced by free radical-initiated curing incorporates the monomers in their relative concentration ratios found in the 5-10 Å liquid region adjacent to the graphene surfaces prior to curing, the resulting matrix in that region will differ substantially from that of the bulk matrix structure. The resulting matrix

would then contain more styrene at the nanofiber/matrix surface, with a corresponding increase in the distance between the crosslinks. The local increase in the VE2/VE1 ratio near the interface would also increase the distance between the crosslinks. Both effects would generate a thin interphase region with low modulus. If this region averaged 10 Å or even 20 Å (e.g., 1 or 2 nm), it would be small relative typical VGCF diameters (70-200 nm). Thus, it would represent a small volume fraction and the mechanical properties of this region would likely have a negligible effect on the composite homogenized elastic moduli. However, since styrene seems to interact favorably with the graphene surface, a thin soft matrix layer near the surface might exhibit a higher interfacial shear strength than a more highly crosslinked matrix region with a smaller styrene content.

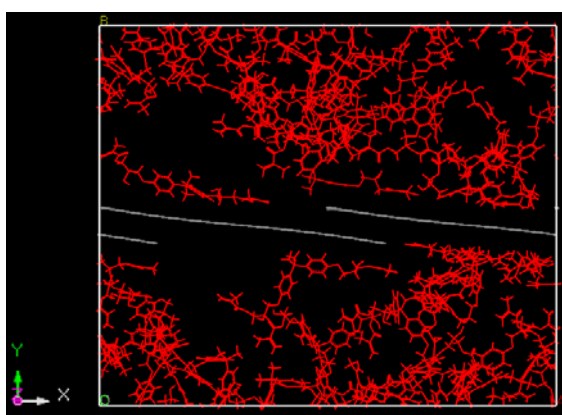
The size of the computational repeating cell used will lead to an underestimation of the styrene concentration adjacent to the graphene surface. This occurs because, as styrene migrates towards the surface, its bulk concentration decreases within the unit cell, with a compensating increase in the bulk concentration of VE2 and especially VE1. In a real composite, the volume of the bulk liquid resin relative to the volume near the nanofiber surface is far larger than that represented in these simulations. Thus, in real composites, the bulk concentration of styrene will be essentially unchanged after equilibrium is reached. Therefore, the driving forces for the migration of styrene away from the surface during equilibration will be smaller than those represented here.

Also, on this basis, the simulation should give a conservative estimate of the styrene build-up in the volume very close to the nanofiber surface. The relative monomer distributions at the end of the simulation are shown in Figure 5.11. These snapshots were

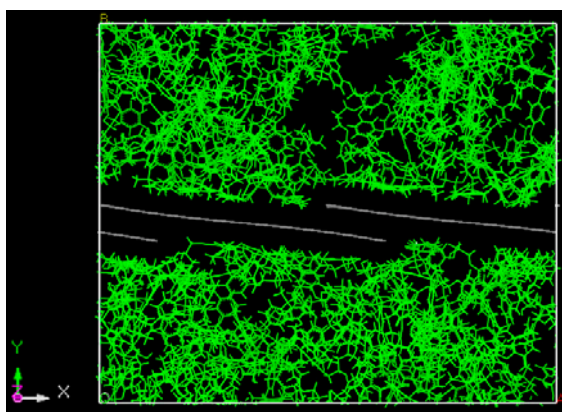
obtained following the cooling procedure C2 (50 K decrement steps) at a total simulation time of ~13 ns and are at a temperature of 300 K.



a)



b)



c)

Figure 5.11 The distribution and arrangement of styrene molecules (a), VE1 molecules (b), and VE2 molecules (c) around the graphene sheets.

The phenyl rings of the styrene strongly align at the interface, parallel to the faces of the graphene sheets (Figure 5.11a). This optimizes π - π stacking and lowers the total energy. This interaction appears more favorable than the interactions of styrene with other monomers in the liquid resin and is a driving force for the build-up of the styrene-rich layer on the nanofiber surface. VE2 molecules are very large and extend over long distances in the simulation cell. A VE2 molecule has four aromatic rings versus only two for VE1. These rings are bonded to the tetrahedral $-\text{C}(\text{CH}_3)_2-$ function, which sterically hinders their ability to lay flat against the graphene sheets (Figure 5.11c). Thus, each ring can only achieve a portion of the π - π stacking interaction that styrene achieves. However, with four aromatic rings in its structure, each VE2 molecule can achieve a larger favorable interaction with graphene surfaces. Apparently, this results in higher VE2 versus VE1 concentration near the surface. Of course, these explanations are tentative because the sum of all the interactions of each type of monomer in the bulk must be compared to the sum of all the interactions of each type of monomer at or near the nanofiber surface.

5.4. Conclusions

MD simulations were performed to study the interactions between VE resin monomers (bisphenol A-glycidyl dimethacrylates) and styrene with the surface of a pristine VGCNF. The monomer concentration profiles were determined at equilibrium to investigate the monomer distributions versus the distance from the nanofiber surface. The styrene/VE monomer ratios were found to be substantially higher within 5 Å of the nanofiber-resin surface compared to their bulk ratios. These modified monomer relative

concentration ratios near the nanofiber surface may result in a thin (5-10 Å thick) interphase region of a few molecular layers if they are retained within the matrix structure during curing. The accumulation of styrene in the immediate vicinity of the nanofiber surface and the increased VE2/VE1 ratio is anticipated to yield a locally more compliant matrix with a lower crosslink density.

The pronounced accumulation of styrene, with its phenyl rings lying parallel to the graphene sheets due to π - π stacking interactions, suggests that a lightly crosslinked interphase with a large number of styrene-graphene interactions could result in improved nanofiber-matrix interfacial shear strengths compared to a more highly crosslinked matrix with bulk monomer composition. This study is one of the few investigations of liquid monomer-nanofiber interactions that directly address the interphase formation in VE matrix nanocomposites.

CHAPTER 6

CONCLUSIONS AND RECOMMENDATIONS FOR FUTURE WORK

VGCNFs are increasingly being used for the nano-enhancement of thermoplastic and thermoset polymers. A variety of improvements have been reported for the host polymer's thermal, electrical, mechanical, and other properties. The present research effort focused on both fundamental and engineering aspects of thermosetting VE resins reinforced with VGCNFs. These thermoset nanocomposites are of great interest for the automotive structural applications because they combine the benefits of low cost with good mechanical properties. Since a comprehensive understanding of the formulation and processing factors affecting viscoelastic properties of VGCNF/VE nanocomposites did not exist previously, the current dissertation attempted to fill this gap by providing a robust statistical analysis of major design factors for the achievement of optimal VGCNF/VE nanocomposite viscoelastic properties. Through design of experiments, the effects of design factors comprised of the VGCNF type (pristine, oxidized), the use of dispersing agent (no, yes), the mixing method (ultrasonication, high-shear mixing, and combination of both), the VGCNF weight fraction (0, 0.25, 0.50, 0.75, and 1.00 phr) were studied. In a separate analysis, these four factors along with the temperature (30, 60, 90, and 120 °C) were investigated to determine their effects on the nanocomposites' storage and loss moduli. As measures of stiffness and energy dissipation of the material, these properties are of key interest in the automotive applications. Empirical response

surface models were developed for the prediction of the viscoelastic properties as a function of significant design factors. Optimal conditions were then determined based on desired goals for both room (service) temperature and over a range encompassing room temperature to the material's glass transition temperature (T_g).

A fundamental aspect of thermoset nanocomposites was addressed in this work, for the first time, using molecular dynamics simulations. The interphase in a nanocomposite plays a major role in the reinforcement characteristics of the material since nanoreinforcements possess large surface area-to-volume ratios. Hence, the interphase volume fraction may be significant. The nature of the interphase in thermoset nanocomposites and the parameters affecting its formation and physical/mechanical properties have been previously unknown for nanocomposites such as VGCNF/VE. A novel methodology was introduced to predict the interphase formation in cured nanocomposites based on pre-curing resin (VE) interactions with the nanoreinforcements (VGCNFs) in the pre-crosslinking stage of nanocomposite fabrication. Through MD simulations, equilibrium monomer concentration profiles were established over the entire simulation cell in a direction roughly parallel to the nanoreinforcement surface, whereby regions of high and low monomer concentration were identified. The results and conclusions of this study are summarized below:

- 1) At room temperature (27 °C), the predicted VGCNF/VE nanocomposite storage moduli were a function of both VGCNF type and VGCNF weight fraction. The mixing method and the use of a dispersing agent did not significantly affect the mean storage modulus. The use of pristine VGCNFs at a VGCNF weight fraction of 0.37 phr, dispersing agent, and high-shear mixing were recommended to

maximize the storage modulus. Even though the use of a dispersing agent did not have a significant effect on the storage modulus, its use is highly recommended since it significantly reduces the VGCNF/VE blend viscosity. High-shear mixing is also recommended because of ease of industrial scale-up, lower cost (compared to ultrasonication), and greater flexibility. The nanofiber weight fraction, the mixing method, and the use of dispersing agent had a significant coupled effect on the predicted nanocomposite loss moduli. Coupled high-shear mixing/ultrasonication gave the lowest predicted loss moduli, while ultrasonication gave the highest predicted loss moduli over the entire range of VGCNF weight fractions. The dispersing agent had a significant effect on the loss moduli of nanocomposites prepared using ultrasonication. Its use significantly increased the predicted loss modulus values. Overall, the inclusion of relatively small weight fractions of nanofibers (< 0.50 phr) led to a 20% increase in the predicted storage modulus in comparison to that of the neat VE.

- 2) Temperature was added as a design factor in the designed experimental study of the viscoelastic properties of VGCNF/VE nanocomposites, leading to new response surface models incorporating two quantitative factors, i.e., VGCNF weight fraction and temperature. This allowed for a temperature-dependent optimization of the nanocomposites' storage and loss moduli. The predicted storage modulus was a function of three mixing combinations, i.e., high-shear mixing (or high-shear mixing/ultrasonication), ultrasonication with oxidized VGCNFs in the presence of a dispersing agent, and ultrasonication with other VGCNF type/dispersing agent combinations over the entire temperature range

(30-120 °C). A similar but simpler dependence was observed for the loss modulus, where the ultrasonication combinations all had the same effect on the predicted loss modulus. The response surface models were used to identify combinations of formulation and processing factors that would lead to optimal predicted nanocomposite viscoelastic properties over the entire temperature range. The use of high-shear mixing, oxidized VGCNFs without a dispersing agent or pristine VGCNFs with a dispersing agent, and a VGCNF weight fraction of ~0.50 phr are recommended for maximizing the storage modulus at low, moderate, and high temperatures. For a low loss modulus over the same temperature range, the combination of oxidized VGCNFs with no dispersing agent is recommended. However, the combination of pristine VGCNFs with a dispersing agent would yield moderate energy dissipation. To maximize the loss modulus over the entire temperature range, the use of ultrasonication with ~0.25 phr VGCNF is recommended. Nevertheless, this will result in lower predicted storage moduli compared to the high-shear mixing.

- 3) The MD simulations of the interphase formation in VGCNF/VE nanocomposites incorporated a simulation cell containing resin monomers in their actual molar ratios in contact with an idealized surface of a VGCNF in the form of overlapping graphene sheets. A total simulation time of ~13 ns was considered to achieve equilibrium monomer distributions in the cell calculated as their relative concentrations. The final averaged concentration profiles revealed that the styrene/VE monomer ratios were substantially higher within 5 Å of the nanofiber-resin surface compared to their bulk ratios. These perturbed molar ratios of the

monomers near the nanofiber surface may result in a 5-10 Å thick interphase region if they are retained within the matrix structure during curing. The styrene-rich layer near the nanofiber surface and the increased VE2/VE1 ratio may yield a more locally compliant matrix with a lower crosslink density. Furthermore, a lightly crosslinked interphase with a large number of styrene-graphene interactions could result in improved nanofiber-matrix interfacial shear strengths compared to a more highly crosslinked matrix with bulk monomer composition.

Both the experimental and molecular modeling results presented in this dissertation represent novel methods to address key issues in the fabrication, characterization, and predictive modeling of thermoset nanocomposites. The empirical study of VGCNF/VE nanocomposites can be extended to include more design factors. These may include 1) nanoreinforcement type, such as carbon nanotubes, nano graphene platelets, nanoclays, polyhedral oligomeric silsesquioxane (POSS), 2) type and amount of dispersing agent, 3) more levels for the mixing method, such as three-roll milling, and 4) mixing time and/or intensity. A variety of mechanical responses, such as tensile, flexural, and compressive moduli and strength, could also be considered. A comprehensive study would then optimize the VGCNF/VE nanocomposites with respect to all the selected design factors and responses. Once optimized, the VGCNF/VE nanocomposite could be incorporated into continuous fiber/woven fabric laminates, whereby their mechanical performance could be characterized.

The MD simulations could be extended to include resin-nanofiber interaction effects on the interphase formation for the case of oxidized VGCNFs. The results of these simulations could then be compared to the case of pristine VGCNFs presented here. Once

established, the interphase region could be included in a crosslinked VGCNF/VE nanocomposite for further analysis of nanocomposite properties such as bulk modulus and interfacial shear strength through MD simulations. These calculated properties could then be fed to higher length scale mechanical models as part of a multi-scale modeling methodology for thermoset nanocomposites in general and VGCNF/VE nanocomposites in particular.

REFERENCES

- Abadie, M. J. M., Mekhissi, K., & Burchill, B. J. (2002). Effects of processing conditions on the curing of a vinyl ester resin. *Journal of Applied Polymer Science*, 84 (6), 1146-1154.
- Accelrys Materials Studio (2011):
<http://accelrys.com/products/materials-studio/> (Date accessed: March 2011).
- Adnan, A., Sun, C. T., & Mahfuz, H. (2007). A molecular dynamics simulation study to investigate the effect of filler size on elastic properties of polymer nanocomposites. *Composites Science and Technology*, 67, 348-356.
- Agarwal, S., Khan, M. M. K., & Gupta, R. K. (2008). Thermal conductivity of polymer nanocomposites made with carbon nanofibers. *Polymer Engineering and Science*, 48 (12), 2474-2481.
- Allaoui, A., Hoa, S. V., & Pugh, M. D. (2008). The electronic transport properties and microstructure of carbon nanofiber/epoxy composites. *Composites Science and Technology*, 68 (2), 410-416.
- Al-Saleh, M. H., & Sundararaj, U. (2009). A review of vapor grown carbon nanofiber/polymer conductive composites. *Carbon*, 47 (1), 2-22.
- Al-Saleh, M. H., & Sundararaj, U. (2010). Processing-microstructure-property relationship in conductive polymer nanocomposites. *Polymer*, 51 (12), 2740-2747.
- Applied Sciences, Inc. (2001):
<http://www.apsci.com/ppi-pyro3.html> (Date accessed: March 2011).
- Ashland Co. (2005). Composite polymers: fabricating tips. *Bulletin #2898*, 4-13.
- Ash, B. J., Siegel, R. W., & Schadler, L. S. (2004). Glass-transition temperature behavior of alumina/PMMA nanocomposites. *Journal of Polymer Science*, 42 (23), 4371-4383.

- Baker, R. T. K., Barber, M. A., Harris, P. S., Feates, F. S., & Waite, R. J. (1972). Nucleation and growth of carbon deposits from the nickel catalyzed decomposition of acetylene. *Journal of Catalysis*, 26 (1), 51-62.
- Bal, S. (2010). Experimental study of mechanical and electrical properties of carbon nanofiber/epoxy composites. *Materials and Design*, 31 (5), 2406-2413.
- Barber, A. H., Cohen, S. R., & Wagner, H. D. (2003). Measurement of carbon nanotube-polymer interfacial strength. *Applied Physics Letters*, 82 (23), 4140-4142.
- Bedrov, D., Smith, G. D., & Smith, J. S. (2003). Matrix-induced nanoparticle interactions in a polymer melt: a molecular dynamics simulation study. *Journal of Chemical Physics*, 119 (19), 10438-10447.
- Bellucci, F., Terenzi, A., Leuteritz, A., Pospiech, D., Frache, A., Traverso, G., et al. (2008). Intercalation degree in PP/organoclay nanocomposites: role of surfactant structure. *Polymers for Advanced Technologies*, 19 (6), 547-555.
- Benissad, F., Gadelle, P., Coulon, M., & Bonnetain, L. (1988). Formation de fibres de carbone a partir du methane: i croissance catalytique et epaississement pyrolytique. *Carbon*, 26, 61-69.
- Berthelot, J. -M. (1999). *Composite materials, mechanical behavior and structural analysis*. New York, NY: Springer-Verlag, 1999, p. 3.
- Binder, K. (1995). *Monte Carlo and molecular dynamics simulations in polymer science*. New York, NY: Oxford University Press.
- Biró, L. P., Bernardo, C. A., Tibbetts, G. G., & Lambin, P. (2001). *Carbon filaments and nanotubes: common origins, differing applications?* Dordrecht, The Netherlands: Kluwer Academic Publishers.
- Bourbigot, S., Fontaine, G., Bellayer, S., & Delobel, R. (2008). Processing and nanodispersion: a quantitative approach for polylactide nanocomposite. *Polymer Testing*, 27, 2-10.
- Bruins, P. F. (1976). *Unsaturated polyester technology*. New York, NY: Gordon and Breach Science Publishers, pp. 343-344.
- Burchell, T. D. (1999). *Carbon materials for advanced technologies*. Oxford, UK: Pergamon (Elsevier Science Ltd.).
- Buryachenko, V. A., Roy, A., Lafdi, K., Anderson, K. L., & Chellapilla, S. (2005). Multi-scale mechanics of nanocomposites including interface: experimental and numerical investigation. *Composites Science and Technology*, 65, 2435-2465.

- Carneiro, O. S., Covas, J. A., Bernardo, C. A., Caldeira, G., van Hattum, F. W. J., Ting, J. -M., et al. (1998). Production and assessment of polycarbonate composites reinforced with vapor grown carbon fibers. *Composites Science and Technology*, 58, 401-407.
- Chávez-Medellín, R., Sanchez de Almeida Prado, L. A., & Schulte, K. (2010). Polyamide-12/functionalized carbon nanofiber composites: evaluation of thermal and mechanical properties. *Macromolecular Materials and Engineering*, 295 (4), 397-405.
- Chaos-Morán, R., Campo, M., Prolongo, S. G., Escalera, M. D., & Ureña, A. (2009). The functionalization of carbon nanofibers with 4,40-diaminodiphenylmethane, a curing agent for epoxy resins. *Journal of Materials Research*, 24 (4), 1435-1445.
- Chen, X. Q., Saito, T., Yamada, H., & Matsushige, K. (2001). Aligning single-wall carbon nanotubes with an alternating-current electric field. *Applied Physics Letters*, 78, 3714–3716.
- Cho, J. & Sun, C. T. (2007). A molecular dynamics simulation study of inclusion size effect on polymeric nanocomposites. *Computational Materials Science*, 41, 54-62.
- Cho, J., Daniel, I. M., & Dikin, D. A. (2008). Effects of block copolymer dispersant and nanotube length on reinforcement of carbon/epoxy composites. *Composites: Part A*, 39 (12), 1844-1850.
- Chowdhury, S. C. & Okabe, T. (2007). Computer simulation of carbon nanotube pull-out from polymer by molecular dynamics method. *Composites: Part A*, 38, 747-754.
- Choi, Y. -K., Sugimoto, K., Song, S. -M., Gotoh, Y., Ohkoshi, Y., & Endo, M. Mechanical and physical properties of epoxy composites reinforced by vapor grown carbon nanofibers. *Carbon*, 43, 2199-2208.
- Choi, Y. -K, Sugimoto, K., Song, S. -M., & Endo, M. (2006). Production and characterization of polycarbonate composite sheets reinforced with vapor grown carbon fiber. *Composites: Part A*, 37 (11), 1944-1951.
- Ciecierska, E., Boczkowska, A., & Kurzydowski, K. J. (2010). Quantitative description of the spatial dispersion of carbon nanotubes in polymeric matrix. *Journal of Materials Science*, 45 (9), 2305-2310.
- Coleman, J. N., Cadek, M., Ryan, K. P., Fonseca, A., Nagy, J. B., Blau, W. J., et al. Reinforcement of polymers with carbon nanotubes. the role of an ordered polymer interfacial region. Experiment and modeling." *Polymer*, 47, 8556-8561.

- Cox, D. R. & Reid, N. (2000). *The theory of the design of experiments*. Boca Raton, FL: Chapman & Hall/CRC.
- Cooper, C. A., Cohen, S. R., Barber, A. H., & Wagner, H. D. (2002). Detachment of nanotubes from a polymer matrix. *Applied Physics Letters*, 81 (20), 3873-3875.
- Cui, H., Yang, X., Simpson, M. L., Lowndes, D. H., & Varela, M. (2004). Initial growth of vertically aligned carbon nanofibers. *Applied Physics Letters*, 84 (20), 4077-4079.
- Dalton, A. & Jurewicz, I. (2007). Nanotechnology meets bubbleology.” *Nature Nanotechnology*, 2, 339–340.
- De Gennes, P. G. (1971). Reptation of a polymer chain in the presence of fixed obstacles. *Journal of Chemical Physics*, 55 (2), 580-588.
- De Jong, K. P. & Geus, J. W. (2000). Carbon nanofibers: catalytic synthesis and applications. *Catalysis Reviews*, 42 (4), 481-510.
- DL_POLY (2011):
http://www.cse.scitech.ac.uk/ccg/software/DL_POLY/ (Date accessed: March 2011).
- Doshi, J. & Reneker, D. H. (1995). Electrospinning process and applications of electrospun fibers. *Journal of Electrostatics*, 35 (2-3), 151-160.
- Dresselhaus, M. S., Dresselhaus, G., Sugihara, K., Spain, I. L., & Goldberg, H. A. (1988). *Graphite fibers and filaments*. New York, NY: Springer-Verlag.
- Edser, C. (2002). Auto applications drive commercialization of nanocomposites. *Plastics Additives and Compounding*, 4, 30-33.
- Elgafy, A. & Lafdi, K. (2005). Effect of carbon nanofiber additives on thermal behavior of phase change materials. *Carbon*, 43 (15), 3067-3074.
- Ellis, T. S. & D'Angelo, J. S. (2003). Thermal and mechanical properties of a polypropylene nanocomposite. *Journal of Applied Polymer Science*, 90 (6), 1639-1647.
- Ellison, S. L. R., Barwick, V. J., & Duguid Farrant, T. J. (2009). *Practical statistics for the analytical scientist, a bench guide*. Cambridge, UK: The Royal Society of Chemistry, pp.59-91.
- Endo, M., Shikata, M. (1985). (In Japanese). *Ohyo Butsuri*, 54, p. 507.

- Endo, M., Kim, Y. A., Takeda, T., Hong, S. H., Matusita, T., Hayashi, T., et al. (2001). Structural characterization of carbon nanofibers obtained by hydrocarbon pyrolysis. *Carbon*, *39* (13), 2003-2010.
- Endo, M., Kim, Y. A., Hayashi, T., Fukai, Y., Oshida, K., Terrones, H., et al. (2002). Structural characterization of cup-stacked-type nanofibers with an entirely hollow core. *Applied Physics Letters*, *80* (7), 1267-1269.
- Endo, M., Kim, Y. A., Hayashi, T., Yanagisawa, T., Muramatsu, H., Ezaka, M., et al. (2003). Microstructural changes induced in “stacked cup” carbon nanofibers by heat treatment.” *Carbon*, *41* (10), 1941-1947.
- Endruweit, A., Johnson, M. S., & Long, A. C. (2006). Curing of composite components by ultraviolet radiation: a review. *Polymer Composites*, *27* (2), 1198-128.
- Esbensen, K. H., Guyot, D., Westad, F., & Houmøller, L. P. (2010). *Multivariate data analysis - in practice: an introduction to multivariate data analysis and experimental design* (5th ed.). Oslo, Norway: CAMO Publisher.
- Evora, M. C., Klosterman, D., Lafdi, K., Li, L., & Abot, J. L. (2010). Functionalization of carbon nanofibers through electron beam irradiation. *Carbon*, *48* (7), 2037-2046.
- Faraz, M. I., Bhowmik, S., De Ruijter, C., Laoutid, F., Benedictus, R., Dubois, P., et al. (2010). Thermal, morphological, and mechanical characterization of novel carbon nanofiber-filled bismaleimide composites. *Journal of Applied Polymer Science*, *117* (4), 2159-2167.
- Finegan, I. C., Tibbetts, G. G., Glasgow, D. G., Ting, J. -M., & Lake, M. L. (2003). Surface treatments for improving the mechanical properties of carbon nanofiber/thermoplastic composites. *Journal of Materials Science*, *38*, 3485-3490.
- Fischer, H. (2003). Polymer nanocomposites: from fundamental research to specific applications. *Materials Science and Engineering: Part C*, *23*, 763-772.
- Frankland, S. J. V., Caglar, A., Brenner, D. W., & Griebel, M. (2002). Molecular simulation of the influence of chemical cross-links on the shear strength of carbon nanotube-polymer interfaces. *Journal of Physical Chemistry*, *106*, 3046-3048.
- Frankland, S. J. V., Harik, V. M., Odegard, G. M., Brenner, D. W., & Gates, T. S. (2003). The stress-strain behavior of polymer-nanotube composites from molecular dynamics simulation. *Composites Science and Technology*, *63*, 1655-1661.
- Frankland, S. J. V. & Gates, T. S. (2007). Local elastic constants for epoxy-nanotube composites from molecular dynamics simulation. In the proceedings of Materials Research Society Fall Meeting, Boston, MA, November 26-30.

- Fratzel, P. (2003). Small-angle scattering in materials science - a short review of applications in alloys, ceramics and composite materials. *Journal of Applied Crystallography*, *36*, 397-404.
- Frenkel, D., & Smit, B. (2002). *Understanding molecular simulation, from algorithms to applications*. London, UK: Academic Press.
- Fu, Y., Han, C., & Ni, Q. (2009). Effects of surface modification on the dispersion property of VGCF.” *Chinese Journal of Chemistry*, *27* (6), 1110-6.
- Garcés, J. M., Moll, D. J., Bicerano, J., Fibiger, R., & McLeod, D. G. (2000). Polymeric nanocomposites for automotive applications. *Advanced Materials*, *12* (23), 1835-1839.
- Garmestani, H., Al-Haik, M. S., Dahmen, K., Tannenbaum, R., Li, D., Sablin, S. S., & Hussaini, M. Y. (2003). Polymer-mediated alignment of carbon nanotubes under high magnetic fields. *Advanced Materials*, *15*, 1918–1921.
- Gates, T. S., Odegard, G. M., Frankland, S. J. V., & Clancy, T. C. (2005). Computational materials: multi-scale modeling and simulation of nanostructured materials. *Composites Science and Technology*, *65*, 2416-2434.
- Gedde, U. W. (1999). *Polymer physics*. Dordrecht, The Netherlands: Kluwer Academic Publishers, p. 21.
- George, J. J. & Bhowmick, A. K. (2008). Fabrication and properties of ethylene vinyl acetate-carbon nanofiber nanocomposites. *Nanoscale Research Letters*, *3*, 508-515.
- Gersappe, D. (2002). Molecular mechanisms of failure in polymer nanocomposites.” *Physical Review Letters*, *89* (5), 058301-(1-4).
- Gibson, R. F., Ayorinde, E. O., & Wen, Y. -F. (2007). Vibrations of carbon nanotubes and their composites: a review. *Composites Science and Technology*, *67* (1), 1-28.
- Glotzer, S. C. & Paul, W. (2002). Molecular and mesoscale simulation methods for polymer materials. *Annual Review of Materials Research*, *32*, 401-436.
- Goodman, S. H. (1998). *Handbook of thermoset plastics* (2nd ed.). Westwood, New Jersey: Noyes Publications, pp. 122-142.
- Gou, J., Minaei, B., Wang, B., Liang, Z., & Zhang, C. (2004). Computational and experimental study of interfacial bonding of single-walled nanotube reinforced composites. *Computational Materials Science*, *31*, 225-236.

- Gou, J., Liang, Z., Zhang, C., & Wang, B. (2005). Computational analysis of effect of single-walled carbon nanotube rope on molecular interaction and load transfer of nanocomposites. *Composites: Part B*, 36, 524-533.
- Gou, J., Anumakonda, K., & Khan, A. (2007). Molecular dynamics simulation of interactions between functionalized carbon nanofibers and polymer resins. *International Journal of Nanoscience*, 6 (6), 443-452.
- Gupta, R. K., Kennel, E., & Kim, K. -J. (2010). *Polymer nanocomposites handbook*. Boca Raton, FL: Taylor & Francis Group (CRC Press), pp. 223-251.
- Haile, J. M. (1992). *Molecular dynamics simulation, elementary methods*. New York, NY: John Wiley & Sons.
- Hammel, E., Tang, X., Trampert, M., Schmitt, T., Mauthner, K., Eder, A., et al. (2004). Carbon nanofibers for composite applications. *Carbon*, 42, 1153-1158.
- Han, Y. & Elliott, J. (2007). Molecular dynamics simulations of the elastic properties of polymer/carbon nanotube composites. *Computational Materials Science*, 39, 315-323.
- Harper, C. A. (2002). *Handbook of plastics, elastomers, and composites* (4th ed.). New York, NY: McGraw-Hill, pp. 598-599.
- Hasan, M. M., Zhou, Y., & Jeelani, S. (2007). Thermal and tensile properties of aligned carbon nanofiber reinforced polypropylene. *Materials Letters*, 61 (4-5), 1134-1136.
- Hatano, M., Ohsaki, T., & Arakawa, K. (1985). Graphite whiskers by new process and their composites, advancing technology in materials and processes. *Science of Advanced Materials and Processes, National SAMPE Symposium*, 30, 1467-1476.
- He, P., Gao, Y., Lian, J., Wang, L., Qian, D., Zhao, J., et al. (2006). Surface modification and ultrasonication effect on the mechanical properties of carbon nanofiber/polycarbonate composites. *Composites: Part A*, 37 (9), 1270-1275.
- Henrich, F., Chan, C., Morre, V., Rolandi, M., & O'Connell, M. (2006). The element carbon. In M. O'Connell (Ed.), *Carbon nanotubes: properties and applications* (pp. 1-2). Boca Raton, FL: Taylor & Francis Group.
- Hine, P., Broome, V., & Ward, I. (2005). The incorporation of carbon nanofibres to enhance the properties of self reinforced, single polymer composites. *Polymer*, 46 (24), 10936-10944.

- Huang, Z. -M., Zhang, Y. -Z., Motaki, M., & Ramakrishna, S. (2003). A review on polymer nanofibers by electrospinning and their applications in nanocomposites. *Composites Science and Technology*, 63 (15), 2223-2253.
- Hughes, T. V. & Chambers, C. R. (1889). Manufacture of carbon filaments. U.S. Patent no. 405,480.
- Hussain, F., Hojjati, M., Okamoto, & M., Gorga, R. E. (2006). Review article: polymer-matrix nanocomposites, processing, manufacturing, and application: an overview. *Journal of Composite Materials*, 40 (17), 1511-1575.
- Iijima, S. (1991). Helical microtubules of graphitic carbon. *Nature*, 354, 56-58.
- Jancar, J. (2008). Review of the role of the interphase in the control of composite performance on micro- and nano-length scales. *Journal of Materials Science*, 43, 6747-6757.
- Jancar, J. (2009). Interphase phenomena in polymer micro- and nanocomposites. In J. Karger-Kocsis, & S. Fakirov (Eds.), *Nano- and micro-mechanics of polymer blends and composites* (pp. 241-266). Cincinnati, OH: Hanser Publications.
- Jang, B. N., Wang, D., & Wilkie, C. A. (2005). Relationship between the solubility parameter of polymers and the clay dispersion in polymer/clay nanocomposites and the role of the surfactant. *Macromolecules*, 38 (15), 6533-6543.
- Ji, G. & Li G. (2008). Effects of nanoclay morphology on the mechanical, thermal, and fire-retardant properties of vinyl ester based nanocomposite. *Materials Science and Engineering: Part A*, 498, 327-334.
- Jimenez, G. A. & Jana, S. C. (2007). Electrically conductive polymer nanocomposites of polymethylmethacrylate and carbon nanofibers prepared by chaotic mixing. *Composites: Part A*, 38 (3), 983-993.
- Jin, L., Bower, C., & Zhou, O. (1998). Alignment of carbon nanotubes in a polymer matrix by mechanical stretching. *Applied Physics Letters*, 73, 1197-1199.
- Kabir, M. E., Saha, M. C., & Jeelani, S. (2007). Effect of ultrasound sonication in carbon nanofibers/polyurethane foam composite. *Materials Science and Engineering: Part A*, 459 (1-2), 111-116.
- Kairn, T., & Daivis, P. J. (2005). Molecular dynamics simulation of model polymer nanocomposite rheology and comparison with experiment. *Journal of Chemical Physics*, 123, 194905.

- Kang, I., Heung, Y. Y., Kim, J. H., Lee, J. W., Gollapudi, R., Subramaniam, S., et al. (2006). Introduction to carbon nanotube and nanofiber smart materials. *Composites: Part B*, 37, 382-394.
- Karippal, J. J., Narasimha Murthy, H. N., Rai, K. S., Krishna, M., & Sreejith, M. (2010, May). Effect of amine functionalization of CNF on electrical, thermal, and mechanical properties of epoxy/CNF composites. *Polymer Bulletin*.
- Khare, H. S. & Burris, D. L. (2010). A quantitative method for measuring nanocomposite dispersion. *Polymer*, 51 (3), 719-729.
- Kim, Y. A., Hayashi, T., Endo, M., Gotoh, Y., Wada, N., & Seiyama, J. (2006). Fabrication of aligned carbon nanotube-filled rubber composite. *Scripta Materialia*, 54 (1), 31-35.
- Kimura, T., Ago, H., Tobita, M., Ohshima, S., Kyotani, M., & Yumura, M. (2002). Polymer composites of carbon nanotubes aligned by a magnetic field. *Advanced Materials*, 14, 1380–1383.
- Klein, K. L., Melechko, A. V., McKnight, T. E., Retterer, S. T., Rack, P. D., Fowlkes, J. D., et al. (2008). Surface characterization and functionalization of carbon nanofibers. *Journal of Applied Physics*, 103 (6), 061301-26.
- Kleinbaum, D. G. & Klein, M. (2010). *Logistic regression, a self-learning text* (3rd Ed.). New York, NY: Springer Science + Business Media, pp. 181-187.
- Kornmann, X., Lindberg, H., & Berglund, L. A. (2001). Synthesis of epoxy–clay nanocomposites: influence of the nature of the clay on structure. *Polymer*, 42 (4), 1303-1310.
- Koyama, T. (1972). Formation of carbon fibers from benzene. *Carbon*, 10, p. 757.
- Koyama, T. & Endo, M. T. (1973). Structure and growth processes of vapor-grown carbon fibers (in Japanese). *Ohyo Butsuri*, 42, p. 690.
- Koyama, T. & Endo, M. T. (1983). Method for manufacturing carbon fibers by a vapor phase process. Japanese Patent 1982-58, 966.
- Kulshreshtha, A. K. (2002). History of composites. In A. K. Kulshreshtha & C. Vasile (Eds.), *Handbook of polymer blends and composites, volume 1* (p. 5). Shropshire, UK: RAPRA Technology, Ltd.
- Kumar, S., Rath, T., Mahaling, R. N., Reddy, C. S., Das, C. K., Pandey, K. N., et al. Study on mechanical, morphological and electrical properties of carbon

- nanofiber/polyetherimide composite. *Materials Science and Engineering: Part B*, 141 (1-2), pp. 61-70.
- Lafdi, K., Fox, W., Matzek, M., & Yildiz, E. (2007). Effect of carbon nanofiber heat treatment on physical properties of polymeric nanocomposite —part I. *Journal of Nanomaterials*, 6 pages.
- Lafdi, K., Fox, W., Matzek, M., & Yildiz, E. (2008). Effect of carbon nanofiber-matrix adhesion on polymeric nanocomposite properties—part II. *Journal of Nanomaterials*, 8 pages.
- Lakshminarayanan, P. V., Toghiani, H., & Pittman, C. U. (2004). Nitric acid oxidation of vapor grown carbon nanofibers. *Carbon*, 42, 2422-2433.
- LAMMPS Molecular Dynamics Simulation Program (2011):
<http://lammps.sandia.gov/> (Date accessed: March 2011).
- Lau, K. A., Hussain, F., & Lafdi, K. (2010). *Nano- and biocomposites*. Boca Raton, FL: Taylor & Francis Group (CRC Press), pp. 23-33.
- Lawrence, J. G., Berhan, L. M., & Nadarajah, A. (2008). Structural transformation of vapor grown carbon nanofibers studied by HRTEM. *Journal of Nanoparticle Research*, 10 (7), 1155-1167.
- Lee, S., Kim, M. -S., & Ogale, A. A. (2010). Influence of carbon nanofiber structure on properties of linear low density polyethylene composites. *Polymer Engineering and Science*, 50 (1), 93-99.
- Li, H. (1998). Synthesis, characterization, and properties of vinyl ester matrix resins. Blacksburg, VA, USA, Virginia Polytechnic Institute and State University, PhD Dissertation.
- Li, J., Vergne, M. J., Mowles, E. D., Zhong, W. -H., Hercules, D. M., & Lukehart, C. M. (2005). Surface functionalization and characterization of graphitic carbon nanofibers (GCNFs). *Carbon*, 43 (14), 2883-2893.
- Li, T. -C., Ma, J., Wang, M., Tjiu, W. C., Liu, T., & Huang, W. (2007). Effect of clay addition on the morphology and thermal behavior of polyamide 6. *Journal of Applied Polymer Science*, 103 (2), pp. 1191-1199.
- Liao, K. & Li, S. (2001). Interfacial characteristics of a carbon nanotube-polystyrene composite system. *Applied Physics Letters*, 79 (25), 4225-4227.

- Liao, Y. H., Marietta-Tondin, O., Liang, Z., Zhang, C., & Wang, B. (2004). Investigation of dispersion process of SWNTs/SC-15 epoxy resin nanocomposites. *Materials Science and Engineering: Part A*, 385, 175-181.
- Lopata, V. J., Saunders, C. B., Singh, A., Janke, C. J., Wrenn, G. E., & Havens, S. J. (1999). Electron-beam-curable epoxy resins for the manufacture of high-performance composites. *Radiation Physics and Chemistry*, 56 (4), 405-415.
- Lozano, K. & Barrera, E. V. (2001). Nanofiber-reinforced thermoplastic composites. I. Thermoanalytical and mechanical analyses. *Journal of Applied Polymer Science*, 79, 125-133.
- Luo, Z. P. & Koo, J. H. (2007). Quantifying the dispersion of mixture microstructures. *Journal of Microscopy*, 225 (2), 118-125.
- Luo, Z. P. & Koo, J. H. (2008). Quantification of the layer dispersion degree in polymer layered silicate nanocomposites by transmission electron microscopy. *Polymer*, 49, 1841-1852.
- Lucretius Molecular Dynamics Simulation Program (2011):
<http://www.che.utah.edu/~gdsmith/lucretius.html> (Date accessed: March 2011).
- Ma, H., Zeng, J., Realf, M. L., Kumar, S., & Schiraldi, D. A. (2003). Processing, structure, and properties of fibers from polyester/carbon nanofiber composites. *Composites Science and Technology*, 63 (11), 1617-1628.
- Maruyama, B. & Alam, K. (2002). Carbon nanotubes and nanofibers in composite materials. *SAMPE Journal*, 38 (3), 59-70.
- Mazumdar, S. K. (2002). *Composites manufacturing, materials, product, and process engineering*. Boca Raton, FL: CRC Press, p. 4.
- McConnell, V. P. (2010, November/December). Vinyl esters get radical in composite markets. *Reinforced Plastics Magazine*, pp. 34-38.
- McHugh, J.J. and Tibbetts, G.G. "Treatment of Vapor-Grown carbon Fibers for Fiber-Polymer Matrix Composites." U.S. Patent no. 5,853,865, 1998.
- Menard, K. P. (1999). *Dynamic mechanical analysis: a practical introduction*. Boca Raton, FL: CRC Press.
- Mokashi, V. V., Qian, D., & Liu, Y. (2007). A study on the tensile response and fracture in carbon nanotube-based composites using molecular mechanics. *Composites Science and Technology*, 67, 530-540.

- Montazeri, A. & Naghdabadi, R. (2010). Investigation of the interphase effects on the mechanical behavior of carbon nanotube polymer composites by multiscale modeling. *Journal of Applied Polymer Science*, 117 (1), 361-367.
- Montgomery, D. C. (2009). *Design and analysis of experiments* (7th ed.). New Jersey: John Wiley & Sons, pp. 440-442.
- Moore, A. L., Cummings, A. T., Jensen, J. M., Shi, L., & Koo, J. H. (2009). Thermal conductivity measurements of nylon 11-carbon nanofiber nanocomposites. *Journal of Heat Transfer*, 131 (9), p. 091602.
- Morales, G., Barrena, M. I., Gómez de Salazar, J. M., Merino, C., & Rodriguez, D. (2010). Conductive CNF-reinforced hybrid composites by injection molding. *Composite Structures*, 92 (6), 1416-1422.
- Morales-Teyssier, O., Sánchez-Valdez, S., & Ramos-de Valle, L. F. (2006). Effect of carbon nanofiber functionalization on the dispersion and physical and mechanical properties of polystyrene nanocomposites. *Macromolecular Materials and Engineering*, 291 (12), 1547-1555.
- Morgan, A. B. & Gilman, J. W. (2003). Characterization of polymer-layered silicate (clay) nanocomposites by transmission electron microscopy and X-ray diffraction: a comparative study. *Journal of Applied Polymer Science*, 87 (8), 1329-1338.
- Morgan, P. (2005). *Carbon fibers and their composites*. Boca Raton, FL: Taylor & Francis Group (CRC Press).
- Morgan, A. B. & Liu, W. (2010). Flammability of thermoplastic carbon nanofiber nanocomposites. *Fire and Materials*, online publication.
- Myers, R. H., Montgomery, D. C., & Anderson-Cook, C. M. (2009). *Response surface methodology, process and product optimization using designed experiments* (3rd ed.). New Jersey: John Wiley & Sons.
- NAMD Molecular Dynamics Simulation Program (2011):
<http://www.ks.uiuc.edu/Research/namd/> (Date accessed: March 2011).
- Nanni, F., Travaglia, P., & Valentini, M. (2009). Effect of carbon nanofibres dispersion on the microwave absorbing properties of CNF/epoxy composites. *Composites Science and Technology*, 69 (3-4), 485-490.
- Nielsen, L. E. & Landel, R. F. (1994). *Mechanical properties of polymers and composites* (2nd ed.). New York, NY: Marcel Dekker.

NIST SEMATECH (2011):

<http://www.itl.nist.gov/div898/handbook/pri/section7/pri7.htm>

(Date accessed: March 2011).

Nouranian, S., Toghiani, H., Lacy, T. E., & Pittman Jr., C. U. (2009). Response surface study of vapor-grown carbon nanofiber/vinyl ester nanocomposites fabricated using high-shear mixing. In the proceedings of the 24th Annual Technical Conference of the American Society for Composites, Newark, DE, September 15-17.

Oberlin, A., Endo, M., & Koyama, T. (1976). Filamentous growth of carbon through benzene decomposition. *Journal of Crystal growth*, 32 (3), 335-349.

O'Connell, M. J. (2006). *Carbon nanotubes: properties and applications*. Boca Raton, FL: Taylor & Francis Group (CRC Press), pp. 215.

Ogasawara, T., Ishida, Y., & Ishikawa, T. (2004). Properties of vapor grown carbon nano fiber/phenylethynyl terminated polyimide composite. *Advanced Composite Materials*, 13 (3-4), 215-226.

Ott, R. (2009). DOE industrial technologies program, overview of nanomanufacturing initiative.

Ott, L. & Longnecker, M. (2010). *An introduction to statistical methods and data analysis* (6th ed.). Belmont, CA: Brooks/Cole, Cengage Learning, pp. 250-259.

Özkan, T., Naraghi, M., & Chasiotis, I. (2010). Mechanical properties of vapor grown carbon nanofibers. *Carbon*, 48 (1), 239-244.

Park, C., Wilkinson, J., Banda, S., Ounaies, Z., Wise, K.E., Sauti, G., et al. (2006). Aligned single-wall carbon nanotube polymer composites using an electric field. *Journal of Polymer Science: Part B*, 44, 1751-1762.

Park, J. H., Alegaonkar, P. S., Jeon, S. Y., & Yoo, J. B. (2008). Carbon nanotube composite: dispersion routes and field emission parameters. *Composites Science and Technology*, 68 (3-4), 753-759.

Patton, R. D., Pittman, Jr., C. U., Wang, L., & Hill, J. R. (1999). Vapor grown carbon fiber composites with epoxy and poly(phenylene sulfide) matrices. *Composites: Part A*, 30, 1081-1091.

Patton, R. D., Pittman, Jr., C. U., Wang, L., Hill, J. R., & Day, A. (2002). Ablation, mechanical and thermal conductivity properties of vapor grown carbon fiber/phenolic matrix composites. *Composites: Part A*, 33 (2), 243-251.

- Plaseied, A., Fatemi, A., & Coleman, M. R. (2008). The Influence of carbon nanofiber content and surface treatment on mechanical properties of vinyl ester. *Polymer Polymer Composites*, 16 (7), 405–413.
- Plaseied, A., & Fatemi, A. (2009). Tensile creep and deformation modeling of vinyl ester polymer and its nanocomposite. *Journal of Reinforced Plastics and Composites*, 28 (14), 1775-1788.
- Podsiadlo, P., Kaushik, A. K., Arruda, E. M., Waas, A. M., Shim, B. S., Xu J., et al. (2007). Ultrastrong and stiff layered polymer nanocomposites. *Science*, 318, 80-83.
- Prestin, H. & König, U. (2003). Future nanotechnology developments for automotive applications. *Materials Science and Engineering: Part C*, 23, 737-741.
- Putz, K., Krishnamoorti, R., & Green, P. F. (2007). The role of interfacial interactions in the dynamic mechanical response of functionalized SWNT-PS nanocomposites. *Polymer*, 48, 3540-3545.
- Pyrograf Products (an Affiliate of Applied Sciences, Inc.) (2011):
http://pyrografproducts.com/Merchant5/merchant.mvc?Screen=cp_nanofiber
 (Date accessed: March 2011).
- Qiao, R. & Brinson, L. C. (2009). Gradient interphases in polymer nanocomposites. In the proceedings of ASME 2009 International Mechanical Engineering Congress and Exposition, Lake Buena Vista, FL, November 13–19, pp. 883-884.
- Rapaport, D. C. (2004). *The art of molecular dynamics simulation* (2nd ed.). Cambridge, UK: Cambridge University Press.
- Rasheed, A., Dadmun, M. D., & Britt, P. F. (2006). Polymer-nanofiber composites: enhancing composite properties by nanofiber oxidation. *Journal of Polymer Science: Part B*, 44 (21), 3053-3061.
- Ratna, D. (2009). *Handbook of thermoset resins*. Shropshire, UK: Smithers RAPRA, pp. 100-102.
- Ren, X., Wang, X. Q., Sui, G., Zhong, W. H., Fuqua, M. A., & Ulven, C. A. (2008). Effects of carbon nanofibers on crystalline structures and properties of ultrahigh molecular weight polyethylene blend fabricated using twin-screw extrusion. *Journal of Applied Polymer Science*, 107, 2837-2845.
- Rodriquez, N. M. (1993). Review of catalytically grown carbon nanofibers. *Journal of Materials Research*, 8 (12), 3233.

- SAS 9.2 software (2011):
<http://www.sas.com/software/sas9/> (Date accessed: March 2011).
- Sandler, J., Shaffer, M. S. P., Lam, Y. -M., Windle, A. H., Werner, P., Altstädt, V., et al. (2002). Carbon-nanofiber-filled thermoplastic composites. *Materials Research Society Symposium Proceedings*, 706, Z4.7.1-Z4.7.6.
- Sandler, J. K. W., Pegel, S., Cadek, M., Gojny, F., van Es, M., Lohmar, J., et al. (2004). A comparative study of melt spun polyamide-12 fibers reinforced with carbon nanotubes and nanofibers. *Polymer*, 45 (6), 2001-2015.
- Schadler, L. S., Brinson, L. C., & Sawyer, W. G. (2007, March). Polymer nanocomposites: a small part of the story. *JOM*, pp. 53-60.
- Schmidt, G., Nakatani, A. I., Butler, P. D., & Han, C. C. (2002). Small-angle neutron scattering from viscoelastic polymer-clay solutions. *Macromolecules*, 35 (12), 4725-4732.
- Sennett, M., Welsh, E., Wright, J. B., Li, W. Z., Wen, J. G., and Ren. Z. F. (2003). Dispersion and alignment of carbon nanotubes in polycarbonate. *Applied Physics: Part A*, 76, 111-113.
- Shi, D., Lian, J., He, P., Wang, L. M., Xiao, F., Yang, L., et al. (2003). Plasma coating of carbon nanofibers for enhanced dispersion and interfacial bonding in polymer composites. *Applied Physics Letters*, 83 (25), 5301-5303.
- Shibayama, M., Karino, T., Miyazaki, S., Okabe, S., Takehisa, T., & Haraguchi, K. (2005). Small-angle neutron scattering study on uniaxially stretched poly(N-isopropylacrylamide)-clay nanocomposite gels. *Macromolecules*, 38 (26), 10772-10781.
- Shonaike, G. O. & Advani, S. G. (2003). *Advanced polymeric materials, structure property relationships*. Boca Raton, FL: CRC Press, pp. 235-245.
- Sikdar, D., Katti, D. R., Katti, K. S., & Bhowmik, R. (2006). Insight into molecular interactions between constituents in polymer clay nanocomposites. *Polymer*, 47, 5196-5205.
- Sikdar, D., Katti, D. R., & Katti, K. S. (2008). The role of interfacial interactions on the crystallinity and nanomechanical properties of clay-polymer nanocomposites: a molecular dynamics study. *Journal of Applied Polymer Science*, 107, 3137-3148.
- Siochi, E. J., Working, D. C., Park, C., Lillehei, P. T., Rouse, J. H., Topping, C. C., et al. (2004). Melt processing of SWCNT-polyimide nanocomposite fibers. *Composites: Part B*, 35 (5), 439-446.

- Smith, J. S., Bedrov, D., & Smith, G. D. (2003). A molecular dynamics simulation study of nanoparticle interactions in a model polymer-nanoparticle composite. *Composites Science and Technology*, 63, 1599-1605.
- Stevens, J. L., Huang, A. Y., Peng, H., Chiang, I. W., & Khabashesku, V. N. (2003). Sidewall amino-functionalization of single-walled carbon nanotubes through fluorination and subsequent reactions with terminal diamines. *Nano Letters*, 3 (3), 331-336.
- Sui, G., Jana, S., Zhong, W. H., Fuqua, M. A., & Ulven, C. A. (2008). Dielectric properties and conductivity of carbon nanofiber/semi-crystalline polymer composite. *Acta Materialia*, 56 (10), 2381-2388.
- Sun, H. (1998). COMPASS: an ab initio force-field optimized for condensed-phase applications: overview with details on alkane and benzene compounds. *Journal of Physical Chemistry: Part B*, 102 (38), 7338-7364.
- Takahashi, T., Suzuki, K., Awano, H., & Yonetake, K. (2007). Alignment of vapor-grown carbon fibers in polymer under magnetic field. *Chemical Physics Letters*, 436, 378-382.
- Tan, E. P. S. & Lim, C. T. (2006). Mechanical characterization of nanofibers – a review. *Composites Science and Technology*, 66, 1102-1111.
- Thostenson, E. T., & Chou, T. -W. (2002). Aligned multi-walled carbon nanotube-reinforced composites: processing and mechanical characterization. *Journal of Physics: Part D*, 35, L77-L80.
- Thostenson, E. T., Ziaee, S., & Chou, T. -W. (2009). Processing and electrical properties of carbon nanotube/vinyl ester nanocomposites. *Composites Science and Technology*, 69 (6), 801-804.
- Tibbetts, G. G. (1985). Lengths of carbon fibers grown from iron catalyst particles in natural gas. *Journal of Crystal Growth*, 73, p. 431.
- Tibbetts, G. G. & Beetz Jr., C. P. (1987). Mechanical properties of vapor-grown carbon fibers. *Journal of Physics: Part D*, 20 (30), 292-297.
- Tibbetts, G. G. & Rodda, E. J. (1988). High temperature limit for the growth of carbon filaments on catalytic iron particles. *Materials Research Society Symposium Proceedings III*, 49.
- Tibbetts, G. G. (1989). Vapor-grown carbon fibers: status and prospects. *Carbon*, 27 (5), 745-747.

- Tibbetts, G. G., Bernardo, C. A., Gorkiewicz, D. W., & Alig, R. L. (1994). Role of sulfur in the production of carbon fibers in the vapor phase. *Carbon*, 32, 569-576.
- Tibbetts, G. G. & McHugh, J. J. (1999). Mechanical properties of vapor-grown carbon fiber composites with thermoplastic matrices. *Journal of Materials Research*, 14, 2871-2880.
- Tibbetts, G. G., Finegan, I. C., & Kwag, C. (2002). Mechanical and electrical properties of vapor-grown carbon fiber thermoplastic composites. *Molecular Crystals and Liquid Crystals*, 387, 129-133.
- Tibbetts, G. G., Lake, M. L., Strong, K. L., & Rice, B. P. (2007). A review of the fabrication and properties of vapor-grown carbon nanofiber/polymer composites. *Composites Science and Technology*, 67 (7-8), 1709-1718.
- Uchida, T., Anderson, D. P., Minus, M. L., & Kumar, S. (2006). Morphology and modulus of vapor grown carbon nano fibers. *Journal of Materials Science*, 41, 5851-5856.
- Vacatello, M. (2001). Monte Carlo simulation of polymer melts filled with solid nanoparticles. *Macromolecules*, 34, 1946-1952.
- Vacatello M. (2003). Predicting the molecular arrangements in polymer-based nanocomposites. *Macromolecular Theory and Simulations*, 12, 86-91.
- Vaia, R. A. & Giannelis, E. P. (2001, May). Polymer nanocomposites: status and opportunities. *Materials Research Society Bulletin*, 394-401.
- VanderHart, D. L., Asano, A., & Gilman, J. W. (2001). NMR measurements related to clay-dispersion quality and organic-modifier stability in nylon-6/clay nanocomposites. *Macromolecules*, 34 (12), 3819-3822.
- Varma, I. K., Rao, B. S., Choudhary, M. S., Choudhary, V., & Varma, D. S. (1985). Effect of styrene on properties of vinyl ester resins, I. *Macromolecular Materials and Engineering*, 30 (1), 191-199.
- Vermogen, A., Masenelli-Varlot, K., & Séguéla R. (2005). Evaluation of the structure and dispersion in polymer-layered silicate nanocomposites. *Macromolecules*, 38 (23), 9661-9669.
- Vidhate, S., Shaito, A., Chung, J., & D'Souza, N. A. (2009). Crystallization, mechanical, and rheological behavior of polyvinylidene fluoride/carbon nanofiber composites. *Journal of Applied Polymer Science*, 112 (1), 254-260.

- Wagner, H. D., Lourie, O., Feldman, Y., & Tenne, R. (1998). Stress-induced fragmentation of multiwall carbon nanotubes in a polymer matrix. *Applied Physics Letters*, 72 (2), 188-190.
- Wagner, H. D. & Vaia, R. A. (2004, November). Nanocomposites: issues at the interface. *Materials Today*, pp. 38-42.
- Wang, C. -S. & Alexander, M. D. (2004). Method of forming conductive polymeric nanocomposite materials. U.S. Patent no. 6,680,016.
- Wei, C. & Srivastava, D. (2004). Nanomechanics of carbon nanofibers: structural and elastic properties. *Applied Physics Letters*, 85 (12), 2208-2210.
- Wu, S. -H., Natsuki, T., Kurashiki, K., Ni, Q. -Q., Iwamoto, M., & Fujii, Y. (2007). Conductivity stability of carbon nanofiber/unsaturated polyester nanocomposites. *Advanced Composite Materials*, 16 (3), 195-206.
- Xia, H. & Song, M. (2005). Preparation and characterization of polyurethane-carbon nanotube composites. *Soft Matter*, 1, 386-394.
- Xu, X., Toghiani, H., & Pittman, Jr., C.U. (2000). Modeling domain mixing in semi-interpenetrating polymer networks composed of poly(vinyl chloride) and 5% to 15% of crosslinked thermosets. *Polymer Engineering and Science*, 40 (9), 2027-2036.
- Xu, L. (2003). Interfacial engineering of the interphase between carbon fibers and vinyl ester resin. East Lansing, MI, USA, Michigan State University, PhD dissertation.
- Xu, J., Donohoe, J. P., & Pittman Jr., C. U. (2004). Preparation, electrical and mechanical properties of vapor grown carbon fiber (VGCF)/vinyl ester composites. *Composites: Part A*, 35 (6), 693-701.
- Xu, Y., Higgins, B., & Brittain, W. J. (2005). Bottom-up synthesis of PS-CNF nanocomposites. *Polymer*, 46 (3), 799-810.
- Yang, S., Taha-Tijerina, J., Serrato-Diaz, V., Hernandez, K., & Lozano, K. (2007a). Dynamic mechanical and thermal analysis of aligned vapor grown carbon nanofiber reinforced polyethylene. *Composites: Part B*, 38 (2), 228-235.
- Yang, S., Benitez, R., Fuentes, A., & Lozano, K. (2007b). Dielectric analysis of VGCNF reinforced polyethylene composites. *Composites Science and Technology*, 67 (6), 1159-1166.

- Yang, Y., Gupta, M. C., & Dudley, K. L. (2007). Towards cost-efficient EMI shielding materials using carbon nanostructure-based nanocomposites. *Nanotechnology*, 18 (34), 345701.
- Yasmin, A., Abot, J. L., & Daniel, I. M. (2003). Processing of clay/epoxy nanocomposites by shear mixing. *Scripta Materialia*, 49 (1), 81-86.
- Yasmin, A., Luo, J. J., Abot, J. L., & Daniel, I. M. (2006). Mechanical and thermal behavior of clay/epoxy nanocomposites. *Composites Science and Technology*, 66 (14), 2415-2422.
- Yong, V. & Hahn, H. T. (2005). Dispersant optimization using design of experiments for SiC/vinyl ester nanocomposites. *Nanotechnology*, 16, 354-360.
- Yoon, P. J., Fornes, T. D., & Paul, D. R. (2002). Thermal expansion behavior of nylon 6 nanocomposites. *Polymer*, 43 (25), 6727-6741.
- Yoonessi, M., Toghiani, H., Daulton, T. L., Lin, J. -S., & Pittman, Jr., C. U. (2005). Clay delamination in clay/poly(dicyclopentadiene) nanocomposites quantified by small angle neutron scattering and high-resolution transmission electron microscopy. *Macromolecules*, 38 (3), 818-831.
- Yousefi, A., Lafleur, P. G., & Gauvin, R. (1997). Kinetic studies of thermoset cure reactions: a review. *Polymer Composites*, 18 (2), 157-168.
- Zeng, J., Saltysiak, B., Johnson, W. S., Schiraldi, D. A., & Kumar S. (2004). Processing and properties of poly(methyl methacrylate)/carbon nano fiber composites. *Composites: Part B*, 35, 173-178.
- Zeng, Q. H., Yu, A. B., & Lu, G. Q. (2008). Multiscale modeling and simulation of polymer nanocomposites. *Progress in Polymer Science*, 33, 191-269.
- Zhang, W., Joshi, A., Wang, Z., Kane, R. S., & Koratkar, N. (2007). Creep mitigation in composites using carbon nanotube additives. *Nanotechnology*, 18, 185703-185708.
- Zhang, W., Srivastava, I., Zhu, Y. -F., Picu, C. R., & Koratkar, N. A. (2009). Heterogeneity in epoxy nanocomposites initiates crazing: significant improvements in fatigue resistance and toughening. *Small*, 5 (12), 1403-1407.
- Zhao, Z. & Gou, J. (2009). Improved fire retardancy of thermoset composites modified with carbon nanofibers. *Science and Technology of Advanced Materials*, 10 (1), 015005(1-6).

- Zhou, Y., Pervin, F., & Jeelani, S. (2007). Effect of vapor grown carbon nanofiber on thermal and mechanical properties of epoxy. *Journal of Materials Science*, *42*, 7544-7553.
- Zhu, J. & Kissell, K. (2008). Nanocomposites technology. Short course presented by NanoRidge Co. at 2008 SAMPE Fall Technical Conference, Memphis, TN, September 8.
- Zhu, Y. A., Sui, Z. J., Zhao, T. J., Dai, Y. C., Cheng, Z. M., & Yuan W. K. (2005). Modeling of fishbone-type carbon nanofibers: a theoretical study. *Carbon*, *43*, 1694-1699.

APPENDIX A
MATERIAL DATA SHEETS

DERAKANE 441-400 Epoxy Vinyl Ester Resin

November 2004

High Performance Resin with Low Styrene Content

DERAKANE 441-400 epoxy vinyl ester resin is a lower styrene-content resin that has an optimized epoxy backbone and resultant superior thermal properties and corrosion resistance performance which places it as a type between DERAKANE 411-350 and DERAKANE 470-300 resins. DERAKANE 441-400 resin offers a superior shelf life compared to conventional vinyl ester resins which provide additional flexibility to fabricators in storage and handling.

Typical Liquid Resin Properties

Property ⁽¹⁾	Value
Density, 25°C/77°F	1.07 g/mL
Dynamic Viscosity, 25°C/77°F	430 mPas
Kinematic Viscosity	400 cSt
Styrene Content	33%
Shelf Life ⁽²⁾ , Dark, 25°C/77°F	9 months

(1) Typical property values only, not to be construed as specifications.

(2) Unopened drum with no additives, promoters, accelerators, etc. added. Shelf life specified from date of manufacture.

Applications and Fabrication Techniques

- FRP storage tanks, vessels, ducts, and on-site maintenance projects, particularly in chemical processing, pulp and paper operations, including chlorine dioxide bleaching towers.
- The resin is designed for ease of fabrication using hand lay-up, spray-up, filament winding, compression molding and resin transfer molding techniques, pultrusion and molded grating applications.

Benefits

- Heat deflection temperature 10-15°C (20-30°F) higher than for DERAKANE 411-350 resin.
- Provides excellent corrosion-resistant protection to organic solvents such as methanol, chlorobenzene, and methyl ethyl ketone to provide long-lasting, reliable equipment for corrosive materials.
- Strength properties are comparable to those for DERAKANE 411 and 470 epoxy vinyl ester resins, allowing flexibility in design and fabrication while still meeting safety requirements.
- Percent elongation two times that of DERAKANE 470-300 resin and equivalent to DERAKANE 411-350 resin. The higher elongation provides FRP equipment with increased toughness and a safety factor for impact damage during process upsets or during shipping and installation.
- Contains only 33 weight percent styrene which allows fabricators to meet California's South Coast Air Quality Management District Rule 1162. Styrene emissions at ambient temperatures can be reduced up to 50% compared with DERAKANE 411-350 resin.
- When properly formulated and cured, complies with FDA regulation 21 CFR 177.2420, covering materials intended for repeated use in contact with food.



Ashland is committed to the continuous evolution of technology and service solutions that promote health, safety and environmental protection around the world.

[®] Registered trademark and [™] trademark of Ashland Inc.

* Registered service mark of the American Chemistry Council

© 2002, 2004 Ashland Inc. All Rights Reserved. CWT-D 5-344 Rev. 1

All statements, information and data presented herein are believed to be accurate and reliable but are not to be taken as a guarantee, express warranty or implied warranty of merchantability or fitness for a particular purpose, or representation, express or implied, for which seller assumes legal responsibility, and they are offered solely for your consideration, investigation and verification. Statements or suggestions concerning possible use of this product are made without representation or warranty that any such use is free of patent infringement and are not recommendations to infringe on any patent.

ASHLAND

Gel Time Formulations

The following table provides typical gel times for MEKP. "Starting point" formulations for MEKP, non-foaming MEKP alternatives, and BPO peroxides are available in separate product bulletins. These and other information are available at www.derakane.com.

MEKP Gel Time Table

Typical Gel Times⁽³⁾ Using NOROX⁽⁴⁾ MEKP-925H⁽⁵⁾ and Cobalt Napthenate-6%⁽⁶⁾

Temperature	15 +/-5 Minutes	30 +/-10 Minutes	50 +/-10 Minutes
18°C/65°F	2.5 phr ⁽⁷⁾ MEKP 0.30 phr CoNap6%	2.5 phr MEKP 0.20 phr CoNap6%	2.0 phr MEKP 0.20 phr CoNap6%
24°C/75°F	1.75 phr MEKP 0.20 phr CoNap6%	1.25 phr MEKP 0.20 phr CoNap6%	1.0 phr MEKP 0.20 phr CoNap6%
30°C/85°F	1.25 phr MEKP 0.3 phr CoNap6%	1.25 phr MEKP 0.20 phr CoNap6%	1.25 phr MEKP 0.20 phr CoNap6%
35°C/95°F	1.5 phr MEKP 0.20 phr CoNap6%	1.0 phr MEKP 0.20 phr CoNap6%	1.5 phr MEKP 0.20 phr CoNap6%


- (3) Thoroughly test any other materials in your application before full-scale use. Gel times may vary due to the reactive nature of these products. Always test a small quantity before formulating large quantities.
- (4) Registered trademark of Norac Inc.
- (5) Materials: NOROX MEKP-925H Methyleneethylketone peroxide (MEKP) or equivalent low hydrogen peroxide content MEKP, Cobalt Napthenate-6% (CoNap6%), Dimethylaniline (DMA), and 2,4-Pentanedione (2,4-P). Use of other MEKP or other additives may result in different gel time results.
- (6) Use of cobalt octoate, especially in combination with 2,4-P can result in 20-30% slower gel times.
- (7) Phr=parts per hundred resin molding compound

Casting Properties

Typical Properties⁽¹⁾ of Postcured⁽⁸⁾ Resin Clear Casting

Property	SI	US Standard	Test Method
Tensile Strength	90 MPa	13,000 psi	ASTM D-638/ISO 527
Tensile Modulus	3.3 GPa	4.8 x 10 ⁵ psi	ASTM D-638/ISO 527
Tensile Elongation, Yield	5-6%	5-6%	ASTM D-638/ISO 527
Flexural Strength	145 MPa	21,000 psi	ASTM D-790/ISO 178
Flexural Modulus	3.4 GPa	5.0 x 10 ⁵ psi	ASTM D-790/ISO 178
Density	1.15 g/cm ³		ASTM D-792/ISO1183
Volume Shrinkage	7.5%	7.5%	
Heat Distortion Temperature ⁽⁹⁾	120°C	245°F	ASTM D-648 Method A/ISO 75
Glass Transition Temperature, Tg2	135°C	275°F	ASTM D-3419/ISO 11359-2
Barcol Hardness	35	35	ASTM D-2583/EN59

- (1) Typical property values only, not to be construed as specifications. SI values reported to two significant figures; US standard values based on conversion.
- (8) Cure schedule: 24 hours at room temperature; 2 hours at 120°C (250°F)
- (9) Maximum stress: 1.8 MPa (264 psi)

 Ashland is committed to the continuous evolution of technology and service solutions that promote health, safety and environmental protection around the world.

® Registered trademark and ™ trademark of Ashland Inc.
* Registered service mark of the American Chemistry Council
© 2002, 2004 Ashland Inc. All Rights Reserved. > CWT-DS-344 Rev. 1

All statements, information and data presented herein are believed to be accurate and reliable but are not to be taken as a guarantee, express warranty or implied warranty of merchantability or fitness for a particular purpose, or representation, express or implied, for which seller assumes legal responsibility, and they are offered solely for your consideration, investigation and verification. Statements or suggestions concerning possible use of this product are made without representation or warranty that any such use is free of patent infringement and are not recommendations to infringe on any patent.

ASHLAND

Gel Time Formulations

The following table provides typical gel times for MEKP. "Starting point" formulations for MEKP, non-foaming MEKP alternatives, and BPO peroxides are available in separate product bulletins. These and other information are available at www.derakane.com.

MEKP Gel Time Table

Typical Gel Times⁽³⁾ Using NOROX⁽⁴⁾ MEKP-925H⁽⁵⁾ and Cobalt Napthenate-6%⁽⁶⁾

Temperature	15 +/-5 Minutes	30 +/-10 Minutes	50 +/-10 Minutes
18°C/65°F	2.5 phr ⁽⁷⁾ MEKP 0.30 phr CoNap6%	2.5 phr MEKP 0.20 phr CoNap6%	2.0 phr MEKP 0.05 phr DMA
24°C/75°F	1.75 phr MEKP 0.20 phr CoNap6%	1.25 phr MEKP 0.20 phr CoNap6%	1.0 phr MEKP 0.05 phr DMA
30°C/85°F	1.25 phr MEKP 0.3 phr CoNap6%	1.25 phr MEKP 0.20 phr CoNap6%	1.25 phr MEKP 0.05 phr DMA 0.08 phr 2,4-P
35°C/95°F	1.5 phr MEKP 0.20 phr CoNap6%	1.0 phr MEKP 0.20 phr CoNap6%	1.5 phr MEKP 0.20 phr CoNap6%


- (3) Thoroughly test any other materials in your application before full-scale use. Gel times may vary due to the reactive nature of these products. Always test a small quantity before formulating large quantities.
- (4) Registered trademark of Norac Inc.
- (5) Materials: NOROX MEKP-925H Methyleneethylketone peroxide (MEKP) or equivalent low hydrogen peroxide content MEKP, Cobalt Napthenate-6% (CoNap6%), Dimethylaniline (DMA), and 2,4-Pentanedione (2,4-P). Use of other MEKP or other additives may result in different gel time results.
- (6) Use of cobalt octoate, especially in combination with 2,4-P can result in 20-30% slower gel times.
- (7) Phr=parts per hundred resin molding compound

Casting Properties

Typical Properties⁽¹⁾ of Postcured⁽⁸⁾ Resin Clear Casting

Property	SI	US Standard	Test Method
Tensile Strength	90 MPa	13,000 psi	ASTM D-638/ISO 527
Tensile Modulus	3.3 GPa	4.8 x 10 ⁵ psi	ASTM D-638/ISO 527
Tensile Elongation, Yield	5-6%	5-6%	ASTM D-638/ISO 527
Flexural Strength	145 MPa	21,000 psi	ASTM D-790/ISO 178
Flexural Modulus	3.4 GPa	5.0 x 10 ⁵ psi	ASTM D-790/ISO 178
Density	1.45 g/cm ³		ASTM D-792/ISO 1183
Volume Shrinkage	7.5%	7.5%	
Heat Distortion Temperature ⁽⁹⁾	120°C	245°F	ASTM D-648 Method A/ISO 75
Glass Transition Temperature, Tg2	135°C	275°F	ASTM D-3419/ISO 11359-2
Barcol Hardness	35	35	ASTM D-2583/EN59

- (1) Typical property values only, not to be construed as specifications. SI values reported to two significant figures; US standard values based on conversion.
- (8) Cure schedule: 24 hours at room temperature; 2 hours at 120°C (250°F)
- (9) Maximum stress: 1.8 MPa (264 psi)

 Ashland is committed to the continuous evolution of technology and service solutions that promote health, safety and environmental protection around the world.

® Registered trademark and™ trademark of Ashland Inc.
* Registered service mark of the American Chemistry Council
© 2002, 2004 Ashland Inc. All Rights Reserved. CWT-DS-344 Rev. 1

All statements, information and data presented herein are believed to be accurate and reliable but are not to be taken as a guarantee, express warranty or implied warranty of merchantability or fitness for a particular purpose, or representation, express or implied, for which seller assumes legal responsibility, and they are offered solely for your consideration, investigation and verification. Statements or suggestions concerning possible use of this product are made without representation or warranty that any such use is free of patent infringement and are not recommendations to infringe on any patent.

ASHLAND

BYK-9076 BYK-9077**Wetting and Dispersing Additives for Solvent-Free Systems and Pigment Concentrates****Composition**

BYK-9076	Alkylammonium salt of a high molecular weight copolymer
BYK-9077	High molecular weight copolymer with pigment affinic groups

Typical Properties

	Amine value in mg KOH/g	Acid value in mg KOH/g	Density at 20°C in g/ml	Non-volatile matter in %	Flash point in °C
BYK-9076	44	38	1,05	96,0	> 100
BYK-9077	48	–	1,05	98,0	> 100

Values indicated in this data sheet describe typical properties and do not constitute specification limits.

Recommended Levels

	% additive (as supplied) based upon			
	carbon blacks	inorganic pigments	organic pigments	titanium dioxide
BYK-9076 BYK-9077	15 - 50	5 - 10	10 - 25	1 - 3

The above recommended use levels are strongly dependent on pigment particle size. Optimal levels may be determined with a **ladder series** in the laboratory.

Incorporation and Processing Instructions

For optimum performance, these additive must be incorporated into the millbase prior to the addition of pigments.



BYK-Chemie is a member of ALTANA Chemie



Applications

	Pigmentconcentrates				Areas of Usage of Pigment Concentrates			
	in polyols	in plasticizers	in unsaturated polyesters	in epoxy resins	PVC-Plastisols	PU foam	PU-floors	Gel Coats
BYK-9076	■	■	■	□	■	■	■	-
BYK-9077	■	■	■	□	□	■	■	□
	■ recommended				□ suitable			

Special Features and Benefits

BYK-9076	significantly reduces viscosity and leads to more Newtonian flow behavior in the mill-base. BYK-9076 is especially suited for stabilizing acidic and neutral carbon black pigments. The product does not contain plasticizers. At the time of publication the active compounds in BYK-9076 fully meet all requirements of Food Contact Regulation 21 CFR (FDA) § 175.105 „Adhesives“ and § 175.300 „Resinous and polymeric coatings“. For the current legal status please contact our product safety department.
BYK-9077	reduces viscosity and leads to more Newtonian flow behavior in the mill-base. BYK-9077 is especially suited for stabilizing basic carbon black pigments. The product does not contain plasticizers.

Function

These high molecular weight additives **deflocculate** pigments through steric stabilization of the pigments. They provide equal electrical charge to pigments and thus avoid additionally possible co-flocculation of pigments that are not equally charged. Due to the small particle sizes of the deflocculated pigments, high gloss is achieved and color strength improved. Additionally, transparency of transparent pigments and hiding power of opaque pigments are increased. These products reduce viscosity, subsequently, leveling is improved and higher pigment loading is possible.

Available Packaging

Drums and pails

Containers not completely emptied must be closed immediately after use!

ANTI-TERRA®, BYK®, BYK®-DYNWET®, BYK®-SILCLEAN®, BYKANOL®, BYKETOL®, BYKOPLAST®, BYKUMEN®, DISPERBYK®, DISPERPLAST®, LACTIMON®, SILBYK® and VISCOBYK® are registered trademarks of BYK-Chemie.

This information is given to the best of our knowledge. Because of the multitude of formulations, production and application conditions, all the above mentioned statements have to be adjusted to the circumstances of the processor. No liabilities, including those for patent rights, can be derived from this fact for individual cases.

12/05 - This data sheet replaces all previous issues - Printed in Germany



BYK-Chemie GmbH, Postfach 100245, 46462 Wesel, Germany
Tel. +49 (0) 281 670-0, Fax +49 (0) 281 65735, info@byk.com, www.byk-chemie.com

BYK-A 500 BYK-A 501
BYK-A 515 BYK-A 550
BYK-A 555 BYK-A 560

Silicone-Free Air Release Additives for Unsaturated Polyester, Epoxy and PUR Resins

Composition

BYK-A 500 BYK-A 501 BYK-A 515 BYK-A 550 BYK-A 555	Solution of foam destroying polymers, silicone free
BYK-A 560	Solution of foam destroying polyacrylates and polymers, silicone free

Typical Properties

	Density at 20°C in g/ml	Non-volatile matter in %	Flash point in °C	Hazen color index	Turbidity TE/F	Refractive index at 20°C
BYK-A 500	0,88	6,5	45	< 200	< 10	1,495
BYK-A 501	0,89	44,0	46	< 200	< 10	1,500
BYK-A 515	0,82	20,0	34	< 250	< 5	1,438
BYK-A 550	0,87	9,7	47	< 250	< 5	1,501
BYK-A 555	0,88	38,0	43	< 250	< 10	1,507
BYK-A 560	0,87	12,0	43	> 250	> 10	1,491

Values indicated in this data sheet describe typical properties and do not constitute specification limits.



BYK-Chemie is a member of ALTANA Chemie



Recommended Levels

	% additive (as supplied) based upon
	total formulation
BYK-A 500 BYK-A 501 BYK-A 515 BYK-A 550 BYK-A 555	0,1 - 0,5
BYK-A 560	0,2 - 0,5

Incorporation and Processing Instructions

To prevent air entrapment caused during the manufacturing and/or application process, it is recommended to stir the air release additive into the resin prior to the addition of other formulation components.

In some resin systems air release additives may cause haze in finished parts.

Applications

	UP-Resins	Fiber wetting	Gel Coats	Casting	Transpa- rent parts	Epoxy resins	PUR- Systems	Acrylic solid surface
BYK-A 500	■	-	□	□	■	■	□	-
BYK-A 501	□	-	□	□	-	■	■	-
BYK-A 515	■	□	□	□	-	-	-	■
BYK-A 550	□	-	□	■	■	■	□	-
BYK-A 555	■	-	■	■	-	□	□	-
BYK-A 560	■	■	■	■	-	□	-	-

■ recommended □ suitable

Special Features and Benefits

BYK-A 500	shows a good compatibility in UP-resins and is specifically recommended for transparent final parts. Also is used in Epoxy flooring formulations and PUR systems.
BYK-A 501	is a highly effective air release additive similar to BYK-A 555.
BYK-A 515	is a highly surface active air release additive with fiber wetting properties. In hand lay up and spray up applications BYK-A 515 is often used in combination with BYK-A 555 or BYK-A 501. In highly thixotropic gel-coats BYK-A 515 is sometimes the only effective air release additive. BYK-A 515 is often used in acrylic syrup to prevent air entrapment.
BYK-A 550	shows a strong air release effect without creating a strong haziness effect in unsaturated polyester resins.
BYK-A 555	shows the highest efficiency and is the best air release additive for practically all UP-resins and applications.
BYK-A 560	combines a very good air release effect with very good fiber wetting properties. BYK-A 560 is recommended for all fiber glass reinforced unsaturated polyester applications. In some gel coat formulations BYK-A 560 shows excellent air release effects specifically in airless applications. BYK-A 560 often is used to improve fiber wetting in RTM and Resin Infusion processes.

Available Packaging

Drums and pails

Containers not completely emptied must be closed immediately after use!

ANTI-TERRA®, BYK®, BYK®-DYNWET®, BYK®-SILCLEAN®, BYKANOL®, BYKETOL®, BYKOPLAST®, BYKUMEN®, DISPERBYK®, DISPERPLAST®, LACTIMON®, NANOBYK®, SILBYK® and VISCOBYK® are registered trademarks of BYK-Chemie.

This information is given to the best of our knowledge. Because of the multitude of formulations, production and application conditions, all the above mentioned statements have to be adjusted to the circumstances of the processor. No liabilities, including those for patent rights, can be derived from this fact for individual cases.

08/06 - This data sheet replaces all previous issues - Printed in Germany



BYK-Chemie GmbH, Postfach 100245, 46462 Wesel, Germany
Tel. +49 (0) 281 670-0, Fax +49 (0) 281 65735, info@byk.com, www.byk-chemie.com

PR-24-XT-LHT Data Sheet

Product Nomenclature

The LHT grade is produced by heat-treating the fiber at 1500°C. This converts any chemically vapor deposited carbon present on the surface of the fiber to a short range ordered structure. The inherent conductivity of the fiber is increased.

Carbon nanofiber properties

Fiber diameter, nm (average):	100
CVD carbon overcoat present on fiber:	no
Surface area, m ² /gm:	43
Dispersive surface energy, mJ/m ² :	155
Moisture, wt%:	<5
Iron, ppm:	<14,000
Polyaromatic hydrocarbons, mg PAH/gm fiber:	<1

APPENDIX B
SAS PROGRAM CODES

SAS Codes for Chapter 3

Code for the storage modulus:

```
OPTIONS PS=52 LS=85;
DATA DMA; /* Defines data set */
INFILE 'E:\DMA.DAT'; /* Reads in the data file */
INPUT TYPE $ AGENT $ MIXING $ AMOUNT STORAGE LOSS;
/* Defines the factors */
A2 = AMOUNT*AMOUNT;
A3 = AMOUNT*A2;
RUN;
ODS GRAPHICS ON;
PROC GLM PLOTS = (DIAGNOSTICS); /* Procedure for linear models and
generation of the ANOVA table */
CLASS TYPE AGENT MIXING AMOUNT;
MODEL STORAGE = TYPE AGENT MIXING AMOUNT TYPE*AGENT TYPE*MIXING
TYPE*AMOUNT AGENT*MIXING
AGENT*AMOUNT MIXING*AMOUNT/SS3;
RUN;
PROC MEANS MEAN; /* Procedure for calculating various means */
CLASS TYPE AGENT MIXING AMOUNT;
VAR STORAGE;
WAYS 1 2 3 4;
RUN;
DATA TYPE_P; /* Creates a subset of the original data */
SET DMA;
IF TYPE = 'P';
RUN;
DATA TYPE_O; /* Creates a subset of the original data */
SET DMA;
IF TYPE = 'O';
RUN;
PROC REG DATA = TYPE_P PLOTS = ALL; /* Procedure for regression and
data fitting */
MODEL STORAGE = AMOUNT A2 A3;
RUN;
PROC REG DATA = TYPE_O PLOTS = ALL; /* Procedure for regression and
data fitting */
MODEL STORAGE = AMOUNT A2 A3;
RUN;
ODS GRAPHICS OFF;
QUIT;
```

Code for the loss modulus:

```
OPTIONS PS=52 LS=85 FORMDLIM='-';
DATA DMA; /* Defines data set */
INFILE 'E:\DMA.DAT'; /* Reads in the data file */
INPUT TYPE $ AGENT $ MIXING $ AMOUNT STORAGE LOSS; /* Defines the
factors */
A2 = AMOUNT*AMOUNT;
A3 = AMOUNT*A2;
RUN;
ODS GRAPHICS ON;
PROC GLM PLOTS = (DIAGNOSTICS); /* Procedure for linear models and
generation of the ANOVA table */
CLASS TYPE AGENT MIXING AMOUNT;
MODEL LOSS = TYPE AGENT MIXING AMOUNT TYPE*AGENT TYPE*MIXING
TYPE*AMOUNT AGENT*MIXING
AGENT*AMOUNT MIXING*AMOUNT/SS3;
LSMEANS AGENT*MIXING/STDERR PDIFF LINES; /* Command for Fisher's least
significant differences (LSD) comparisons */
RUN;
PROC MEANS MEAN; /* Procedure for calculating various means */
CLASS TYPE AGENT MIXING AMOUNT;
VAR STORAGE;
WAYS 1 2 3 4;
RUN;
DATA HS; /* Creates a subset of the original data */
SET DMA;
IF MIXING = 'HS';
RUN;
DATA HU; /* Creates a subset of the original data */
SET DMA;
IF MIXING = 'HU';
RUN;
DATA US_YES; /* Creates a subset of the original data */
SET DMA;
IF MIXING = 'US' & AGENT = 'Y';
RUN;
DATA US_NO; /* Creates a subset of the original data */
SET DMA;
IF MIXING = 'US' & AGENT = 'N';
RUN;
PROC REG DATA=US_YES PLOTS = ALL; /* Procedure for regression and data
fitting */
MODEL LOSS = AMOUNT A2 A3;
RUN;
PROC REG DATA=US_NO PLOTS = ALL; /* Procedure for regression and data
fitting */
MODEL LOSS = AMOUNT A2 A3;
RUN;
PROC REG DATA=HS PLOTS = ALL; /* Procedure for regression and data
fitting */
MODEL LOSS = AMOUNT A2;
RUN;
```



```
PROC REG DATA=HU PLOTS = ALL; /* Procedure for regression and data
fitting */
MODEL LOSS = AMOUNT A2 A3;
RUN;
ODS GRAPHICS OFF;
QUIT;
```

SAS Codes for Chapter 4

Code for the storage modulus:

```
OPTIONS PS=52 LS=85 FORMDLIM='-';
DATA DMA; /* Defines data set */
INFILE 'E:\DMA_TEMP_DATA.DAT'; /* Reads in the data file */
INPUT TYPE $ AGENT $ MIXING $ AMOUNT TEMP STORAGE LOSS; /* Defines the
factors */
RUN;
ODS GRAPHICS ON;
PROC GLM PLOTS = (DIAGNOSTICS); /* Procedure for linear models and
generation of the ANOVA table */
CLASS TYPE AGENT MIXING AMOUNT TEMP;
MODEL STORAGE = TYPE AGENT MIXING AMOUNT TEMP TYPE*AGENT TYPE*MIXING
TYPE*AMOUNT TYPE*TEMP AGENT*MIXING AGENT*AMOUNT
AGENT*TEMP MIXING*AMOUNT MIXING*TEMP AMOUNT*TEMP
TYPE*AGENT*MIXING TYPE*AGENT*AMOUNT TYPE*AGENT*TEMP
TYPE*MIXING*AMOUNT TYPE*MIXING*TEMP TYPE*AMOUNT*TEMP
AGENT*MIXING*AMOUNT AGENT*MIXING*TEMP AGENT*AMOUNT*TEMP
MIXING*AMOUNT*TEMP/SS3;
RUN;
LSMEANS TYPE*AGENT*MIXING/STDERR PDIF LINES; /* Command for Fisher's
least significant differences (LSD) comparisons */
RUN;
DATA MIXING_HS_HU; /* Creates a subset of the original data */
SET DMA;
IF MIXING = 'HS' | MIXING = 'HU';
RUN;
DATA MIXING_US_TYPE_O_AGENT_Y; /* Creates a subset of the original data
*/
SET DMA;
IF MIXING = 'US' & TYPE = 'O' & AGENT = 'Y';
RUN;
DATA MIXING_US_OTHER; /* Creates a subset of the original data */
SET DMA;
IF MIXING = 'US' & NOT(TYPE = 'O' & AGENT = 'Y');
RUN;
PROC GLM DATA = MIXING_HS_HU PLOTS = ALL; /* Procedure for regression
*/
MODEL STORAGE = AMOUNT TEMP AMOUNT*TEMP AMOUNT*AMOUNT TEMP*TEMP
AMOUNT*TEMP AMOUNT*TEMP*TEMP AMOUNT*AMOUNT*AMOUNT/SS3;
RUN;
PROC GLM DATA = MIXING_US_TYPE_O_AGENT_Y PLOTS = ALL; /* Procedure for
regression */
```

```

MODEL STORAGE = AMOUNT TEMP AMOUNT*TEMP AMOUNT*AMOUNT TEMP*TEMP
AMOUNT*TEMP AMOUNT*AMOUNT*TEMP AMOUNT*TEMP*TEMP/SS3;
RUN;
PROC GLM DATA = MIXING_US_OTHER PLOTS = ALL; /* Procedure for
regression */
MODEL STORAGE = AMOUNT TEMP AMOUNT*TEMP AMOUNT*AMOUNT TEMP*TEMP
AMOUNT*TEMP AMOUNT*AMOUNT*TEMP AMOUNT*TEMP*TEMP/SS3;
RUN;
ODS GRAPHICS OFF;
QUIT;

```

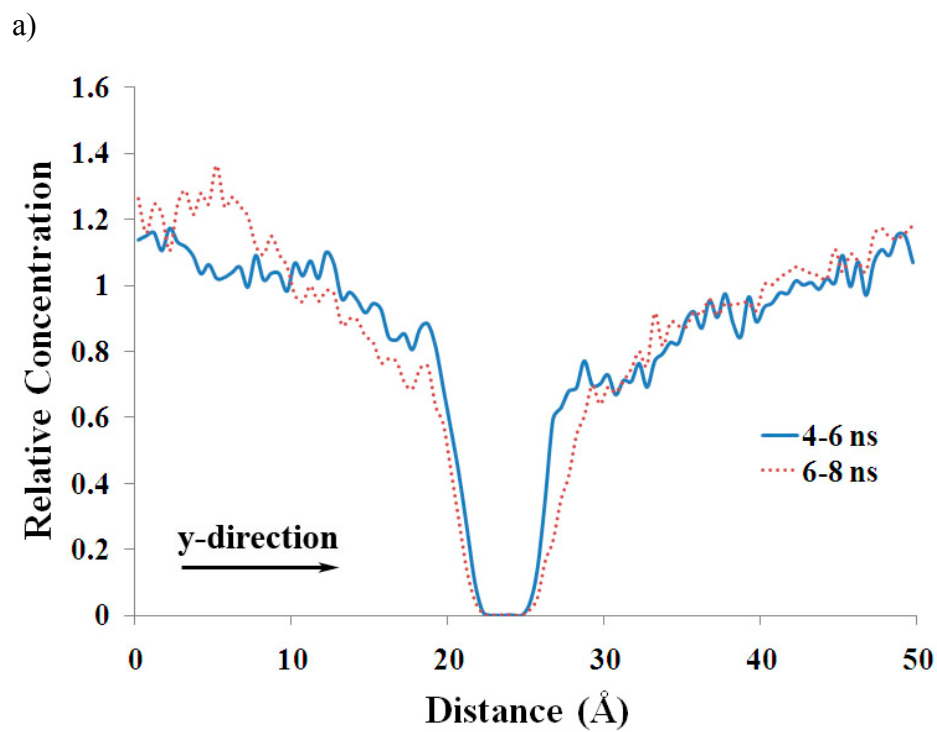
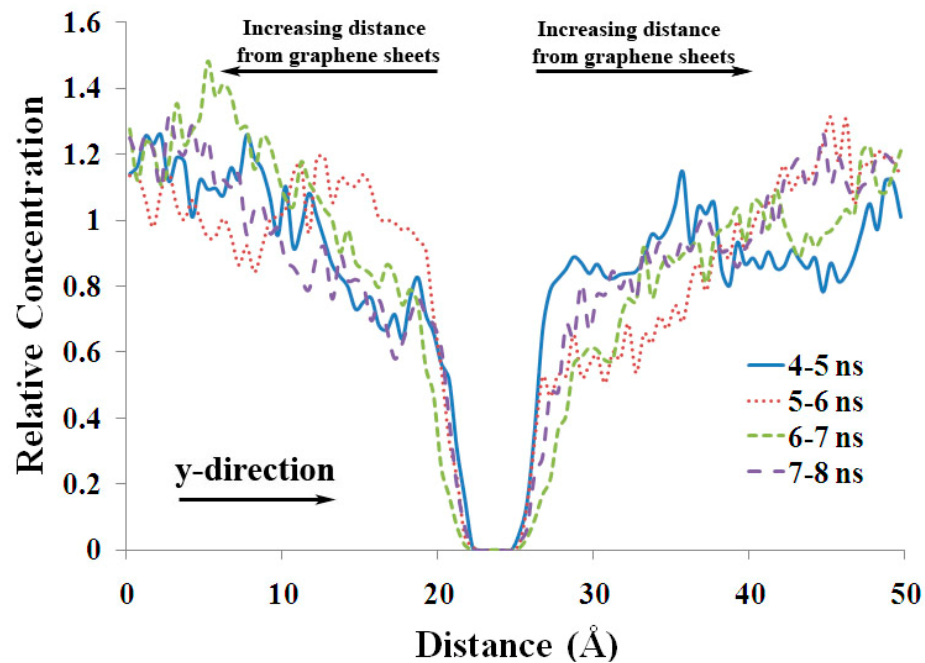
Code for the loss modulus:

```

OPTIONS PS=52 LS=85 FORMDLIM='-';
DATA DMA; /* Defines data set */
INFILE 'E:\DMA_TEMP_DATA.DAT'; /* Reads in the data file */
INPUT TYPE $ AGENT $ MIXING $ AMOUNT TEMP STORAGE LOSS; /* Defines the
factors */
RUN;
ODS GRAPHICS ON;
PROC GLM PLOTS = (DIAGNOSTICS); /* Procedure for linear models and
generation of the ANOVA table */
CLASS TYPE AGENT MIXING AMOUNT TEMP;
MODEL LOSS = TYPE AGENT MIXING AMOUNT TEMP TYPE*AGENT TYPE*MIXING
TYPE*AMOUNT TYPE*TEMP AGENT*MIXING AGENT*AMOUNT
AGENT*TEMP MIXING*AMOUNT MIXING*TEMP AMOUNT*TEMP
TYPE*AGENT*MIXING TYPE*AGENT*AMOUNT TYPE*AGENT*TEMP
TYPE*MIXING*AMOUNT TYPE*MIXING*TEMP TYPE*AMOUNT*TEMP
AGENT*MIXING*AMOUNT AGENT*MIXING*TEMP AGENT*AMOUNT*TEMP
MIXING*AMOUNT*TEMP/SS3;
RUN;
LSMEANS TYPE*AGENT*MIXING/STDERR PDIFF LINES; /* Command for Fisher's
least significant differences (LSD) comparisons */
RUN;
DATA MIXING_HS_HU; /* Creates a subset of the original data */
SET DMA;
IF MIXING = 'HS' | MIXING = 'HU';
RUN;
DATA MIXING_US; /* Creates a subset of the original data */
SET DMA;
IF MIXING = 'US';
RUN;
PROC GLM DATA = MIXING_HS_HU PLOTS = ALL; /* Procedure for regression
*/
MODEL LOSS = AMOUNT TEMP AMOUNT*TEMP AMOUNT*AMOUNT TEMP*TEMP
AMOUNT*AMOUNT*TEMP AMOUNT*TEMP*TEMP TEMP*TEMP*TEMP/SS3;
RUN;
PROC GLM DATA = MIXING_US PLOTS = ALL; /* Procedure for regression */
MODEL LOSS = AMOUNT TEMP AMOUNT*TEMP AMOUNT*AMOUNT TEMP*TEMP
AMOUNT*TEMP*TEMP AMOUNT*AMOUNT*AMOUNT TEMP*TEMP*TEMP/SS3;
RUN;
QUIT;

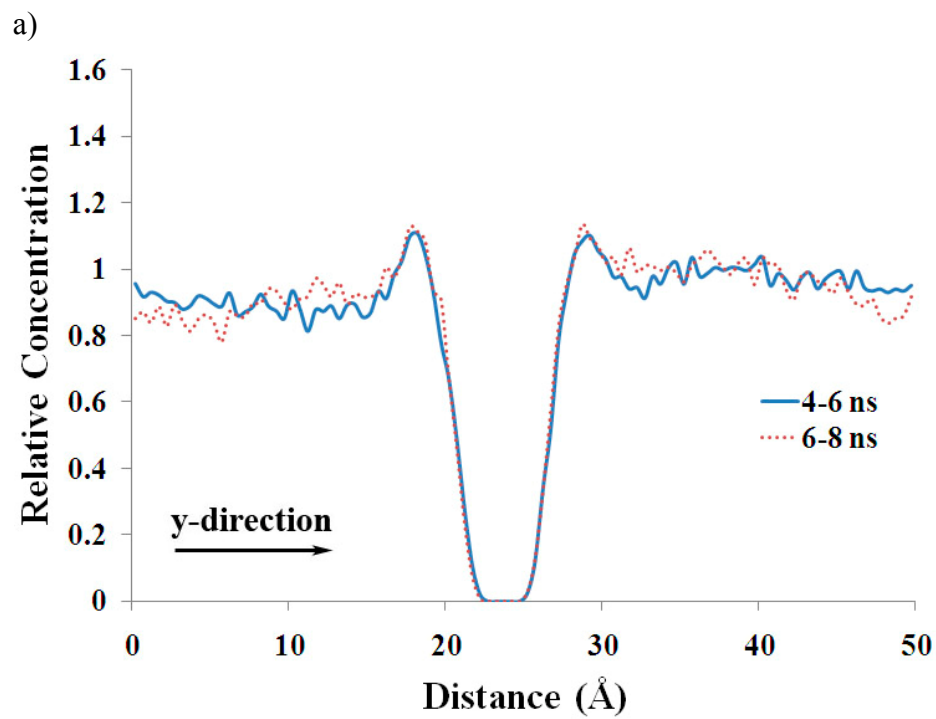
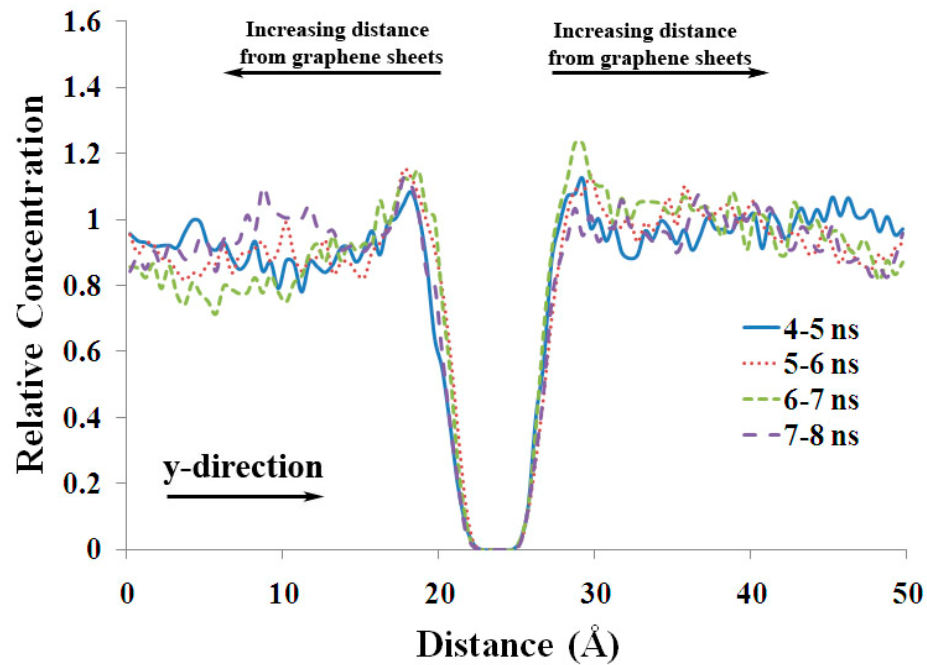
```

APPENDIX C
SUPPLEMENTAL CONCENTRATION PROFILES



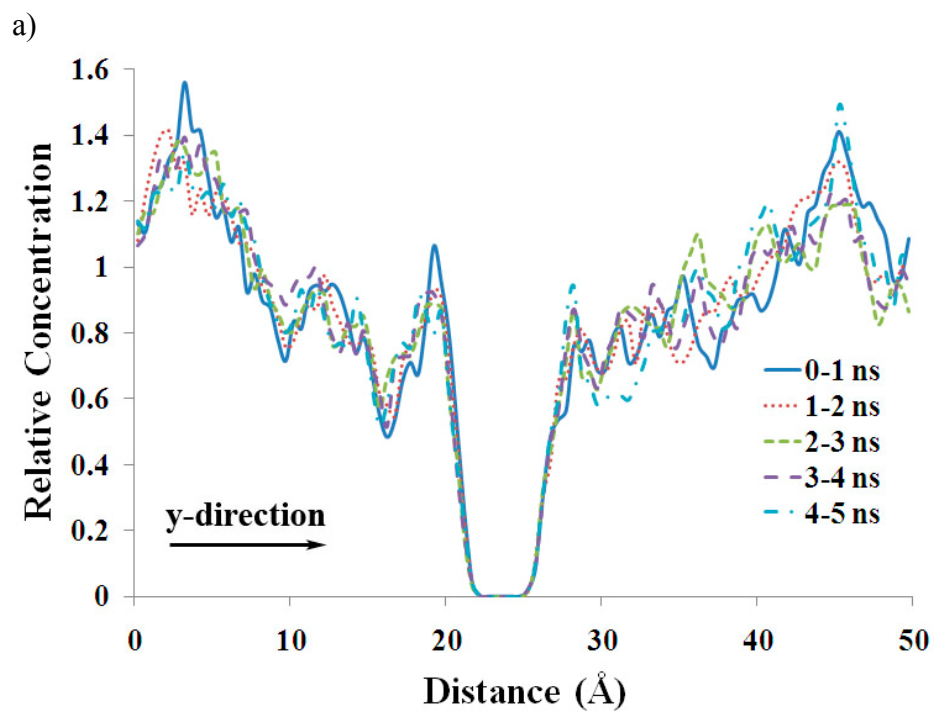
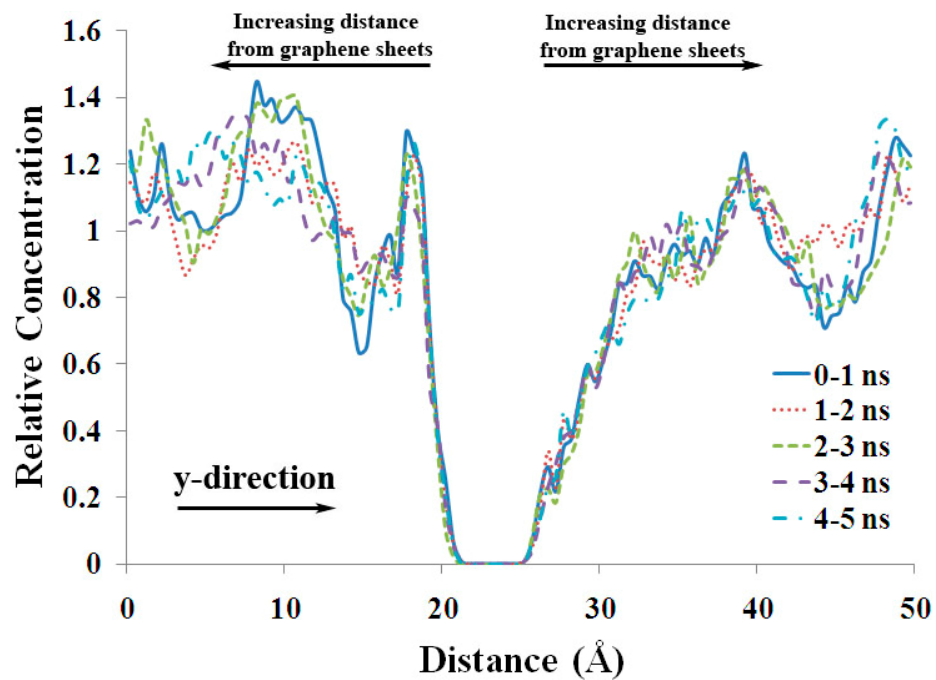
b)

Figure A.1 Concentration profiles of VE1, time-averaged over each successive 1 ns (a) and 2 ns (b) time intervals at 1000 K.



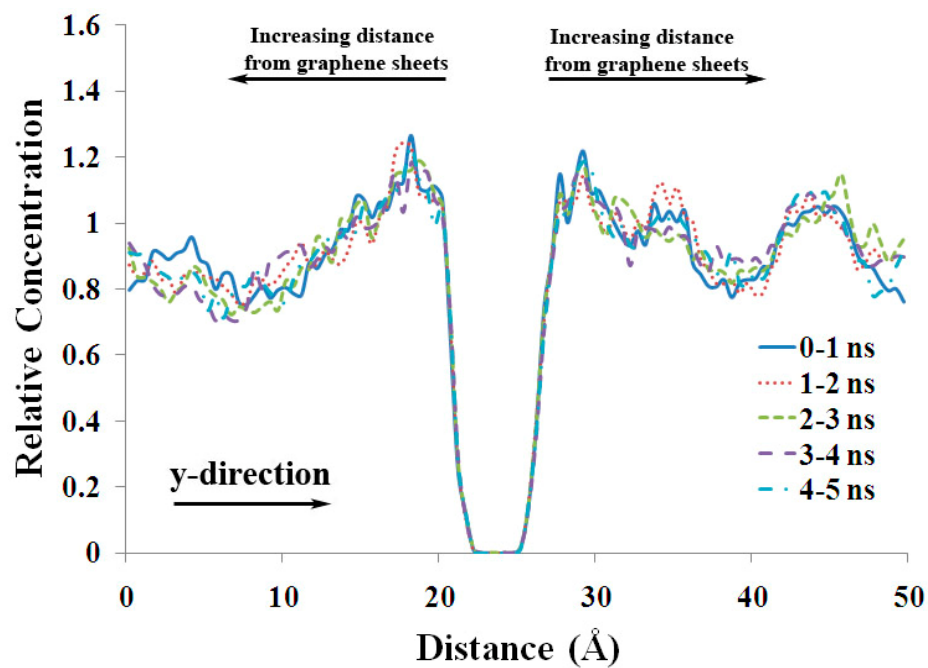
b)

Figure A.2 Concentration profiles of VE2, time-averaged over each successive 1 ns (a) and 2 ns (b) time intervals at 1000 K.

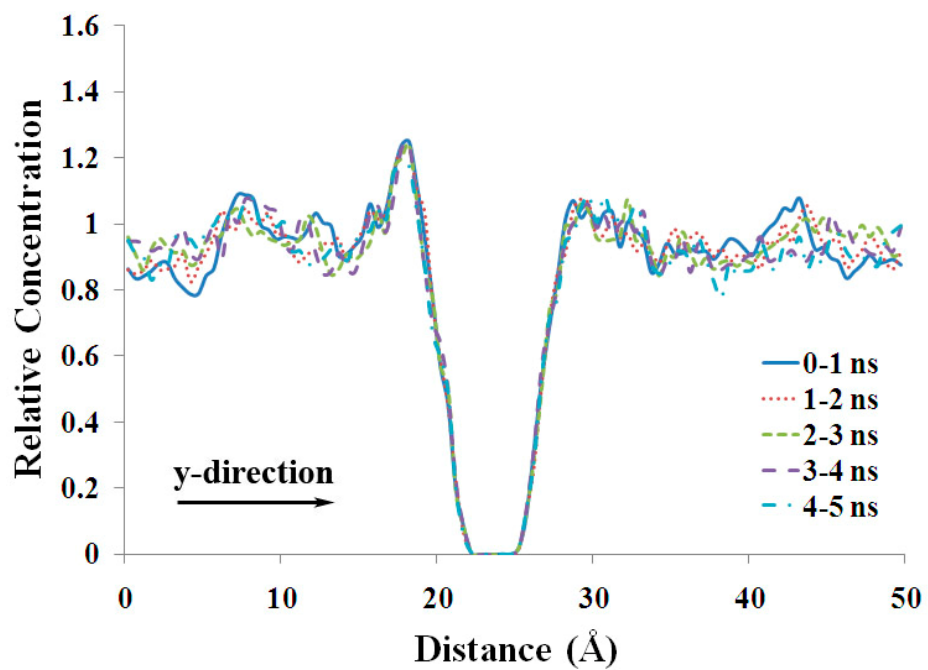


b)

Figure A.3 Concentration profiles of VE1 time-averaged over each successive 1 ns time interval at 300 K (total simulation time of 5 ns) for simulations following cooling procedure C1 (a) and C2 (b).



a)



b)

Figure A.4 Concentration profiles of VE2 time-averaged over each successive 1 ns time interval at 300 K (total simulation time of 5 ns) for simulations following cooling procedure C1 (a) and C2 (b).